UNIVERSITY OF CALIFORNIA
SANTA CRUZ

MODELING AND CONTROL OF ACTIVE TWIST AIRCRAFT

A dissertation submitted in partial satisfaction of the
requirements for the degree of

DOCTOR OF PHILOSOPHY

in

COMPUTER ENGINEERING

by

Nicholas Bryan Cramer

March 2017

The Dissertation of Nicholas Bryan Cramer
is approved:

Professor Mircea Teodorescu, Chair

Professor Gabe Elkaim

Dr. Sean Swei

Dean Tyrus Miller
Vice Provost and Dean of Graduate Studies

Table of Contents

List of Figures

List of Tables

Abstract

Modeling and Control of Active Twist Aircraft

by

Nicholas Bryan Cramer

The Wright Brothers marked the beginning of powered flight in 1903 using an active twist mechanism as their means of controlling roll. As time passed due to advances in other technologies that transformed aviation the active twist mechanism was no longer used. With the recent advances in material science and manufacturability, the possibility of the practical use of active twist technologies has emerged. In this dissertation, the advantages and disadvantages of active twist techniques are investigated through the development of an aeroelastic modeling method intended for informing the designs of such technologies and wind tunnel testing to confirm the capabilities of the active twist technologies and validate the model. Control principles for the enabling structural technologies are also proposed while the potential gains of dynamic, active twist are analyzed.

Dedicated to Val for sticking with me and supporting me while I made a terrible life choice.

Acknowledgments

I would like to thank my committee for taking the time to read and comment on this tome. Specifically, I would like to thank my advisor Mircea Teodorescu for giving me a chance and the intellectual freedom to pursue my interest but most importantly being my friend as well.

There are many others who have helped to guide me to the completion of my Ph.D. Chief amongst those are my collaborators at NASA Ames. I need to thank individually; Sean Swei who has been an incredible mentor to me over the years and Kenneth Cheung for helping to expand my horizons. Special thanks to everyone in the Coded Structures Lab and the NASA Langley Flight Dynamics Branch 12-Foot Low-Speed Tunnel test team.

I had the opportunity to work with some industry partners from Aurora Flight Science Cory Kays and Van Livieratos who gave me great insight into the process of development and provided a platform for my work.

I would be remiss not to mention the members of my lab especially those who I had working with me Tyler Clinkaberry, Maryam Tebyani, and Christopher Seruge.

There are many others who provided support and knowledge: Without my parents, Mike and Rebecca I would not have had this opportunity. My roommates who over the past years have become my family.

Chapter 1

Introduction

1.1 Motivation

Demand for commercial air travel has increased at a steady rate of 9% annual growth rate of passenger and freight traffic globally over the past three decades. [78] With the continued increase in demand for air travel the ramifications of air travel must be addressed. These range from health concerns to ever increasing CO_2 emissions. It is expected that between 1995 and 2050 the contribution of CO_2 from air travel will to increase by a factor of 36 which is why air travel and its efficiency are heavily discussed in climate change policy. [55] While air travel has it's downsides it is also a critical component for trade [69], regional developments [43], and intercultural communications [3]. With air travels key role in financial and social institutions, it is unreasonable to expect that anything less and a holistic solution of technological and policy advancement could appropriately address the salient issues associated with it.

Increased aircraft efficiency is typically achieved either by a reduction of weight or and an increase in aerodynamic efficiency. In the industry, the most common production level approach is to reduce weight through the use of composites. For example Boeing's 787 Dreamliner which was able to achieve a 20% weight reduction by using carbon fiber plastic composites. [19] On the other end of the spectrum the aerospace community has been investigating the use of morphing aircraft to increase the aerodynamic efficiency through the use of shape morphing.[5, 37, 70] Shape morphing can be described as the ability of an aircraft to change some form of its geometry. There is very few limitation of what can be considered "shape morphing" other than the fact that traditional hinged flaps/slats are not sufficient changes in the aircraft geometry to be counted. Figure 1.1 shows the general range of aircraft geometries that can be adjusted for reference.

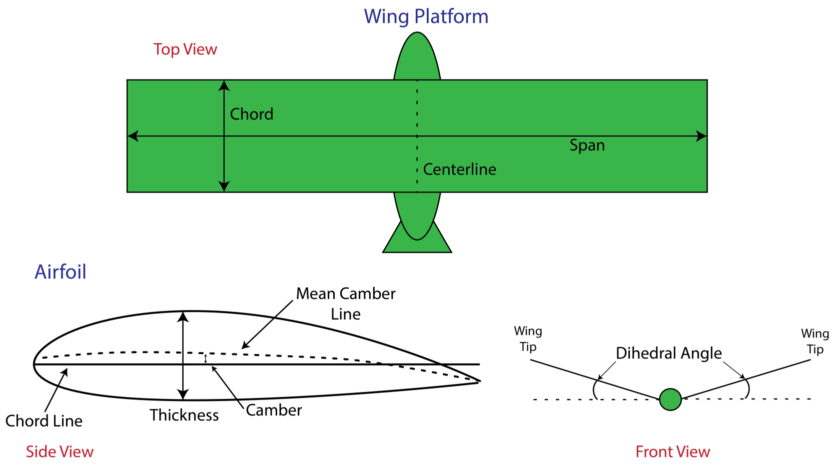

Figure 1.1: General definitions of aircraft geometries, this is a recreation of a figure provided by NASA Glenn Research Center

Shape morphing typically achieves the increase in aerodynamic efficiency by changing the aircraft geometry to become more optimal at various flight conditions. Typical fixed wing aircraft are designed to have maximum efficiency around their nominal cruise conditions, which necessarily results in the design being sub-optimal at other flight conditions. In theory, the aircraft should spend the vast majority of it's flight time at its nominal cruise condition but due to things like weather, airspace congestion, and distance of flight this is not always true, and shape morphing can help address this problem.

There are four significant challenges associated with making shape morphing a viable technology for the industry, distributed high-power density actuation, structural mechanization, flexible skins, and control law development. [61] Of these primary challenges we will be addressing the control law development, but the linkage between all of these difficulties will be evident. This dissertation will specifically be focusing on the development of reasonable models, control and capability analysis of an active twist aircraft. Wing twist is defined as the angle that the wing tip is compared to the angle that the wing meets the aircraft body as shown in Figure 1.2. Wing twist was selected because it is capable of generating many interesting and potentially important phenomena for increased efficiency.

1.2 Applications

The motivation example focused primarily on commercial aircraft but the application space for this research can be broken down into four areas, where commercial

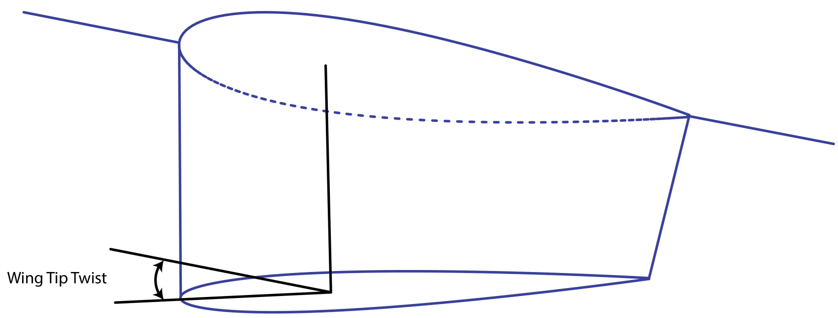

Figure 1.2: Definition of wing twist, where the tip of the wing is twisted at an angle different than the one that the wing meets the plane body at

aircraft are but one part.

- Commercial Aviation - The commercial aviation sector was touched on above, but effective control of active twist could have a direct and immediate impact on this field. A very effective use of wing twist could be the creation of active twisting winglets that can be trimmed to optimal wash out of various flight regimes. This could provide significant performance increases during take-off and landing.

- Military Aircraft - The military has a desire to have an aircraft that is flexible to a multitude of missions. The use of active twist technology would allow for more efficient vehicles and longer flights but more crucially would increase the performance envelope of the aircraft. It could be especially important as an enabling technology for other high-efficiency designs such as blended body and flying wings where the minimum stability margin of the aircraft can be catastrophically affected by the discontinuities that come from traditional flaps.

- Unmanned Aerial Vehicles (UAVs) - UAVs have a lot of promise as means of delivery or inspection. One of the primary problems with UAV's is that the rotor copter set-up that is ideal for these missions has sever longevity issues while the fixed-wing variant needs long ranges to take off and land and are difficult to loiter in the same spot. The active twist technology could help by decreasing the loiter speed and loiter radius of the UAV while also reducing the range necessary to take off and land.

- High Altitude Long Endurance (HALE) Aircraft - Active twist for HALE aircraft have many of the same advantages as commercial aviation, but they also have a distinct advantage of not typically having passengers. This means that it is possible for the HALE to make use of some of the aerodynamic efficiency gains of active that can be seen in flapping flight that would be untenable for passengers.

1.3 Contributions of this Work

This work takes a holistic approach to the design and analysis of the active twist controllers which result in various contributions to the field as listed below.

- Development of an aeroelastic simulation method that is specifically tailored to the targeted operating regime.
- Design of wind tunnel tests to access the broader capabilities of the technology and validate the simulation.
- Proposed decentralized control expanding on the work of Siljak [68] to address the issues associated with overlapping decentralized control.

- Expansion of the concept of the transfer matrix method as a means of control centered modeling and decentralized structural stabilization.
- Explored the use of an aerodynamic database for structural state estimation and inner loop active twist control.

Chapter 2

Background

2.1 Aeroelastic Modeling

Aeroelasticity has been a well-known and well-studied problem since shortly after the creation of planes. To date, many of the studies use some combination of an aerodynamic simulator that then couples the aerodynamics with the mode shapes of the wing. Indeed Nguyen et. al. [52] use an elastic wing model, a vortex lattice program (Vorview), and a geometry modeling tool coupled together to create an aeroelastic model. The flexible wing modeling utilizes twist, spanwise and chordwise bending including bending-torsion coupling. They eventually simplified the problem by neglecting the chordwise bending because it is noted that it is small, especially in comparison to the wing sweep angle.

The aeroelastic angle of attack is defined to be the velocity of the wind in the chordwise direction over the velocity in the vertical direction. These velocities are a combination of the air speed and the elastic velocities. The forces resulting from the aeroelastic angle of attack are calculated by using the aeroelastic angle of attack and the lift and pitching moment coefficients as calculated by Vorview.

The static and dynamic analysis were performed by Galerkin method to separate the mode shapes for each given natural frequency. The static analysis of the primary mode with no dynamics is then added to the dynamics modes, creating a perturbation method approach. Each state equation is the result of the summation of a primary set of modes, and then the states are converted into the modal coordinates are used for the calculations.

In [54] the work from [52] is extended. Nguyen et. al present variable camber continuous trailing edge (VCCTE) system to control the wing twist and wing bending. The proposed wing would be formed into the optimal configuration for drag reduction during cruising and possibly lift enhancement during take off. The VCCTE would utilize three component flaps to dynamically shape the mean chord of the airfoil and to change the aerodynamic center location and the spanwise variation in lift.

The generic transport model (GTM) was used as the basis for the rigid body model. The aeroelastic equations were derived for the wings using primarily the adjusted local angle of attack and the lift, drag, and moment coefficients associated with the instantaneous wing configuration. The beam model used was the same that was used in [52] with the addition of bending-torsion coupling and the inclusion of chordwise bending. The GTM has jet engines attached, and the effects of the thrust from the engines on the wings were also considered, as was the fact that fuel is stored in the wings resulting in the varying wing density, area moment of inertia, and the bending torsion constants.

The rigid body mechanics and the aeroelastic equations associated with the wings were coupled via the integration of the local lift, drag and moments along the span. This was important because the frequencies of the aeroelastic and rigid body components are close and coupled. The equations of motion take the form of a time-varying state space model. An observer is proposed to estimate the local angle of attack, and then an LQR control was suggested to minimize the drag, states, and power.

With many of the same assumptions that Nguyen et. al. work on Wang et. al presented a reduced modal approach to modeling nonlinear aeroelastic responses in flexible wings in [81]. They also showed H_∞ control for the trim from the reduced modal model. The wing was treated like a typical beam system to get the expected modes then the amplitude of the modes was used to generate that dynamics which was then reduced. The dynamic modal equation relates linearly the natural frequencies to the modal amplitudes and the interaction between the modal amplitudes as well as the external forces.

The aerodynamics forces were calculated using a 2-D unsteady airfoil theory to develop lifting, drag, and moment coefficient on angle of attack. The induced angle of attack was generated with an approximation of Theodorsen's lift deficiency function.

Due to the reduction scheme, there can be some drift in the values that must be checked via a spanwise integration. The external force effects due to thrust, gust, and control surface input were converted to the modal coordinates to create the dynamics equation, which was used for the proposed control.

Getting away from the assumed mode shapes that the previous works, Su introduced a strain based modeling technique for a slender, flexible wing in [72]. The localized strain components can be integrated to arrive at the local position and positional rate components for the finite elements. To allow for warping of the system a warping field was proposed where a finite selection of warping modes for the cross-sectional area and the effects of neighboring warped cross sections are considered. Then using the virtual work concept the external and internal virtual work was combined to derive the equations of motion.

2.2 Morphing Wings

Morphing wings as a means of control is an intuitive and readily understandable means of controlling an aircraft. In our daily life, we often see birds flying, and their primary mechanism of motion control is changing the shape of their wings. Not surprisingly then the first attempt at roll control was done via wing warping during the Wright brothers first flight. [16] The use of compliant wing morphing mechanisms quickly fell out of favor it seems likely this was due to the rise of the structural shell mechanism, for which the shell of the aircraft became the primary structural component. While aircraft still used truss structures like that found in the Wright brother's plane the weight was reduced dramatically by having the shell bare the load. [84] It seems likely that the additional engineering effort to make the shell compliant to actuation while resisting autoloading and the relative ease at which traditional control surfaces could be manufactured resulted in the dormancy of morphing wing research.

Work on compliant morphing wings resumed in the 1980's with Air Force Research Laboratory's (AFRL) the Active flexible wing (AFW) technology project that was using traditional control surfaces to shape a compliant wing. [45] This was eventually followed by the "PARTI" [57] and DAPRA's Smart Wing Project [34] who used smart materials as a means of actuation for the morphing airfoil, irreversibly linking the morphing wing research to the continued development of smart materials. With the turn of the century research in morphing aircraft exploded, in the next few sections we will explore some of the more relevant morphing wing research.

2.2.1 Camber Morphing

Changing the camber of an airfoil is probably the most researched area of morphing wing research. This is because of the dramatic changes that the camber can have on the aerodynamic performance.

One of the most successful Small Business Innovation Research (SBIR) in recent memory has been FlexSys which created a variable camber trailing edge for wings[30] and rotors[29]. The FlexSys system uses an underlying complaint mechanism to control the structural deformation of the airfoil and therefore the camber with a simple rotary actuator. This structure encourages a reduction of stress concentrations and the weight of joints while minimizing backlash. The interface between the stiff wing and the compliant trailing edge is an elastomer membrane. FlexSys was able to demonstrate the effectiveness of their variation of the camber morphing through model test flight and are currently performing full-scale flight systems both of which have yielded positive results.

The spiritual successor at AFRL to the ARW program is the AFRL Variable Camber Compliant Wing (VCCW) which shares a lot of similarities to the FlexSys system. The VCCW is focused on optimization of the variable camber design by combining the leading and trailing edge mechanism, eliminating the need for stretchable skin, while minimizing the energy consumption. The VCCW has been exhaustively studied before flight testing via bench top testing and simulations [46] as well as wind tunnel testing [88] both showing the expected performance increases.

The final camber morphing project that will be highlighted is NASA and Boeing's Variable Camber Continuous Trailing Edge Flap (VCCTEF). The VCCTEF bears some similarities to the AFW project in that it is using the flaps to control the aerodynamic forces and the resultant wing shaping. This is achieved via numerous trailing edge flaps that changed the airfoil camber and are attached to each other via and elastomer filling. The flap actuation is achieved with a slow large displacement using Shape Memory Alloy (SMA) and faster electric drive motors for the outboard flap.[79] The configuration of the actuator results in actuation constraints that much be taken into account. [73] Of the camber morphing technologies presented here the VCCTEF project is one of the only ones that committed a significant effort to investigating the control of the aircraft[54] though additional validation has not been completed beyond simulations.

2.2.2 Flapping Flight

There has been a large amount of research in the area flapping flight. [66] While the field of flapping flight is expansive and robust we will be focusing only on the research relevant to this dissertation in this section. The work relating to relevant modeling techniques are highlighted in Section 2.1.

Much of the flapping flight research has been focused on creating bio-mimetic devices to study the flight characteristics of flying animals. A group from the Department of Integrative Biology at the University of California Berkeley has created an dynamically scaled model of a common fruit fly's wing to study the effects of different patterns of wing strokes. They were able to show that the wing twist during the stroking motion can result in rotational circulation that they theorized can be used as a means of directional control and force modulation.[10] In later works, they were able to show that the wing twist had a significant impact on the lift force in flight, especially when the wing strokes are of small amplitudes. They also revealed that the quasi-steady estimates were limited in its capability of replicating the kinematic patterns,[64] while continuing to expand on the means of quasi-static simulation techniques.[65]

There is ongoing work at AFRL into the control of flapping micro aerial vehicles. Much of the work has focused on the use of split-cycle control to achieve various maneuvers. [83] Split-cycle control uses asymmetric cosine waves as shown in Figure 2.1, where the period and phase of the rising and falling edge are modulated to create asymmetric forces inducing six degrees of freedom control. The work has been focused primarily on creating biomimetic hovering. [12, 56]

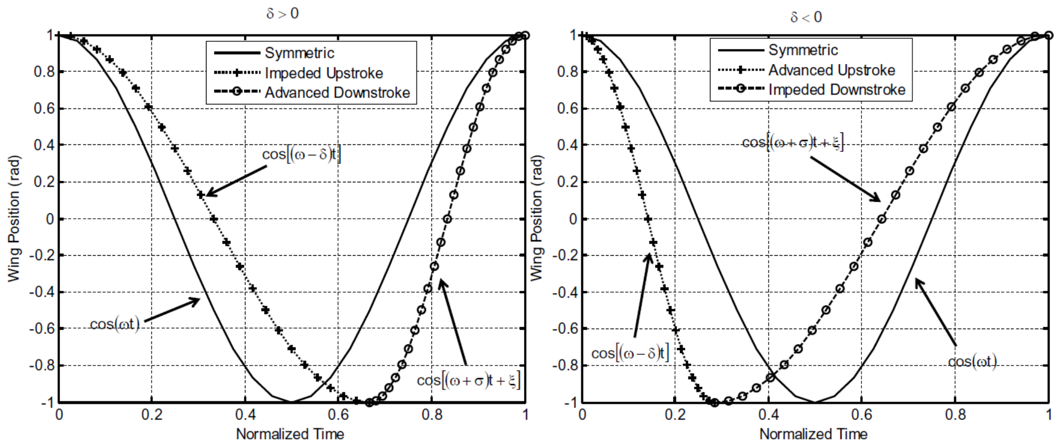

Figure 2.1: Split-cycle example waveform. Figure taken from [83].

2.2.3 Active Twist

The research in this dissertation is focused on the modeling and control of active twist aircraft making the work presented in this section of critical importance. To the author's knowledge, the first known modern investigation of variable twist on a wing was performed by Ferris at NASA Langley. [14] Ferris created a model aircraft with 35^o sweep and the ability to modulate the camber of the leading and trailing edge as well as the sectional twists. In this study, the twist was implemented by having the leading edge camber morphing hinge being more swept than the trailing edge. As a result of the implementation the variable twist the effects of the twist and camber changed could not be de-coupled, and therefore only the camber was investigated.

Unlike the morphing wing field in general investigation into particular active twist technology did not begin until the mid-2000's. This is likely because of the flexibility that camber morphing offers over active twist. Camber also has a conceptual advantage because modern aircraft's aileron, flaps, and slats are intended to replicate variable camber. Keeping that in mind much of the research that was done on active twist has been part of the creation of an entirely adaptable aircraft. This is the case for [50] where Neal *et. al.* created a fully adaptive aircraft that was able to change its span, sweep and tip twist. While they had created an aircraft that was capable of active tip twist when they performed the wind tunnel testing they did not report any of the results from the tip twist focusing instead on the mechanisms that would have the largest most immediate effects on the lift like variable span.

One of the only studies of active twist technology that was flown was by Abdulrahim *et. al.* [2]. They made two different small sized UAV's one with wing curling capabilities and one with wing twisting capabilities they flew both and compared the two aircraft performance. The aircraft wings are not of a typical NACA airfoil like design. Instead, they are more akin to reinforced membranes. The authors noted that it was difficult to achieve system identification of the curling aircraft due to time varying asymmetries, limited data collection, and data quality. They did not attempt to perform the molding on the wing twisting aircraft, but it seems likely that the last two issues remained as well. They were able to show that the wing twist was an effective means of roll control.

Of the previous active twist research, the most relevant to the work presented in this thesis of Majji *et. al.*[42] at Texas A&M and the later work of Vos *et. al.*[80] at the Delft University of Technology. Majji *et. al.* developed a redundant torque tube active twist set-up where the wing box was split into one-third section with a telescoping torque rod in attaching in four places to allow for multiple combinations of the twist. The wing box and torque tube were then skinned using an elastomeric skin. They used Prandtl's lifting line theory as a means to calculated the expected lift coefficient and compare it to the wind tunnel results. They noted in the paper that there were some structural issues with the design, primarily the skin ballooned and dimpled to the point that it was necessary to compensate for those issues in the calculations. They were still able to show the ability to control the lift coefficient with each twist location with the root twist location having the largest effect.

Vos *et. al.*[80] set out to address some of the more common issues with active twist technology as were seen in [42]. The basic premise was that the traditional wing box is not an effective means of inducing twist but that instead the outer shell can be viewed as a torque tube itself and the skin could be addressed by allowing it to be an open tube but with a control mechanism to help with the modulation of the torsional stiffness. They achieved their goal with a clever threaded rod system attached at the trailing edge of the carbon fiber reinforced skin and allowing the skin to slide freely on the ribs which could rotate freely on the spar. For modeling purposes, they used both lifting line and vortex lattice code and then compared the results to wind tunnel tests. They found that the models matched the wind tunnel test relatively well especially at higher angles of attack where the lift induced drag would dominate.

Chapter 3

Modeling

The appropriate modeling of the active twist wing is critical to further exploration of the capabilities of active twist. Due to the nature of active twist, the structure becomes inherently aeroelastic. Aeroelasticity is the coupling of the aerodynamics, the rigid body dynamics of the aircraft, as well as the structural dynamics of the wings. A conceptual diagram of this interaction can be seen in Figure 3.1. The nature of aeroelasticity requires the development of both the structural modeling aspects and aerodynamic modeling with a particular focus on the combination of the two.

3.1 Structural Modeling

One of the primary components of aeroelastic modeling is the structural modeling that will be coupled with the aerodynamics. I used the Galerkin finite element method (GFEM) to model the wing. The GFEM is presented in [15] the basic approach to GFEM is to use an assumed shape that takes a basic spline and use the energetic

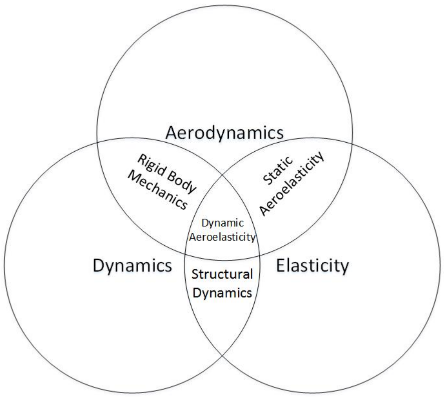

Figure 3.1: Conceptual diagram of the aeroelastic field. This figure is a recreation from [22]

equations to populate the mass and stiffness matrix. For a standard beam bending scenario that we will be eventually extending to a wing structure a Hermite cubic spline was used resulting in the assumed shape in Equation 3.1.

$$\begin{aligned}
&w(x) = f_1(x)w_i + f_2(x)\phi_i + f_2(x)w_{i+1} + f_2(x)\phi_{i+1} \\
&f_1(x) = 1 - \tfrac{3x^2}{l_i^2} + \tfrac{2x^3}{l_i^3} \\
&f_2(x) = x - \tfrac{2x^2}{l_i} + \tfrac{x^3}{l_i^2} \\
&f_3(x) = \tfrac{3x^2}{l_i^2} - \tfrac{2x^3}{l_i^3} \\
&f_4(x) = \tfrac{-x^2}{l_i} + \tfrac{x^3}{l_i^2}
\end{aligned} \tag{3.1}$$

The combined use of Castigliano's theorem and Lagrange's equations of motion yield the mass, damping, and stiffness matrices, which take the general forms presented in Equation 3.2 and 3.3.

$$K_i = E_i I_i \begin{bmatrix} \frac{12}{l_i^3} & \frac{6}{l_i^2} & \frac{-12}{l_i^3} & \frac{6}{l_i^2} \\ \frac{6}{l_i^2} & \frac{4}{l_i} & \frac{-6}{l_i^2} & \frac{2}{l_i} \\ \frac{-12}{l_i^3} & \frac{-6}{l_i^2} & \frac{12}{l_i^3} & \frac{-6}{l_i^2} \\ \frac{6}{l_i^2} & \frac{2}{l_i} & \frac{-6}{l_i^2} & \frac{4}{l_i} \end{bmatrix} \tag{3.2}$$

$$M = \frac{\rho A}{420} \begin{bmatrix} 156l_i & 22l_i^2 & 54l_i & -13l_i^2 \\ 22l_i^2 & 4l_i^2 & 13l_i^2 & -3l_i^3 \\ 54l_i & 13l_i^2 & 156l_i & -22l_i^2 \\ -13l_i^2 & -3l_i^3 & -22l_i^2 & 4l_i^3 \end{bmatrix} \tag{3.3}$$

E_i is the modulus of elasticity, l is the length between the states, and I_i is the second area moment of inertia, all of which are for the i_{th} component of a beam. The stiffness matrix is the same as the damping matrix with the modulus of elasticity replaced with the damping coefficient η.When applying these matrices to to a beam like the one shown in Figure 3.2 each beam section generates its own matrix which add together where the beam sections share their states. Extending this concept to a

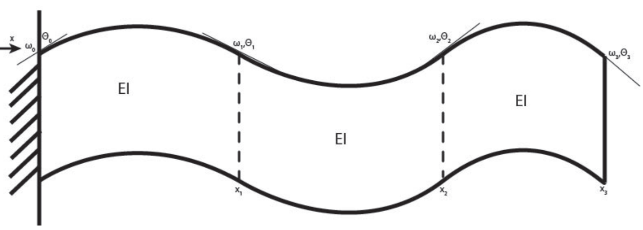

Figure 3.2: Vibrating beam with states and stiffness labeled.

wing results in the configuration shown in Figure 3.3. The Z_i and ϕ_{Z_i} are the states associated with spanwise bending which is defined as the vertical displacement along the spanwise axis. When speaking of a wing the spanwise direction is along the lateral axis. The states X_i and ϕ_{X_i} are associated with the chordwise bending which is defined as the longitudinal displacement along the spanwise axis. The chord of a wing is the straight line connecting the leading and trailing edge of an airfoil, in Figure 3.3 this is along the longitudinal axis. The final states shown are θ_i and ϕ_{θ_i} which are the twist states of the wing about the lateral or spanwise axis. n is the number of sections the wing is split into necessarily causing the number of sets of states to be $n + 1$. This

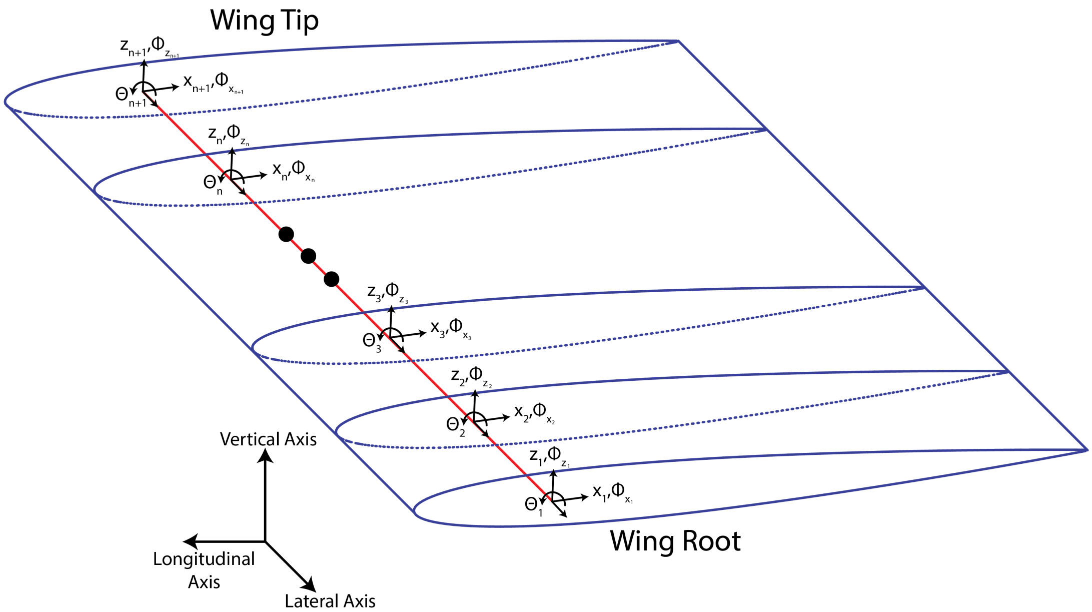

Figure 3.3: Visualization of GFEM model of a wing with spanwise bending, chordwise bending and twist.

configuration has the dynamic equation presented in Equation 3.5

$$X = [Z_1, \phi_{Z_1}, X_1, \phi_{X_1}, \theta_1, \phi_{\theta_1}, \ldots, Z_{n+1}, \phi_{Z_{n+1}}, X_{n+1}, \phi_{X_{n+1}}, \theta_{n+1}, \phi_{\theta_{n+1}}] \tag{3.4}$$

$$M\ddot{X} + C\dot{X} + KX = F \tag{3.5}$$

where going forward F can be populated by the aerodynamic forces.

3.2 Aerodynamics

To generate the aerodynamic forces that we produced by the wing, we decided to use the standard vortex lattice method. The vortex lattice method (VLM) has some distinct advantages over other methods such as lifting line theory and traditional panel methods. VLM is capable of being used on any possible geometry, unlike typical lifting line theory. It also includes the interaction in the spanwise direction unlike many of the traditional panel methods. VLM is also one of the more accurate methods for simulating aerodynamic lift. [6] The biggest disadvantage to VLM is that it does not easily lend itself to viscid calculations. Given our expected application is a mesoscale UAV the viscid effects will likely not be an issue at the operating velocities.

In many ways, the dynamic twist capabilities of the active twist wing are similar to the most general movements that are seen in the flapping wing design. The unsteady vortex lattice method was chosen to model the aerodynamic effects, because of its relatively low computational cost and good accuracy when presented with changing circulations [41, 71, 8]. The main difference between the approach proposed here and the flapping wing research is that, while most flapping flight simulations use exclusively vortex rings which propagate through time, this work uses horseshoe vortices.

The expected operating regime as shown in Figure 3.4 borders on the range where simple high Reynolds number assumptions are valid but are not entirely in the regime that would require the rings. This allows the horseshoes tp be used because the twist sheds vortices solely in the aft direction, but it does so at a rate that prevents wake roll up [28]. With the appropriate aeroelastic adjustments, the horseshoes are a viable means of simulation and are preferred because of their computation efficiency. For reference, a wing with m spanwise sections and n chordwise sections with horseshoes would result in $3m^2n^2$ calculations per a time step while for rings it would be between $4m^2n^2$ and $32m^2n^2$ computations depending on the time step and the number of chord lengths the user deems necessary.

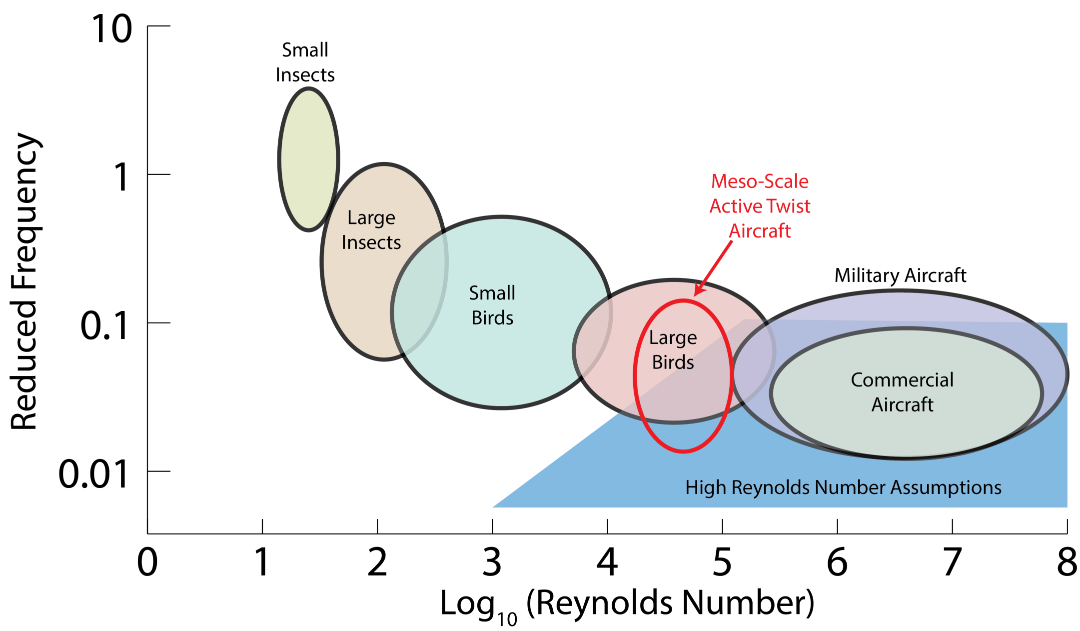

Figure 3.4: Operating regimes of flying animals and human built aircrafts and the region where high reynolds number assumptions are applicable. The information was taken from [47]

These horseshoe vortices interactions are what creates the spanwise variation of the circulation about the wing. Figure 3.5 shows the set up for the VLM with the horseshoe vortices centered about the three quarter chord axis and the horizontal component of the horseshoe on the quarter chord axis. The horizontal vortex can be thought of as the circulation about the airfoil while the longitudinal vortices are the trailing vortices that satisfy Helmholtz vortex theorem requiring that a bound vortex does not change strength unless a separate vortex splits that is equal to the change in circulation.

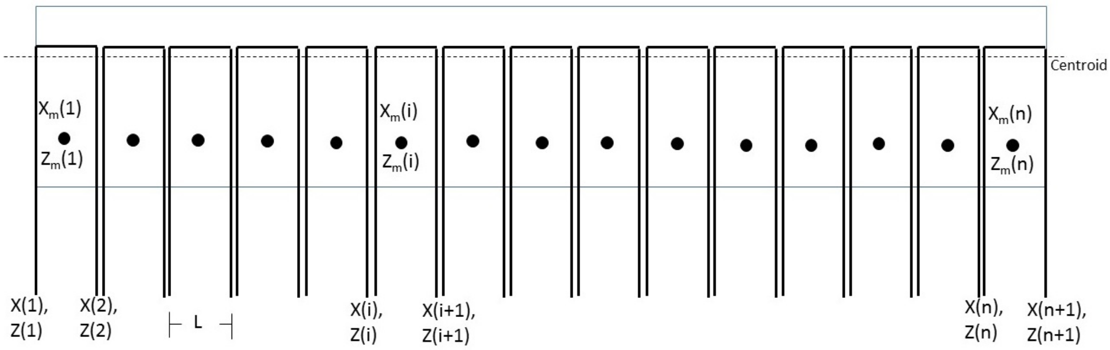

Figure 3.5: VLM finite element horseshoe vortices with constant distances and centered about the three quarter cord line

When comparing Figure 3.5 to Figure 3.3 it can be seen how the VLM readily lends itself to the preexisting GFEM solid mechanics model. This was one of the reasons that the VLM was chosen to generate the aerodynamic forces, it has also already been shown to be a viable method for modeling aeroelastic effects in [52, 54, 53, 51]. While there are numerous prepackaged VLM softwares available we opted for writing a custom one primarily to have a base to build some of the proposed work that will be covered later. We based the VLM that we wrote off of the equations and methodology presented

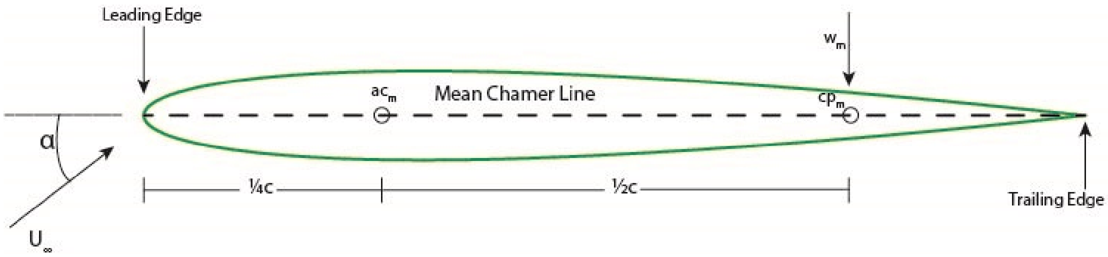

Figure 3.6: The angle of attack, α, is the angle between the normal vector and the air velocity vector. For the symmetric airfoil the aerodynamic center is located at the quarter chord.

in [6] with some auxiliary content taken from [36]. VLM uses Equation 3.6 coupled with the boundary conditions provided in Equation 3.7 to determine what the circulation about the airfoil is at a given control point m.

$$\vec{V} = \vec{C}\Gamma_n \tag{3.6}$$

$$-u_m sin\delta cos\chi - v_m cos\delta sin\chi + w_m cos\chi cos\delta + U_\infty sin(\alpha - \delta) cos\chi = 0 \tag{3.7}$$

where $\vec{V}$ is the generalized velocity vector at all the control points m, $\vec{C}$ is the geometry matrix that VLM generates from the current wing geometry, Γ is the circulations at the control points. u_m, v_m, and w_m are the local velocities at the control point m in the longitudinal, lateral and vertical directions respectively. U_∞ is the air speed, δ is the slope of the mean chamber line at the control point, χ is the dihedral angle, and α is the angle of attack. Figure 3.6 shows the mean chamber line which for a symmetric airfoil causes the slope of the mean chamber line, the δ, to be equal to zero. Figure 3.6 also shows the angle of attack which is defined as $\frac{w_m}{U_\infty}$ where w_m is the vertical induced velocity at the control point. Figure 1.1 shows the front view of a wing showing the dihedral angle.

In order to combine and apply Equations 3.6 and 3.7 $\vec{C}$ needs to be generated. For each directional velocity in Equation 3.7 a separate $\vec{C}$ can be generated by finding the velocity that each Γ generated at a given control point. Each control point was chosen to be located at the three quarter chord and halfway between each spanwise GFEM element on the upper surface of the wing. Equations 3.8, 3.9, 3.10 show how to populate the m, n_{th} cell of matrix $\vec{C}$.

$$\begin{aligned}
&u_m = [(y_m - y_n)(z_m - z_{n+1}) - (y_m - y_{n+1})(z_m - z_n)]/ \\
&\{((y_m - y_n)(z_m - z_{n+1}) - (y_m - y_{n+1})(z_m - z_n))^2 \\
&+((x_m - x_n)(z_m - z_{n+1}) - (x_m - x_{n+1})(z_m - z_n))^2 \\
&+((x_m - x_n)(y_m - y_{n+1}) - (x_m - x_{n+1})(y_m - y_n))^2\}
\end{aligned} \tag{3.8}$$

$$\begin{aligned}
&v_m = -[(x_m - x_n)(z_m - z_{n+1}) - (x_m - x_{n+1})(z_m - z_n)]/ \\
&\{((y_m - y_n)(z_m - z_{n+1}) - (y_m - y_{n+1})(z_m - z_n))^2 \\
&+((x_m - x_n)(z_m - z_{n+1}) - (x_m - x_{n+1})(z_m - z_n))^2 \\
&+((x_m - x_n)(y_m - y_{n+1}) - (x_m - x_{n+1})(y_m - y_n))^2\} \\
&+\frac{z_m - z_n}{4\pi((z_m - z_n)^2 + (y_n - y_m)^2)}\left[1 + \frac{x_m - x_n}{\sqrt{(x_m - x_n)^2 + (y_m - y_n)^2 + (z_m - z_n)^2}}\right] \\
&+\frac{z_m - z_{n+1}}{4\pi((z_m - z_{n+1})^2 + (y_{n+1} - y_m)^2)}\left[1 + \frac{x_m - x_{n+1}}{\sqrt{(x_m - x_{n+1})^2 + (y_m - y_{n+1})^2 + (z_m - z_{n+1})^2}}\right]
\end{aligned} \tag{3.9}$$

$$
\begin{aligned}
w_m = {} & [(x_m - x_n)(y_m - y_{n+1}) - (x_m - x_{n+1})(y_m - y_n)]/ \\
& \{((y_m - y_n)(z_m - z_{n+1}) - (y_m - y_{n+1})(z_m - z_n))^2 \\
& +((x_m - x_n)(z_m - z_{n+1}) - (x_m - x_{n+1})(z_m - z_n))^2 \\
& +((x_m - x_n)(y_m - y_{n+1}) - (x_m - x_{n+1})(y_m - y_n))^2\} \\
& +\tfrac{y_m - y_n}{4\pi((z_m - z_n)^2 + (y_n - y_m)^2)}\left[1 + \tfrac{x_m - x_n}{\sqrt{(x_m - x_n)^2 + (y_m - y_n)^2 + (z_m - z_n)^2}}\right] \\
& +\tfrac{y_m - y_{n+1}}{4\pi((z_m - z_{n+1})^2 + (y_{n+1} - y_m)^2)}\left[1 + \tfrac{x_m - x_{n+1}}{\sqrt{(x_m - x_{n+1})^2 + (y_m - y_{n+1})^2 + (z_m - z_{n+1})^2}}\right]
\end{aligned}
\tag{3.10}
$$

These equations represent the application of Biot-Savart law to the horse finite element horseshoes. The substitution of Equations 3.8, 3.9, 3.10 into Equations 3.6 and 3.7 yield a system of equations that can be solve simultaneously by matrix inversion.

Equations 3.8, 3.9, 3.10 are the closed form solution for a vortex line going to infinity, but it is not necessary to calculate beyond seven wing spans due to the inverse squared components of the equation. I used an adaptation of Tornado that uses the finite solution to the Biot-Savart law for its computational speed and flexibility.[44]

3.3 Aeroelastic

From a practical implementation perspective, since the GFEM axial stretching and compressing were ignored all the components associated with y are constant. The other variables z and x vary with the spanwise and chordwise deflections presented earlier. With the control points being placed between the GFEM states and allowing the edges of the horse shoe's to be put on the GFEM states a number of control points can be taken from $\lfloor \frac{2(n+1)}{5} \rfloor$ for having a control point and the edges of the horseshoe placed at GFEM states to n. The control point spanwise and chordwise deflections can be estimated with the cubic spline from Equation 3.1 and then added to the initial geometric parameters of the wing to generate z_m and x_m.

The exchange of position vectors between the solid mechanics and the aerodynamics does not represent the totality of the coupling in an aeroelastic system. Indeed the primary means of interaction between the two components if the aerodynamic forces that are applied to the wing. Utilizing the vortex lattice method we were able to generate the circulation at each control point. The circulation directly corresponds to the lift and vortex-induced drag forces as shown in Equations 3.11 and 3.12.

$$l(y) = \rho_\infty U_\infty \Gamma(y) \tag{3.11}$$

$$d(y) = tan(\theta(y) + \alpha_{root}) l(y) \tag{3.12}$$

where θ is the twist of the wing at a given location y and α_{root} is the angle of attack at the root of the wing. It is assumed that the air velocity is constant in the spanwise direction. Because the control points are placed between GFEM states the force due to circulation does not directly apply to the state equation presented in 3.5. To address this, we simply split the forces equally to each adjacent states. The generated force vector can then be put into Equation 3.5 to complete the current iteration of this aeroelastic modeling.

The coupling of the aerodynamic states to the structural states allows for the creation of a static aeroelastic simulation tool, which is useful especially in the preliminary design and development stages but in some cases, it is necessary to have a full dynamic aeroelastic model using an unsteady vortex lattice method.

The wing is divided into m panels and calculates the aerodynamic forces/moments at each panel. Furthermore, we assume that the sectional element defined earlier coincides with the panel section, and we define q collocation points around each panel section.

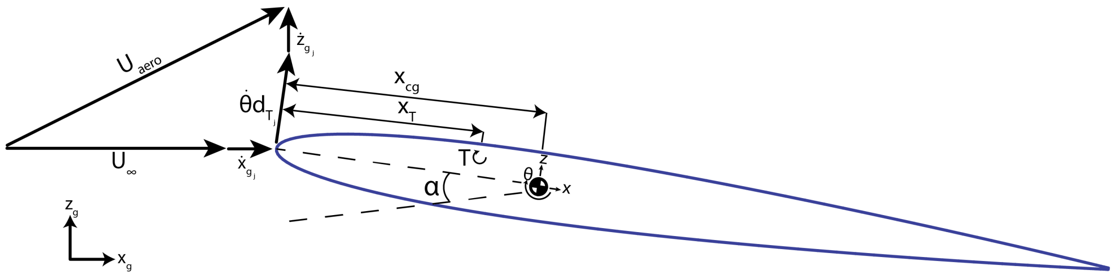

Figure 3.7: Aeroelastic definitions

The local aeroelastic wind velocity vector at each collocation point can is shown in Figure 3.7 and can be given by

$$U_{i,j} = R(\alpha_{root}) \begin{bmatrix} U_\infty & 0 \end{bmatrix}^T + R(\theta_i) \begin{bmatrix} \dot{\theta}_i |d_j| & 0 \end{bmatrix}^T + \begin{bmatrix} \dot{x}_{i,j} & 0 \end{bmatrix}^T + \begin{bmatrix} 0 & \dot{z}_{i,j} \end{bmatrix}^T \tag{3.13}$$

for , $i = 1, \cdots, m$, $j = 1, \cdots, q$ where $R(\cdot)$ denotes a 3×3 rotational matrix, α_{root} is the angle of attack at the wing root, U_∞ is the airspeed, $|d_j|$ is the magnitude of the position vector d_j from torque tube axis to collocation point j, θ_i is the twist angle at ith panel, and $\dot{\theta}_i$ its rate, $\dot{x}$ is the rate of chordwise displacement, and $\dot{z}$ is the rate of spanwise displcacement. We should note that the local wind velocity $U_{i,j}$ defined in (5.81) is a tall matrix of dimension $mq \times 3$. To simplify the subsequent presentation, we rewrite its notation to be just U_i, where $i = 1, \cdots, mq$. Then, the local aeroelastic angle of attack at each collocation point can be determined by

$$\alpha_i = \tan^{-1}\left(\frac{U_{iz}}{U_{ix}}\right), \ i = 1, \cdots, mq \tag{3.14}$$

Similarly, the local sideslip angle at section i, β_i, is given by

$$\beta_i = \tan^{-1}\left(\frac{U_{iy}}{U_{ix}}\right), \ i = 1, \cdots, m \tag{3.15}$$

where U_{iy} is the y component of U_i.

where U_{ix} and U_{iz} denote the x and z components of U_i.

The circulation equation can be solved in its standard form as [44]

$$\begin{cases} C_x \Gamma_x &= B_x \\ C_y \Gamma_y &= B_y \\ C_z \Gamma_z &= B_z \end{cases} \tag{3.16}$$

where Γ_x, Γ_y, and Γ_z are the vectors of dimension mq and denote the circulation of mq collocation points in (x, y, z) coordinates. The matrices C_x, C_y, and C_z contain entries of influence coefficients that result form the geometry of the horseshoe vortex on collocation points in (x, y, z) coordinates. The details on the influence coefficient matrix can be found in [44]. Furthermore, the boundary conditions $\mathbf{B} = [B_x \ \ B_y \ \ B_z]$ are given by

$$\mathbf{B}_i = \begin{bmatrix} U_{ix}\cos(\alpha_i)\cos(\beta) \\ -U_{iy}\cos(\alpha_i)\sin(\beta) \\ U_{iz}\sin(\alpha_i) \end{bmatrix}^T, \ i = 1, \cdots, mq \tag{3.17}$$

where α_i is given in (5.82) and β is the aircraft sideslip angle. Let $\mathbf{\Gamma} = [\Gamma_x \;\; \Gamma_y \;\; \Gamma_z]$, then we can solve for $\mathbf{\Gamma}_i$ by substituting (3.17) into (3.16). Therefore, the total aerodynamic forces and moments on the digital wing can be derived from each panel as

$$F = \rho_\infty \sum_{i=1}^{mq} (\mathbf{B}_i \otimes \mathbf{\Gamma}_i) \tag{3.18}$$

and

$$M = \rho_\infty \left[\sum_{i=1}^{mq} (d_i - m_c) \otimes (\mathbf{B}_i \otimes \mathbf{\Gamma}_i) \right] \tag{3.19}$$

where ρ_∞ is the air density, d_i the ith collocation point position vector, m_c the position vector to the center of gravity, and $\otimes$ denotes the vector cross product. It should be noted that the sectional aerodynamic forces and moments from (3.18) and (3.19) are coupled with the structural dynamics described in (3.5). Finally, the total aerodynamic lift (L), drag (D), and lateral force (S) can be given by

$$\begin{bmatrix} D \\ S \\ L \end{bmatrix} = R(\alpha_{root}) R(\beta) \begin{bmatrix} F_{ax} \\ F_{ay} \\ F_{az} \end{bmatrix} \tag{3.20}$$

where $F = [F_{ax} \;\; F_{ay} \;\; F_{az}]^T$.

Chapter 4

Active Twist Wing Design

For the development of the control of an active twist wing, it is necessary to have a platform to work from. For this purpose, we have two different active twist wings designs that were made by two different collaborators. The first active twist wing is a lattice-based design that informed wing simulations to create a holistic design process and was manufactured by collaborators at NASA Ames. The second active twist wing is a polystyrene hollow core design created by collaborators at Aurora Flight Sciences.

4.1 Composite Lattice-based Cellular Structure Active Twist Wing Design

The ability of composite lattice-based cellular structure to form complex geometries with anisotropic material properties is an enabling technology for morphing wing flight. Figure 4.1 shows the active twist wing mounted in the wind tunnel with the actuation mechanism highlighted.

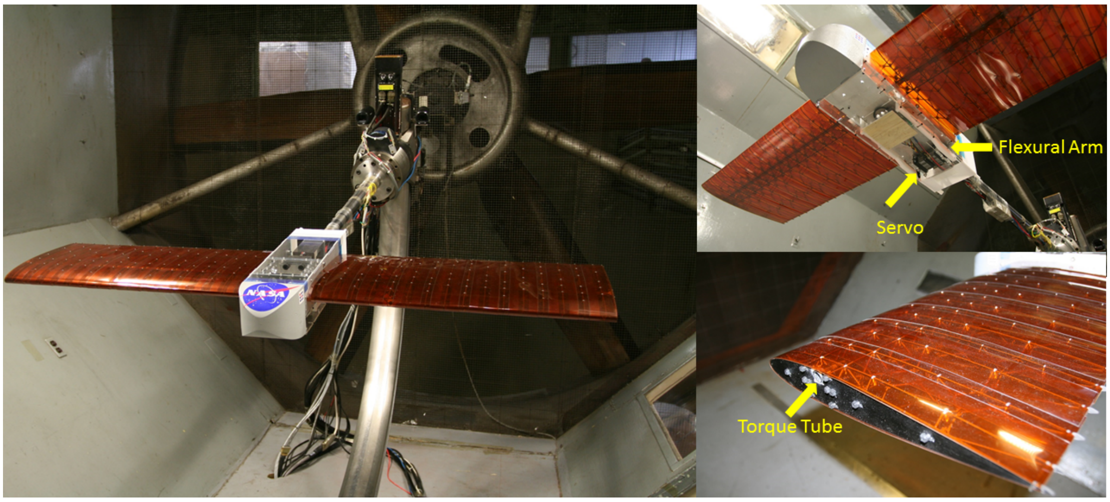

Figure 4.1: Wind tunnel test setup for a digital wing model.

With any wing application where it is potential for large displacements there is a common problem with the skin of the wing. The wing skin is the layer that has direct contact with the air. The problem with wings that have large displacements is that instabilities in the skin result in buckling and ridges or dimpling of the skin, all of which increase the friction and therefore drag of the plane. A more recent approach has been proposed to make the skin be applied in sections with the bending and twist allowances coming from the joints.

One of the necessary steps to doing this is to determine the size of a given patch that will not result in significant displacement of the skin during normal operating conditions. To address this problem we combined the VLM method we presented earlier with the standard panel method Xfoil. Figure 4.2 shows the flow chart representing the combination of VLM and Xfoil where VLM coupled with the GFEM result in a lift coefficient that is then passed to Xfoil. Xfoil then generates a pressure profile for each spanwise lift coefficient that was generated by the VLM.

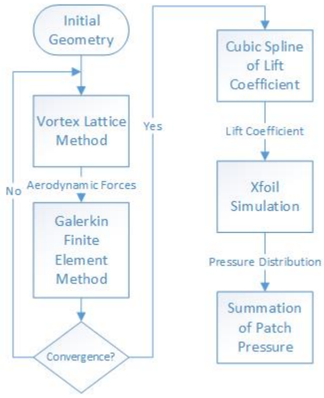

Figure 4.2: The initial geometry is given to the VLM which generates the aerodynamic forces that are then passed to the GFEM for static analysis. If the geometry that results from the GFEM converges then a cubic spline is used to create a lift coefficient for every millimeter. Those lift coefficients are then passed to Xfoil which generates the pressure distribution around the airfoil for each section.

In order to determine the necessary size of the patch the maximum pressure is assumed to the be the center of the patch. The pressures generated by Xfoil within the specified patch size are summed for each pressure profile generated from independent lift coefficients within the specified patch size. Figure 4.3 shows the average patch pressure with respect to angle of attach and patch size. The shape of the curve is not symmetric about the zero angle of attack because as the angle of attack is negative the induced drag changes direction. Figure 4.4 shows the maximum displacement normalized for material and geometric constants, of a patch plotted against the patch size and angle of attack. The patch displacement was determined using the navier solution to the Kirchoff-Love plate theory assuming that the average pressure from Figure 4.3 is constant across the patch. Since the wing can be assumed to be a flat plate in many situations this assumptions should be valid as well and result in equation 4.1.

$$w(x,y)D = \sum_{m=1}^{\infty}\sum_{n=1}^{\infty}\frac{16P_0}{(2n-1)(2m-1)\pi^6}\left[\frac{(2m-1)^2}{a^2}+\frac{(2n-1)}{b^2}\right]^{-2}\frac{sin(2m-1)\pi x}{a}\frac{sin(2n-1)\pi y}{b} \tag{4.1}$$

where,

$$D = \frac{2h^3E}{3(1-\nu)} \tag{4.2}$$

where, h is the depth of the plate, E is the modulus of elasticity, and ν is poisson's ratio. It is desirable to have the largest possibly patch size possible prior to the normalized displacement values becoming dependent on angle of attack. Figure 4.4 shows this to be around $30mm$.

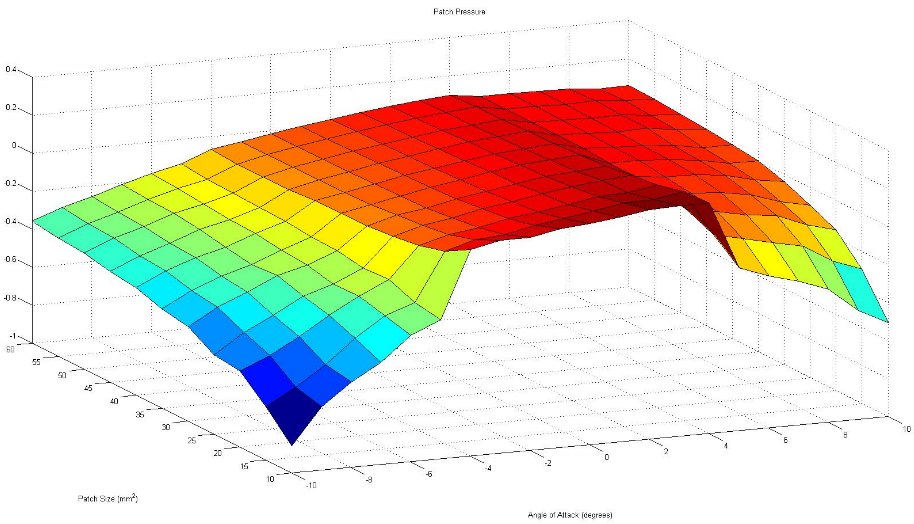

Figure 4.3: The average patch pressure plotted against the angle of attack and patch size.

Now that the lattic pitch size has been determined the rest of the wing design can proceed. The wing was designed and built by Benjamin Jennett details of the design

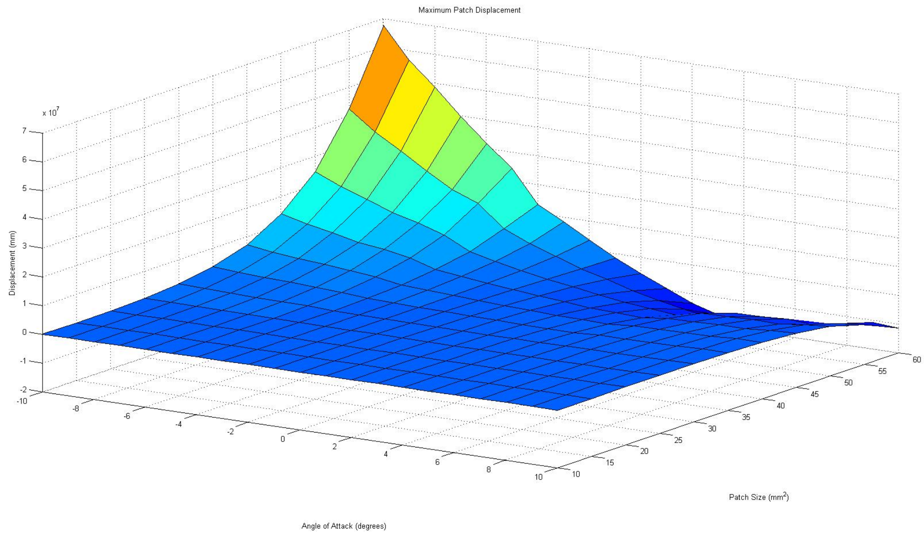

Figure 4.4: The maximum displacement of an assumed thin plate with the average pressure applied from Figure4.3

can be found in [24]. The basics of the wing design will be included here for completeness. Figure 4.5 shows the internal structure of wing. The cellular structures internal to the wing are created out of seven unique pieces and are formed of two primary geometries a cubic octahedron (cuboct) and a rhombic dodecahedron, also known as kelvin lattice, where the cubocts make up the rigid center with the lattice pitch determined above. The kelvin lattice makes up the trailing edge and has twice the pitch lattice that the cuboct section does allowing for the twist capabilities. The material properties for the carbon fiber reinforced polymer that the wing components were made out of can be seen in Table 4.1.

The active twist was achieved using a servo driven torque tube with a flexural arm to gain mechanical advantage an apply the appropriate amount of torque. The servo is mounted internally to the fuselage and acts as a means of redistributing the

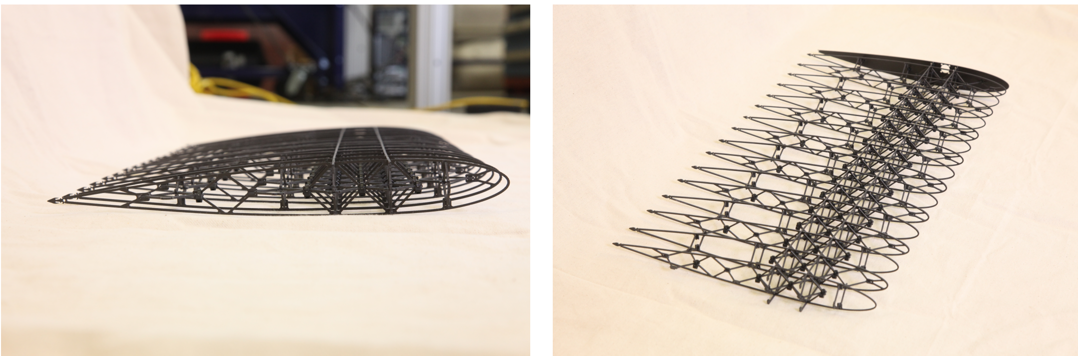

(a) Side View (b) Tri-Iso View

Figure 4.5: The internal structure of the wing is made from seven unique quasi isotropic carbon fiber components that were reversibly assembled as show in (a) and (b)

Table 4.1: Carbon Fiber Reinforced Polymer Properties

Parameter	Value
Layup Orientation	$0, 45, 90, 0, -45, -90, -45, 0^o$
Sheet thickness	$0.600'' + / - 0.005''$
Density	$1600kg/m^3$
Young's Modulus (E)	$25 - 28Gpa$

weight of the aircraft, further details on the actuation mechanism can be found in [24].

4.2 Polystyrene Hollow Core Wing Design

Our collaborators at Aurora Flight Sciences designed and built the wing in Figure 4.6 using fast construction methods, in particular, a thermoplastic layer over a polystyrene hollow core wing. With the design constraints associated with the manufac-

Figure 4.6: Twist capable and outfitted with an actuation system that enabled in-flight active twist demonstration

turing process, it was decided that it was necessary to make a geometrically insensitive airfoil, which they tested using XFOIL. The geometrically insensitive airfoil is important from a modeling preservative for active twist because twist induced warping requires more computation and provides another variation to consider. Knowing this we performed benchtop testing to confirm that the aerodynamic properties of the airfoil do not change with the twist.

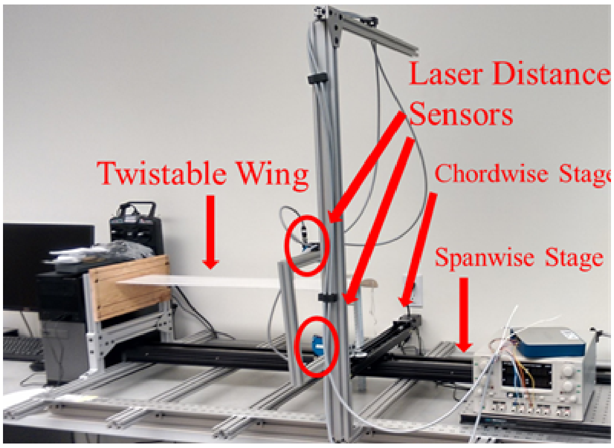

Figure 4.7: Airfoil measurement benchtop testing rig

The benchtop testing to confirm the airfoil properties did not change with the twist was done by scanning the cross section of the wing at various twist degrees and then using XFOIL to inspect the twist aerodynamic properties. The test rig used is shown in Figure 4.7. The laser distance sensors were placed on a C structure which was mounted on a linear stage to scan the chordwise directions while that was mounted on another stage to scan the spanwise direction. The scanning results can be seen in Figure 4.8 and they show that there are minimal changes in the airfoil shape.

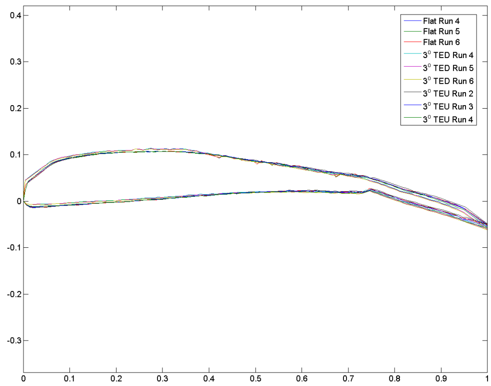

Figure 4.8: Comparison of airfoil profile for different amounts of twist

Figure 4.9 shows the lift profile for the measured airfoils, which are grouped fairly tightly, giving us confidence that the assumption that the limited warping does to tip twist has little effect on the airfoil performance. The lift profiles were used as means of aerodynamic comparison because they are the aerodynamic parameters which are less susceptible to extraneous variations due to the combination of small inconsistencies in the experimental setup combined with the numeric requirements of XFOIL. [13]

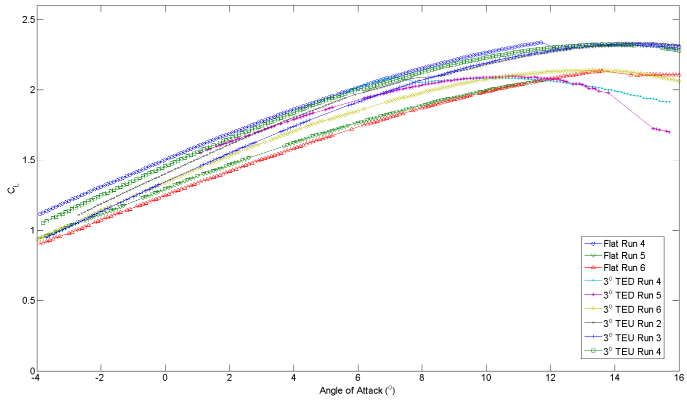

Figure 4.9: XFOIL comparison of lift profile for measured airfoils

With the completion of the design of the active twist wings, it is important to test and validate the capabilities of the developed active twist wings.

4.3 Wind Tunnel Testing

The wind tunnel testing was performed at the NASA Langley 12-Foot Atmospheric, closed throat, annular return wind tunnel a graphic of the wind tunnel. Figure 4.10 shows the active twist aircraft mounted in the wind tunnel.

The methodology for wind tunnel testing was to assess the performance of the flexible design for a range of speed, angle of attack, and sideslip conditions with the wing twist angles deflected symmetrically and differentially. For comparison purposes, a similar matrix of conditions was tested using a rigid model with identical (neutral) outer model line geometry shown in Figure 4.11. Flaperons were included on the rigid model to represent typical symmetric and differential control surfaces for comparisons

Figure 4.10: Active twist wing mounted in the wind tunnel

to the flexible model undergoing commanded twist deflections. The rigid model was 3D printed from polycarbonate using the Fused Deposition Modeling process since the tests were aimed at measuring the aerodynamic properties and the extra weight was not a concern. During the test campaign, two copies of the flexible structure were tested.

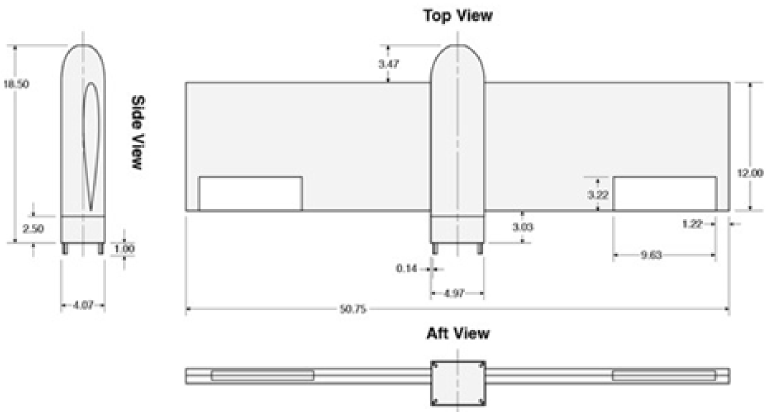

Figure 4.11: Design parameters for rigid model. The outer mold lines in the flat actuator trim condition are identical for the control and active twist models. Displayed dimensions are in inches.

4.4 Results and Validation

The wind tunnel testing was broken into two parts the static test and the dynamic test. The static tests are defined as wind tunnel test where neither the active wing twist or the model was subjected to forced oscillations.

4.4.1 Static Wind Tunnel Results

During the static wind tunnel testing, many different configurations were tested. In this section, the results for a range of angle of attack, angle of sideslip, dynamic pressure, and wing twist (or control surface) deflection are covered. In each configuration and test, we are also validating and comparing our simulations, all of the parameters for which can be found in Table 4.2

4.4.1.1 Symmetric Twist

The first experiments performed in the wind tunnel were symmetric static tests with varying angles of attack, followed by symmetric flaperon deflection angles (labeled flap in the graphics) or tip twist in the case of the flexible models. Looking at Figure 4.12, there is significant of overlap between the results for each model, as would be expected due to the overall geometric similarities. It can also be seen that the 10^o Flap curve (Figure 4.12 a) is very close to the 6^o TipTwist curve (Figure 4.12 b), suggesting that there is a proportionality between the control effectiveness of two models.

The similarity of the 6^o Tip Twist and 10o Flap results warrants closer inspection. Figure 4.13 compares the lift and drag curves for the two flexible models (labeled

Table 4.2: Shape and material parameters for VLM simulation

Parameter	Value
Half Span	$0.5795m$
Wing Cord	$0.3048m$
Body Width	$0.126238m$
Body Cord	$0.3048m$
Number of Spanwise Wing Panels	32
Number of Spanwise Body Panels	4
Number of Cordwise Panels	8
Rotational Area Moment of Inertia	$3.8918e^{-05}m^4$
Cross Sectional Area	$0.0076m^2$
Shear Modulus	$.169MPa$
Density	$0.01543\frac{kg}{m^3}$

Flex 1 and Flex 2), the rigid model, and the VLM simulation results of 6^o of tip twist. From Figure 4.13 it can be seen that all of the lift curves are very similar until the higher angles of attack, where the Flex 2 model has a little higher lift than the Flex 1, while the simulation predicts a little less. The biggest difference is in the drag curve, where at the lower angles of attack, the simulation agrees well with the wind tunnel results. However, the lack of accounting for the presence of the center body, and possibly viscous effects, cause the simulation results to diverge at an angle of attack of approximately

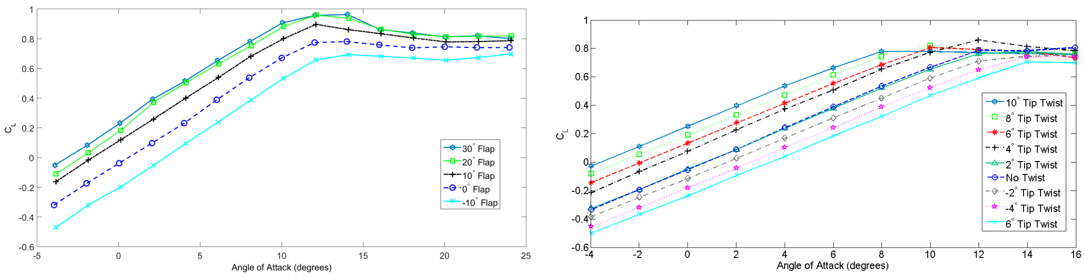

(a) Rigid model

(b) Flexible model

Figure 4.12: Coefficient of lift curves

two degrees. Before stall, the rigid model data also show a lower drag coefficient. In the results that follow, no distinction is made between the results for Flex 1 and Flex 2, and are simply referred to as flexible model results.

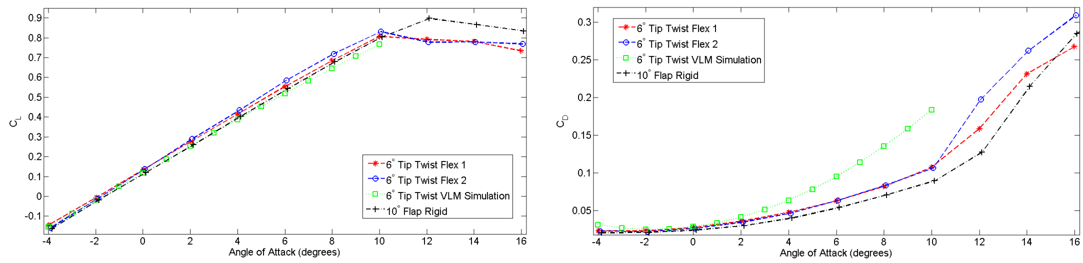

(a) Lift Curve

(b) Drag Curve

Figure 4.13: Comparing the lift and drag curves of the rigid model, flexible models, and VLM simulations

Figure 4.14 shows the drag curves for the flexible and rigid model types. In general, the drag coefficient of the flexible model is higher at lower angles of attack. For the equivalent control effectiveness, deflections of 10^o for the rigid model and 6^o for the flexible model, the drag data are very similar at the higher, yet pre-stall, angles of attack.

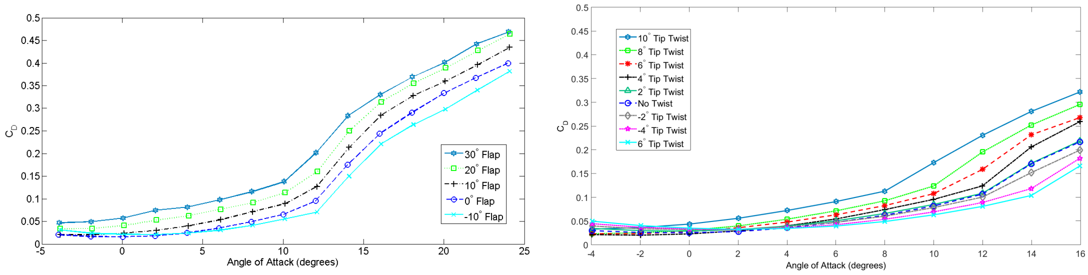

(a) Rigid model (b) Flexible model

Figure 4.14: Coefficient of drag curves

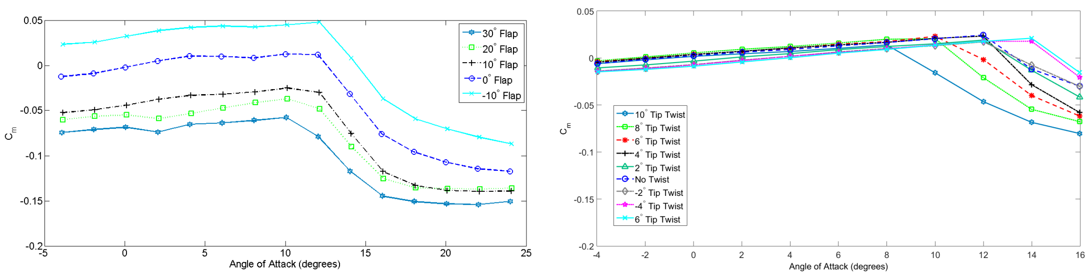

(a) Rigid model (b) Flexible model

Figure 4.15: Pitching moment coefficient curves

Due to the configuration of the models (tailless, unswept flying wing without a reflexed camber line), it is not surprising to see Figure 4.15 show that both models are unstable at low angles of attack. With no camber, a fuselage, and no tail, low or unstable static pitch stability is to be expected. Note that the flexible model is approaching marginal stability and the addition of a tail with minimal tail volume could easily make it stable. This also suggests that the design goal of mitigating the amount of airfoil warping was successful because the pitching moment coefficient is very similar to what we would expect for a symmetric airfoil. One important part of the research

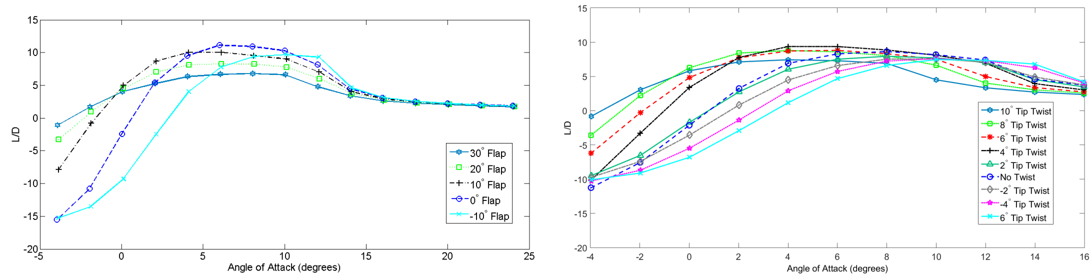

(a) Rigid model

(b) Flexible model

Figure 4.16: Lift over Drag curves

was to determine the capabilities of the active twist system to improve efficiency over an extensive range of flight conditions. Figure 4.16 shows the lift-over-drag curves for the rigid and flexible models. The maximum lift-to-drag ratio for the rigid model is slightly higher than that of the flexible models; however, the maximum lift-to-drag ratio for the rigid model comes solely from the 0^o Flap configuration. That is not the case for the flexible model, where most of the tested configurations reach the maximum efficiency of the no-twist configuration, and some of them exceed it. In fact, the 4^o Tip Twist configuration has the highest lift-to-drag ratio for the flexible model. This suggests that for particular combinations of required lift and angle of attack, the flexible model would be more efficient than the rigid model and would be uniformly more efficient if the skins were comparable.

4.4.1.2 Asymmetric Twist

In this section, we will be focusing on the ability to generate roll and yaw moments. This is achieved primarily through asymmetric flaperon deflection (labeled aileron in the graphics) for the traditional rigid model and asymmetric twist for the flexible lattice model.

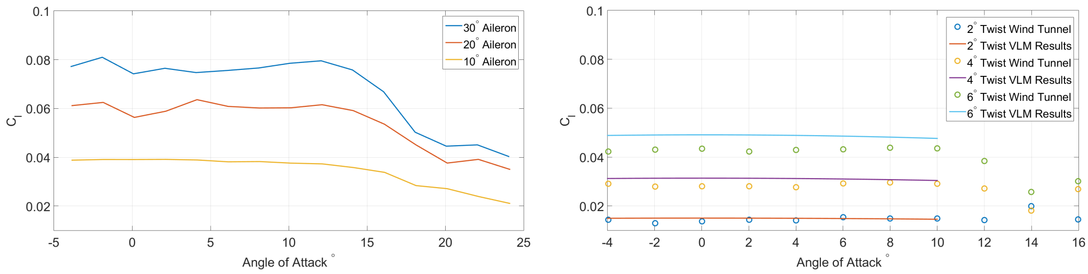

(a) Rigid model (b) Flexible model

Figure 4.17: Roll characteristics at varying A) aileron angle (for rigid model) and B) wing tip twist angle (for flexible model and simulation model), as a function of angle of attack. (dynamic pressure = 2 psf)

The rigid model was tested at various dynamic pressures, from 2 psf to 4 psf, with a sweep of the angle of attack from 4^o to 24^o and asymmetric flaperons at 10^o, 20^o, and 30^o deflected with the left device trailing edge down and the right device trailing edge up by the same deflection angle (equal and opposite in a direction to nominally produce a right-wing-down rolling moment). The flexible lattice wing model was tested over the same range of dynamic pressures but over a range of angle of attack from 4^o to 16^o with asymmetric wing twist of 2^o, 4^o, and 6^o with two exceptions: For the dynamic pressure of 3 psf there is no 4o wing twist; for the dynamic pressure of 4 psf the angle of attack only goes up to 10^o. The flexible-wing deflections were also equal and opposite in the same sense as described above. At a dynamic pressure of 2 psf, Figure 4.17 shows the incremental rolling moment coefficient of the rigid model and the flexible lattice wing model calculated by subtracting the neutral deflection data from the deflected cases. The various twist angles result in easily distinguishable rolling moment coefficients, ranging from approximately 0.015 to 0.045, and the simulation model compares reasonably well with the wind tunnel results, particularly in the lower twist angles. Furthermore, the roll coefficient magnitude of the 6^o twist is comparable to the 10^o flaperon deflection case. This gives some proportionality to the amount of twist that would be needed to replicate the roll performance of flaperons.

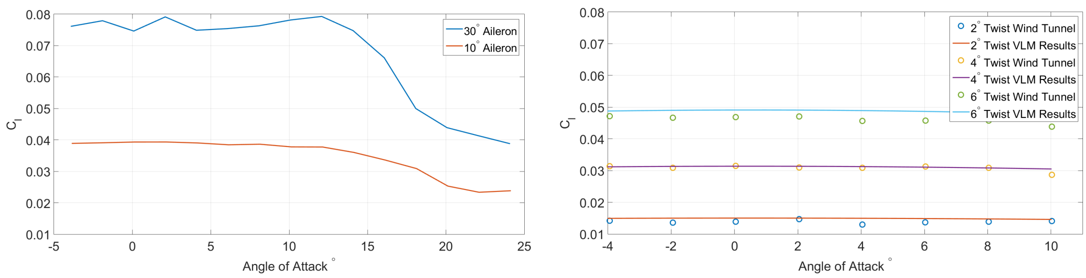

(a) Rigid model

(b) Flexible model

Figure 4.18: Roll characteristics at varying A) aileron angle (for rigid model) and B) wing tip twist angle (for flexible model and simulation model), as a function of angle of attack. (dynamic pressure = 3 psf)

Figures 4.17, 4.18 and 4.19 further indicate that the magnitude of the rolling moment coefficients for the rigid model does not change with increasing dynamic pressure, whereas for the flexible model, the rolling magnitude continues to grow and begins to converge to the simulation results. We can expect that the simulation results will act as an effective upper bound for the performance of the flexible lattice wing. This is because the VLM method does not include the fuselage, so the magnitude and the slope of the lifting line for a given wing is always optimistic which then is passed to the rolling cases when the twist is asymmetric. It is valuable to note that as the dynamic pressure increases the flexible lattice wing performs better. This means that at the same altitude but higher speeds the roll authority will be increased.

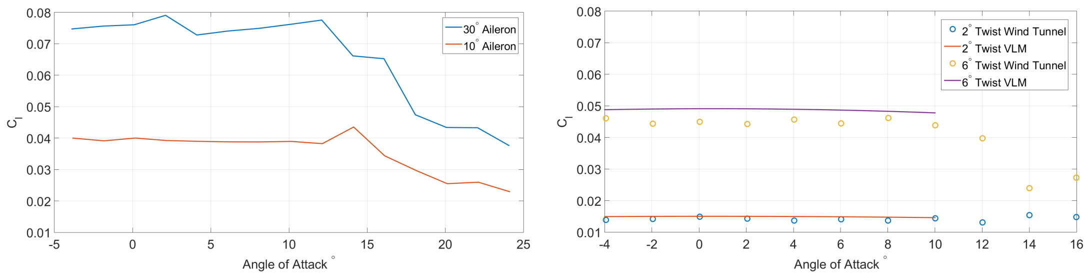

(a) Rigid model

(b) Flexible model

Figure 4.19: Roll characteristics at varying A) aileron angle (for rigid model) and B) wing tip twist angle (for flexible model and simulation model), as a function of angle of attack. (dynamic pressure = 4 psf)

Figure 4.20 shows the yawing moment coefficients for the rigid model and the flexible model at a dynamic pressure of 2 psf with surfaces deflected in a similar manner as for the prior asymmetric cases. Note that while the peaks of the yawing moment coefficients are larger in magnitude for the rigid model than the flexible model over the same range of angle of attack, the yawing moment coefficient for the 10^o flaperon deflection is minimal in the angle of attack range of 0 to 12^o for the rigid model. Above this range and for the larger flaperon deflections, the results in Figure 4.20 are a mix of proverse and adverse moments which would complicate achieving lateral-directional control harmony with the rigid model. Note that there is a substantial difference in the magnitude and shape of the curves for the two models. The rigid model is much more jagged; on the other hand, C_n of the flexible model is clearly nearly linear across the angle of attack range tested. The flexible wing exhibits adverse yawing moments arising from drag induced by the asymmetric lift levels of the left and right wings, but the levels are mild and smoothly vary the angle of attack increases.

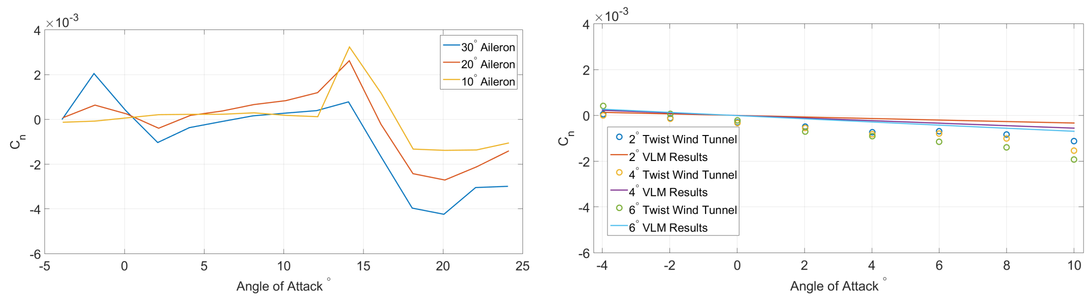

(a) Rigid model (b) Flexible model

Figure 4.20: Yaw characteristics at varying A) aileron angle (for rigid model) and B) wing tip twist angle (for flexible model and simulation model), as a function of angle of attack. (dynamic pressure = 2 psf)

The simulation model was able to correctly predict the direction and trend for both the rolling moments and yawing moments, but it did not match the yawing moment as well as it did with the rolling moment. This is to be expected because without a tail or rudder the differential of the wing drag will be the largest contributing factor to yaw. Because VLM only calculates the lift-induced drag and excludes other sources of drag, such as the profile drag, which change with the varying angle of attack, it is expected that the slope of the simulated yawing moment coefficient curve would be lower than that for the wind-tunnel yawing moment coefficient. There is also a small negative offset in the experimental results about the simulation results. VLM only accounts for the lift-induced drag. Hence the simulation results always pass through (0,0) where the induced drag is zero. It was assumed that the offset is due to asymmetries in the installation of the flexible model or even the model itself, resulting in left-to-right differences in parasitic drag. If this were the case then

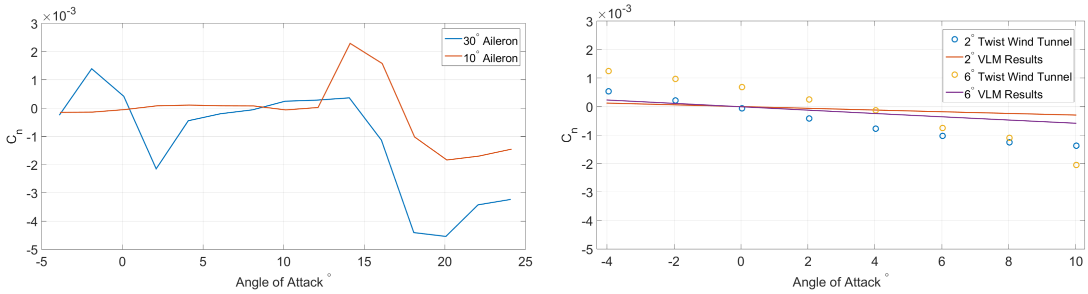

(a) Rigid model

(b) Flexible model

Figure 4.21: Yaw characteristics at varying A) aileron angle (for rigid model) and B) wing tip twist angle (for flexible model and simulation model), as a function of angle of attack. (dynamic pressure = 3 psf)

the zero-crossing point would shift with changes in the airspeed, which occurs when the dynamic pressure changes. Figures 4.21 and 4.22 show the zero-crossing points shifting with the dynamic pressure, indicating that it is likely the result of a parasitic drag difference.

4.4.1.3 Parasitic Drag Inspection

One theoretical advantage of an active twist system is the potential drag reduction, but we saw in these experiments that the traditional model had lower magnitudes of drag. This was even the case for the flat configurations where there was no twist or flaps which suggest that the difference between the two is the parasitic drag. The

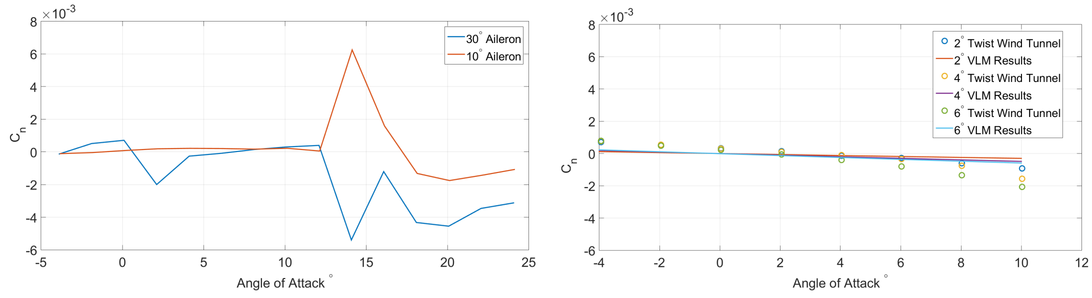

(a) Rigid model

(b) Flexible model

Figure 4.22: Yaw characteristics at varying A) aileron angle (for rigid model) and B) wing tip twist angle (for flexible model and simulation model), as a function of angle of attack. (dynamic pressure = 4 psf)

parasitic drag was estimated the point where there is no lift.

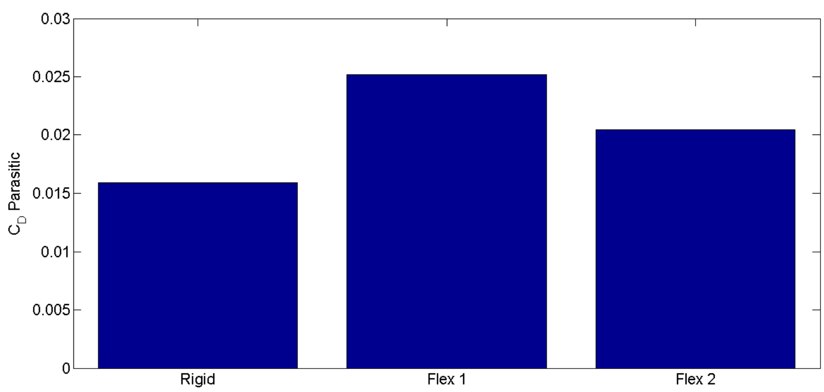

Figure 4.23: Average of parasitic drag for flat configuration of three models

It can be seen from Figure 4.23 that the rigid model had a much lower parasitic drag coefficient than either of the flexible models, but the Flex 2 model has less parasitic drag than the Flex 1 model. The two flex models are identical in the form of their construction and geometry the primary difference was that the Flex 2 model had all of the reversible joints and attachment points glued. This did not seem to have and visual difference, but it appears it had a quantifiable difference in force response. During testing, it was clear that the Kapton strips used for the skin on the flexible models would flutter and likely resulted in ventilation. It seems likely that the skin selection is a large contributing factor in the increase of the parasitic drag.

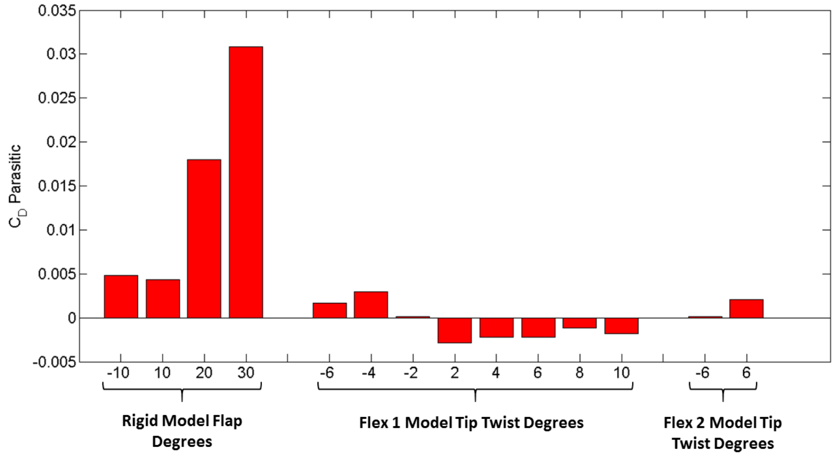

Figure 4.24: Comparisons of the difference between the flat parasitic drag and the twisted tips or angled flaps

It is likely that the skin friction has a dominate effect in the difference between the flat parasitic drag; however, when the flap is actuated, or the tip is twisted, there is a change in the form friction. This can be estimated by assuming that the skin friction is nearly the same for each configuration and looking at the difference in the parasitic drag. Figure 4.24 shows the difference in the parasitic drag for the flaps and active twist. Overall the difference in parasitic drag is small for the active twist configurations, indeed, when we compare the two most similar configurations, the 6 Tip Twist and 10 Flap that the magnitude of change for the flex models are nearly half that for the flaps.

4.4.2 Dynamic Wind Tunnel Results

One of the more under-explored aspects of active twist is the aerodynamic capabilities of active twist. In the earlier section of the symmetric static twist one of the reasons that the 6^o tip twist drag increases at a faster rate with respect to α than the comparable 10^o rigid flap is that as a control surface active twist has a much larger wetted surface area than the flap which means that it has more substantial form drag but will hit stall latter. While from a static perspective the increased wetted surface area can be negative at increasing angles of attack there is potential to use the increased surface area as a means to enhance aerodynamic control parameters. In this section, we will investigate the capabilities of a symmetric active twist as a means of aeroelastic control and validate the modeling technique presented in Section 3.

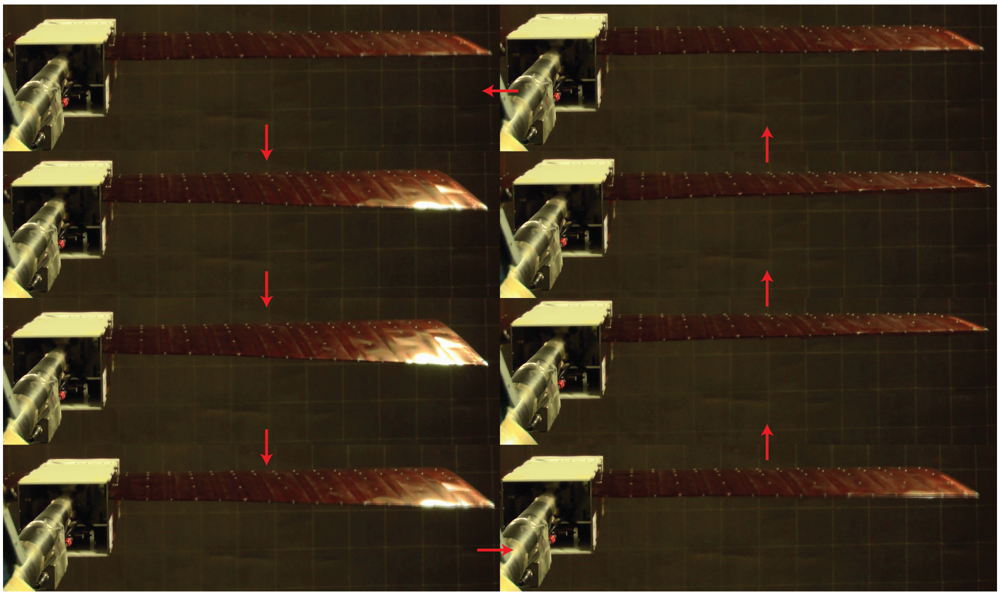

Figure 4.25: Time lapse of the right wing during dynamic twist experiments

The wind tunnel testing had the tip twist oscillating in a sine pattern at a given frequency between 6^o and -6^o tip twist and had the dynamic pressure linearly increasing from $1psf$ to $7psf$. Figure 4.25 shows a timelapse of the right wing during the dynamic wind tunnel testing. To demonstrate the capabilities of the symmetric twist sine wave, we will analyze a case study oscillating at $4Hz$. The simulations were performed using the same parameter shown in Table 4.2. Figure 4.26 indicates that the shape of the aeroelastic simulation matches the wind tunnel results well. The gap shown between top section of the waveform and the bottom part of the waveform is the aeroelastic contributions. While the C_L waveform matches well Figure 4.27 shows that

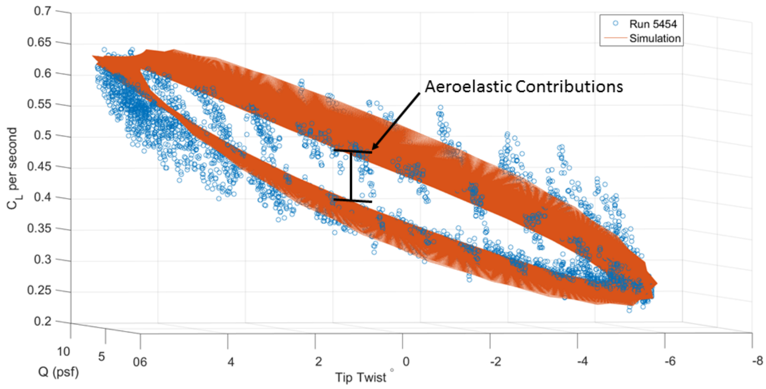

Figure 4.26: The shape of the simulation matches well with the over all shape of the wind tunnel results. The gap between the top and the bottom is the aeroelastic contributions of the dynamic twist showing the ability to control C_L with the twist rate as well as the tip twist.

the drag coefficient does not match very well. The wind tunnel results are much more dispersed, and the aeroelastic simulation seems to be representing the floor of the wind tunnel data instead of matching its shape. Of particular interest is the lift to drag ratio because it acts as an efficient evaluation of aerodynamic efficiency.

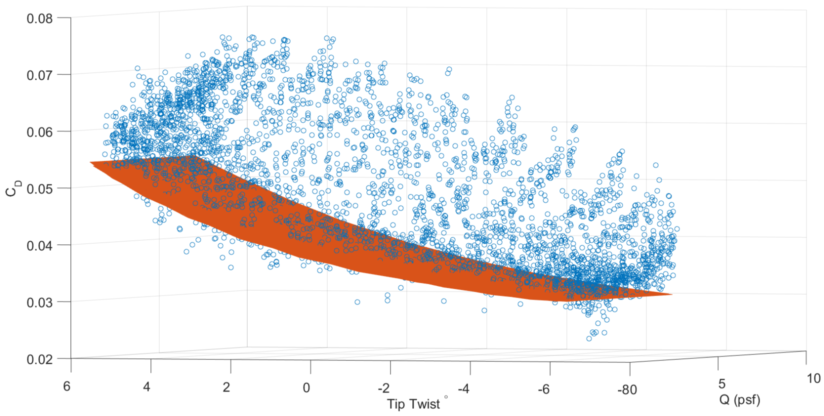

Figure 4.27: The simulations results do not match the drag coefficient as well and instead seem to act more as a floor.

Figure 4.28 shows the lift-drag ratio for the wind tunnel testing and the aeroelastic simulation. The overall shape of the simulation is a decent representation of the form of the wind tunnel data, but it suffers from the same loss in magnitude that the drag coefficient exhibits.

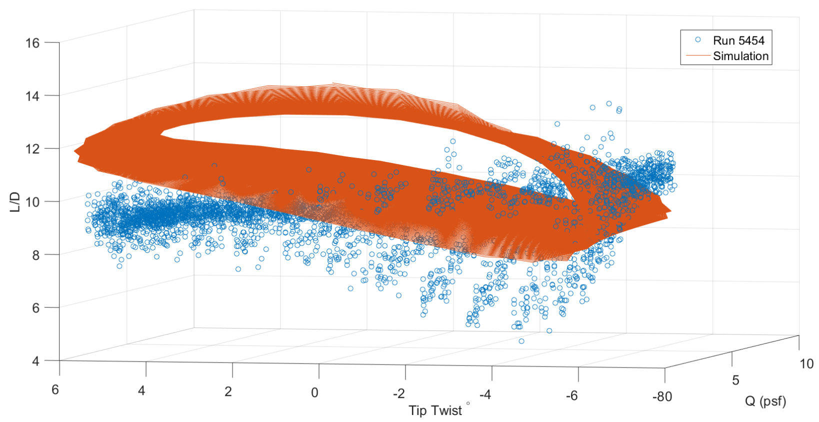

Figure 4.28: The simulations results do not match the drag coefficient as well and instead seem to act more as a floor.

It is possible that the errors displayed in Figures 4.26 to 4.28 are the result of static errors from the bulky fuselage and the small aspect ratio (3) of the aircraft. To investigate the effect of the dynamic, active twist the time derivative for the parameters mentioned above was taken. Figure 4.29 shows that the aeroelastic contributions are proportionally much larger for $\frac{dC_L}{dt}$ than they were for C_L in Figure 4.26 and the simulation replicates the wind tunnel data.

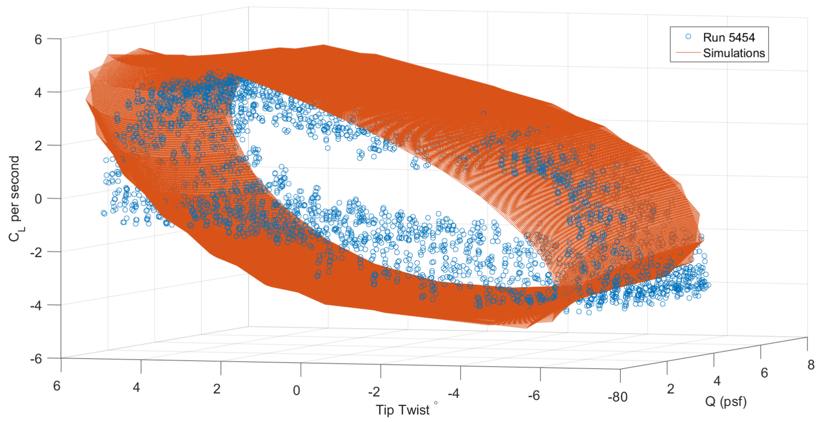

Figure 4.29: The shape of the simulation continues to matches well with the over all shape of the wind tunnel results. The aeroelastic contributions are much more dominant for the lift coefficient rate.

While the most significant qualitative difference between Figures 4.26 and 4.29 is that shape is rounder, and the aeroelastic contributions are more pounced the time derivative of the drag coefficient shows a dramatic increase in the accuracy of the simulation. Figure 4.30 indicates that the simulation matched much better to the shape of the wind tunnel results, with the small exception of the lower right corner around negative six degrees. This suggests that much of the error shown in Figure 4.27 is the result of static errors and that the rate of change of the drag coefficient is dominated by the induced drag.

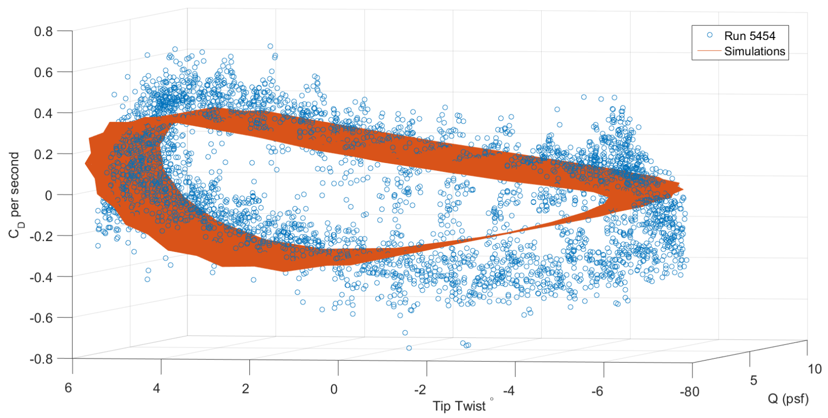

Figure 4.30: The shape of the simulation matches well with the over all shape of the wind tunnel results, suggesting that the rate of change of the drag coefficient is largely due to induced drag

The rate of change of the lift-drag ratio in Figure 4.31 shows good matching with the wind tunnel results as well.

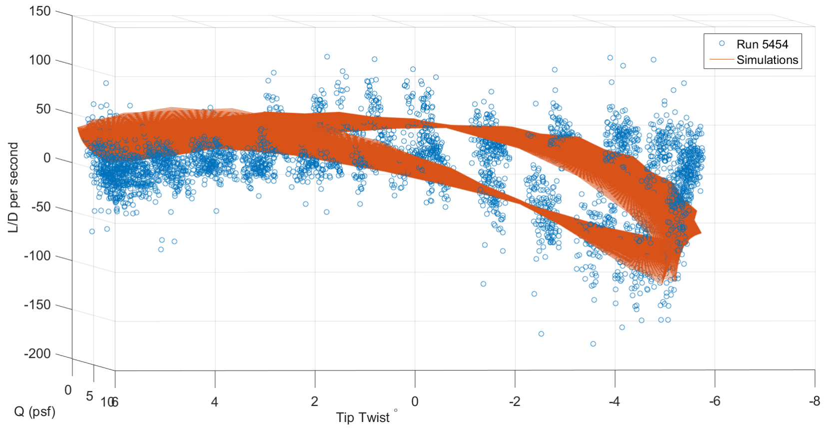

Figure 4.31: As a result of the drag rate being able to be matched by the simulation the lift drag ratio rate is matched well by the simulation as well.

This is important because if we were to ignore the desired lift traveling along the path that allowed the rate of change of the lift-drag ratio always to be positive would result in an increase in the lift-drag ratios in time, the range of particular interest for this frequency and arbitrary lift would be the region between 6^o and 4^o tip twist. While it is not realistic to ignore the lift requirements of the aircraft this concept is an important one that will be explored more later in this thesis.

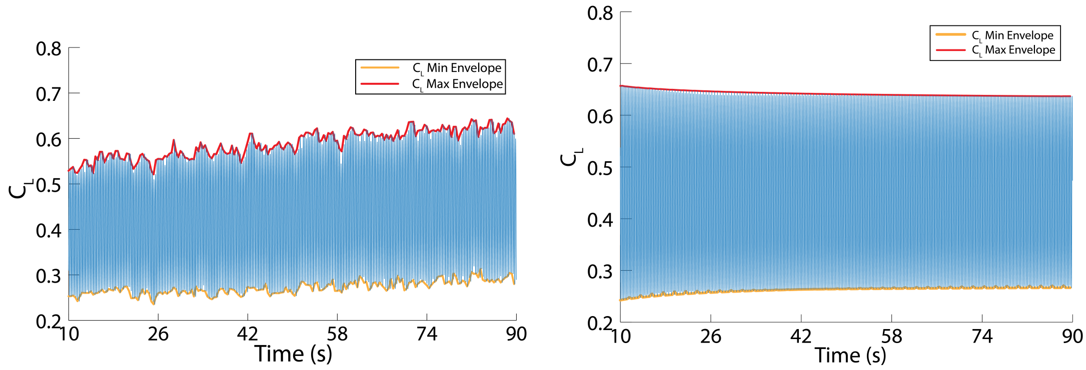

(a) Wind Tunnel Envelope

(b) Aeroelastic Simulations Envelope

Figure 4.32: C_L envelope for the wind tunnel results and the aeroelastic simulations

Now that we have a qualitative idea of the effect of the dynamic twist we need to develop a quantitative means of comparing the simulations to the wind tunnel data. To do this, we will use the maximum and minimum envelope values as shown in Figure 4.32 for the lift coefficients and Figure 4.33 for the drag coefficients.

Figure 4.34 shows the combined percent error of the maximum and minimum envelopes for the lift and drag coefficients. The percent error was calculated for each envelope (maximum and minimum) separately and then added together to get the cumulative envelope error. The drag coefficient error is shown in Figure 4.34 is approaching the maximum expected accuracy for drag given the vortex lattice method. The simulation method takes into account lift-induced drag and then a bulk estimate of skin

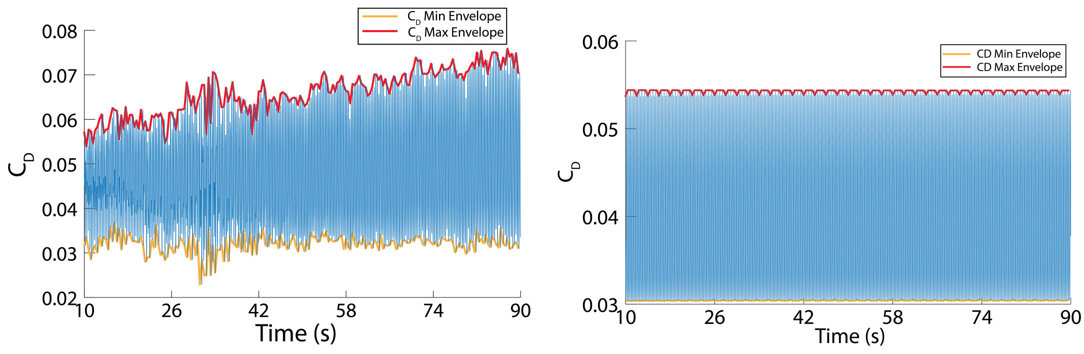

(a) Wind Tunnel Envelope (b) Aeroelastic Simulations Envelope

Figure 4.33: C_D envelope for the wind tunnel results and the aeroelastic simulations

friction which [76] states accounts for about 85% of drag. There is also no clear trend line for the drag coefficient, but the lift coefficient does show a downward trend of error in time. This also corresponds to the decreasing of reduced frequency into the quasi-static range. A single test run is not sufficient to make any lasting judgments on the impact of reduced frequency on the overall accuracy.

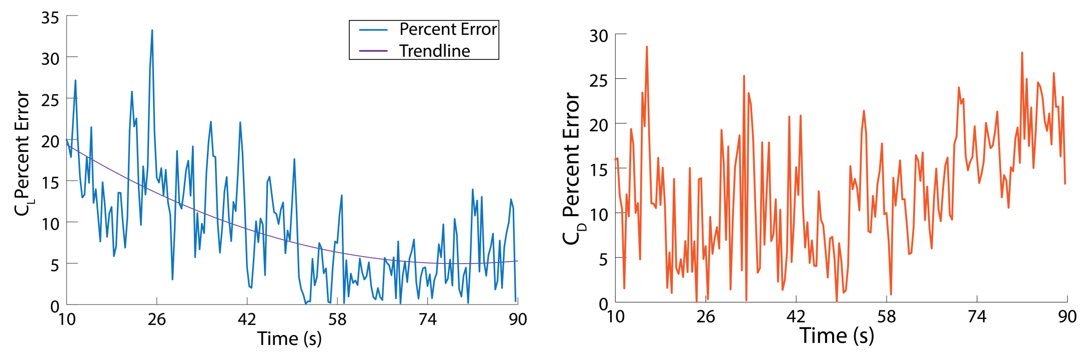

(a) Wind Tunnel Envelope (b) Flexible model

Figure 4.34: Lift and drag percent error for the maximum and minimum envelopes of the test run oscillating at $4Hz$ and an angle of attack of 6^o

Figure 4.35 shows the reduced frequency against the lift coefficient's percent error against. The colored dots are the time domain percent error, the black line if the least squares best fit while the pink section is the 95% confidence interval, the blue part is the expected operation range for the aircraft. While the maximum error value for the operational area might appear alarming at first, it is important to keep in context that 45% of the data points were had less than 15% error in the operational range and a majority of the values that did not come from a single test run. Similar

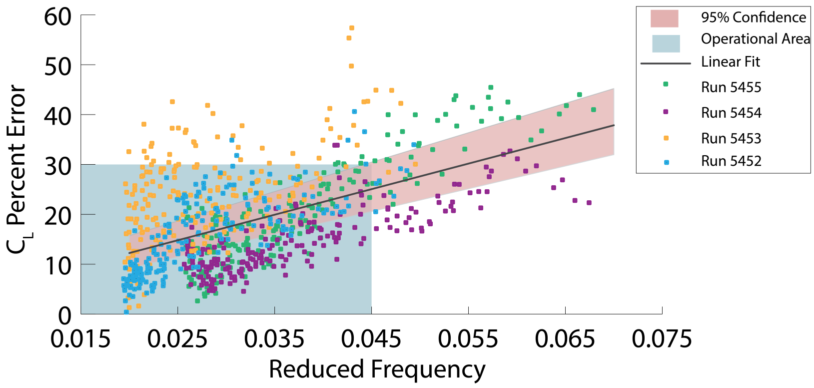

Figure 4.35: The accuracy of the simulation scales with the reduced frequency

methods such as the one [41] used, which was a full vortex ring method and that they compared to results from [20] which used a rigid NACA 0012 spanning the whole wind tunnel to approximate an infinite wing that pitched and plunged and a constant rate while the airspeed was kept constant. Long *et. al* got errors of four to eight percent for a similar range of testing but with a much more idealized configuration our range is easily twice that, but the majority of the values are below the fit line because of the hefty punishment levied by the time domain outliers which would have been less evident in Halfman's configuration because he measured the simple amplitude without the complications of increasing airspeed. At the time of wind tunnel testing, it was decided to do the testing by sweeping the airspeed due to time constraints and a desire to explore the aeroelastic coupling at the largest amount of airspeed values.

Table 4.3: Wind Tunnel and Simulation System ID

Parameter	Wind Tunnel Estimate	Simulation Estimate	Percent Error	Range Overlap
C_{L_θ}	0.0257	0.03	16.6%	True
$C_{L_{\dot\theta}}$	$-3.16e^{-5}$	$-4.97e^{-4}$	147%	True
C_{D_θ}	$2.39e^{-3}$	0.0016	32.9%	True
$C_{D_{\dot\theta}}$	$3.38e^{-6}$	$-9.79e^{-7}$	129%	True
$\frac{dC_{L_\theta}}{dt}$	$5.65e^{-5}$	0.0174	208%	False
$\frac{dC_{L_{\dot\theta}}}{dt}$	0.027	0.0308	14.1%	True
$\frac{dC_{D_\theta}}{dt}$	$-7.68e^{-5}$	$-3.82e^{-3}$	$4.87e^{3}$%	False
$\frac{dC_{D_{\dot\theta}}}{dt}$	$2.1e^{-3}$	$1.59e^{-3}$	24.3%	False

The ultimate goal of this simulation tool is to be able to be used as a design tool to understand trends and capabilities in a computationally efficient manner and to be able to estimate the control derivatives. To validate this linear step-wise regression was performed using NASA's System IDentification Programs for AirCraft (SIDPAC) [27] on both the wind tunnel data and the simulated data. The results are shown in

Table 4.3 for the most parts the estimated parameters for the simulations matched well with the wind tunnel estimates. For the control derivatives associated with lift and drag coefficients, the only ones that showed significant errors were very small values that are nearly zero and the 95% confidence interval ranges for the values overlap meaning that there is still a possibility that the simulations value could be a representative of the wind tunnel value. The rate control derivatives have some larger errors on the nonprimary control derivatives (tip twist as opposed to twisting rate) which seems likely to be a result of errors from the simple finite derivatives taken to achieve those values.

4.4.2.1 Stall Mitigation

The lift data of Figure 4.12 presents an intriguing possibility to use active twist for stall mitigation at a given angle of attack. For example, at a tip twist of 10o and an angle of attack of 10^o, the flexible model has begun to stall; however, while maintaining the angle of attack, the twist could be reduced (e.g., to 4 o or below) to avoid stall. A brief experiment was run to show that stall mitigation was possible, and the results compared favorably to the trends shown in Figure 4.12.

To test the active twist capability of stall mitigation, we started at given angle of attack and a tip twist of 10^o. Twist was then reduced by 2^o and maintained at the new value for ten seconds. Figure 16 shows the results of the stall mitigation tests compared to the expected values. We can see that for all the angles of attack other than 14^o, we were able to mitigate the stall effects by varying the twist. In fact, in these cases, we were able to observe stall-induced trailing edge flutter of the wing skin,

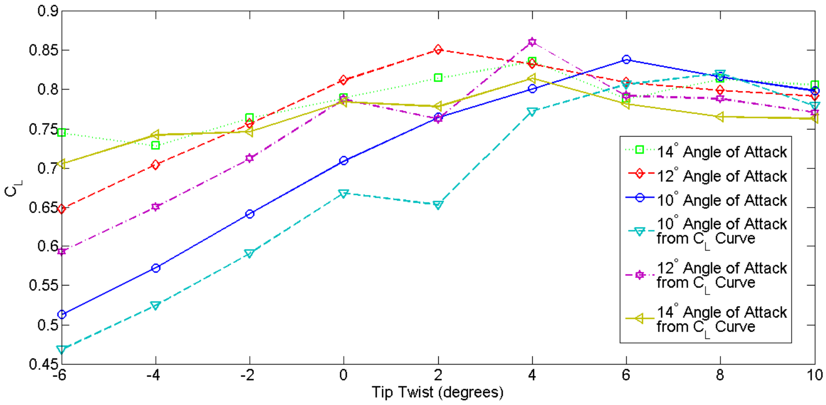

Figure 4.36: Comparisons of the test for stall mitigation at various angles of attack and their expected values from Figure 4.12

and the trailing edge flutter for the 10^o angle of attack visually stopped at 6^o of twist, confirming what the data indicate in Figure 4.36. It is also interesting to note that the lift coefficients from the stall mitigation tests were consistently 0.5 higher than the expected values. Of course, more runs would be needed to show that changing twist to alleviate stall would result in a higher lift coefficient, but it is interesting nonetheless.

Chapter 5

Control

The control of morphing aircraft has been a critical limiting factor in the adoption of this technology. Much like the simulation methodology, it is necessary to develop the structural control aspects of the aeroelastic control before moving to the fully coupled system. To address these issues, I start by trying to develop controllers that take advantage of the underlying configuration of the structure.

5.1 Structural Decentralized Control

One of the primary issues when developing structural control is the sheer dimensionality that is associated with a large (and even not that large) lattice based structures. One of the primary advantages of using the lattice-based approach is that each voxel can be individually characterized and considered a physical "finite element" [7]. Therefore, the behavior of the entire wing structure could be predicted by assembling the required series of elementary voxels.

As a practical example of the proposed approach, we will consider a single long array of octahedron voxels anchored to a rigid base representing a minimalistic wing attached to the plane's fuselage. Figure 5.1 shows an example of a single interconnected array of voxel substructures. The proposed model consists of two types of voxels: *active voxels* (with control authority), which could perform as an active functional component with actuation capability, and *passive voxels* (without control authority). The goal of active voxels is to suppress the external disturbances, and therefore, improve the overall performance of the structure. It should be noted that for easy manipulation, the active and passive voxels have identical connectors and require identical assembly techniques.

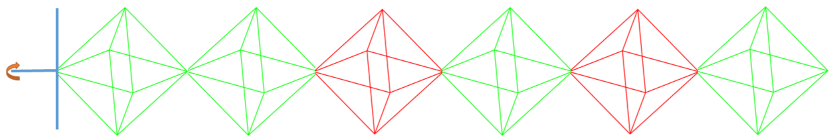

Figure 5.1: A single long array of cuboctahedron voxels. Red indicates an active voxels and green a passive one.

The voxels that we are proposing to use as the basis for the wing structure have already been created and tested.[25] We will use the primary bending modes of the voxels as a means of creating a low order model. This low order model then allows us to create a large scale model of the proposed wing structure. For very large scale structures even with a low order model, like the one we are proposing, the problem can quickly become intractable. Dimensionality issues are a primary motivation for the creation of decentralized control[4], this and the inherent structure of the lattice make it an excellent choice for decentralized control.

5.1.1 Low Order Modeling of a Cuboct Voxel

To obtain a low-order spring-mass-damper model of a voxel substructure, we performed a lab-based dynamics and vibration test. The voxel was rigidly attached to a vibration isolating optical table and loaded at the top. The modal response of the voxel during unloading was monitored using a Polytech Laser Vibrometer, which was mounted on the same vibration isolation optical table to minimize outside interference. The laser was focused on the mounting nodes for measurement. Figure 5.2 shows the experimental setup on the left and the voxel on the right. Figure 5.3 schematically shows the loading/unloading approach.

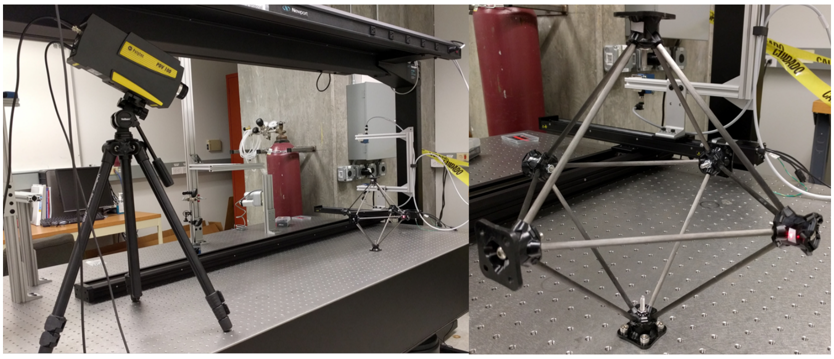

Figure 5.2: Experimental setup (left) and a single voxol clamped on teh optical table (right)

Figure 5.4 shows the frequency domain of the voxel, measured at the five nodes connecting the carbon fiber struts. The first harmonic mode (see insert in Figure 5.4) corresponds to the first bending mode of the voxel. Equation 5.1 predicts the quality

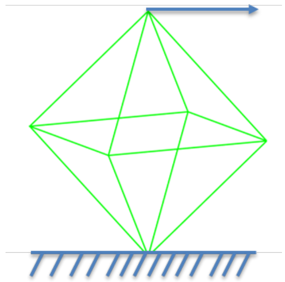

Figure 5.3: Schematic representation of the experimental procedure.

factor using the maximum frequency and the full width at half maximum.

$$Q = \frac{f_{max}}{\Delta f} \tag{5.1}$$

The quality factor can be related to the damping of the system through,

$$c = 4\sqrt{kM}Q\,. \tag{5.2}$$

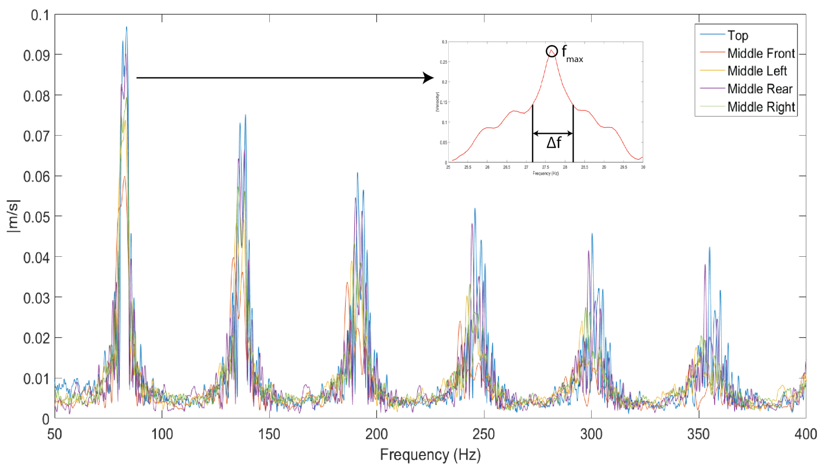

Figure 5.4: Frequency domain of the cuboctahedron voxel, measured at the five nodes connecting the carbon fiber struts. The lowest harmonic order is used to find the quality factor.

The mass of the voxel $M = 1.01$ kg is used to predict the appropriate spring constant k associated with the primary bending mode, and it is given by

$$k = f_{max}^2 M = 771.7\,\mathrm{N}/m \tag{5.3}$$

which results in a damping of $c = 97.41\frac{N}{ms}$. It is also of interest that as the frequency increases the peaks continue to spread out and diverge into multiple individual peaks, which is evidence of the variations between beams and that the interface between the beams plays a substantial role in the behavior of the structure at the higher modes.

The equations of motion for the assembled wing structure is obtained using the low order spring-mass-damper voxel models, as follows,

$$\mathcal{M}\ddot{\eta}(t) + \mathcal{C}\dot{\eta}(t) + \mathcal{K}\eta(t) = \mathcal{B}u(t) + \mathcal{D}w(t) \tag{5.4}$$

where $\eta(t)$, $\dot{\eta}(t)$, and $\ddot{\eta}(t)$ denote respectively the displacement, velocity and accelration of the voxels, $u(t)$ represents the active voxels whose locations are indicated in $\mathcal{B}$, $w(t)$ denotes the disturbance inputs, with intensity $W > 0$, applied to the voxel structure. It is assumed that there is a total of n voxels, among them m active voxels. The structural matrices $(\mathcal{M}, \mathcal{C}, \mathcal{K})$ have dimensions $n \times n$ and can be defined as

$$\begin{bmatrix} m & 0 & 0 & 0 & \dots & 0 \\ 0 & m & 0 & 0 & \dots & 0 \\ 0 & 0 & m & 0 & \dots & 0 \\ \vdots & \vdots & \vdots & \vdots & \ddots & \vdots \\ 0 & 0 & 0 & 0 & \dots & m \end{bmatrix}, \begin{bmatrix} 2c & -c & 0 & 0 & \dots & 0 \\ -c & 2c & -c & 0 & \dots & 0 \\ 0 & -c & 2c & -c & \dots & 0 \\ \vdots & \vdots & \vdots & \vdots & \ddots & \vdots \\ 0 & 0 & 0 & 0 & \dots & c \end{bmatrix}, \begin{bmatrix} 2k & -k & 0 & 0 & \dots & 0 \\ -k & 2k & -k & 0 & \dots & 0 \\ 0 & -k & 2k & -k & \dots & 0 \\ \vdots & \vdots & \vdots & \vdots & \ddots & \vdots \\ 0 & 0 & 0 & 0 & \dots & k \end{bmatrix}. \tag{5.5}$$

Then, Equation (5.4) can be rewritten in the state-space representation as follows,

$$\dot{x}(t) = Ax(t) + Bu(t) + Dw(t) \tag{5.6}$$

where $x = [\eta^t \;\; \dot{\eta}^t]^t$ denotes the states, and

$$A = \begin{bmatrix} 0 & I \\ -\mathcal{M}^{-1}\mathcal{K} & -\mathcal{M}^{-1}\mathcal{C} \end{bmatrix}, \; B = \begin{bmatrix} 0 \\ \mathcal{M}^{-1}\mathcal{B} \end{bmatrix}, \; D = \begin{bmatrix} 0 \\ \mathcal{M}^{-1}\mathcal{D} \end{bmatrix}. \tag{5.7}$$

We assume the actuator dynamics can be described by

$$\dot{u}_i(t) = a_i u_i(t) + b_i v_i(t) \,, \quad i = 1, 2, \ldots, m \,, \tag{5.8}$$

where (a_i, b_i) are known, $[v_1 \; v_2 \; \cdots \; v_m]^t = v$ are the commanded inputs, and $[u_1 \; u_2 \; \cdots \; u_m]^t = u$. Then, (5.8) can be expressed in a compact matrix form as

$$\dot{u}(t) = A_u u(t) + B_u v(t) \,, \tag{5.9}$$

where A_u and B_u are diagonal matrices with entries a_i and b_i, respectively. In this study, we consider that each control input u_i is bounded by its practical limitation. Hence, the proposed decentralized control is to design a novel bounded input controller to suppress the excessive structural vibration for (5.6).

5.1.2 Decentralized Model Formulation

To generate the decentralized control formulation we will follow the procedure for Type II overlapping control presented by *Zečević*[86] and *Šiljak*[68], and extend it to include the actuator dynamics. To start, we first combine (5.6) and (5.9) to form an augmented system as follows,

$$\Sigma : \quad \dot{\bar{x}}(t) = \bar{A}\bar{x}(t) + \bar{B}v(t) + \bar{D}w(t) \tag{5.10}$$

where the combined state vector $\bar{x} = [x^t \;\; u^t]^t$, and the system matrices are given by

$$\bar{A} = \begin{bmatrix} A & B \\ 0 & A_u \end{bmatrix}, \; \bar{B} = \begin{bmatrix} 0 \\ B_u \end{bmatrix}, \; \bar{D} = \begin{bmatrix} D \\ 0 \end{bmatrix}.$$

Next, depending on where the active voxels are being placed, we need to reorder the sequence of combined state vector $\bar{x}$ into,

e.g., $[\eta_1^t \; \dot{\eta}_1^t \; u_1 \; \eta_2^t \; \dot{\eta}_2^t \; u_2 \; \ldots \eta_m^t \; \dot{\eta}_m^t \; u_m \; \eta_{m+1}^t \; \dot{\eta}_{m+1}^t \ldots]^t$. Subsequently, all thirsty matrices, i.e. matrices in bar, $(\bar{A}, \bar{B}, \bar{D})$ need to be adjusted accordingly. Finally, by following the procedure presented in [86, 68], the matrices $(\bar{A}, \bar{B}, \bar{D})$ can be transformed into an overlapping description $(\hat{A}, \hat{B}, \hat{D})$ as follows,

$$\hat{A} = \left[\begin{array}{cc|cc|cc|c} A_{11} & A_{12} & 0 & 0 & 0 & \ldots & 0 \\ A_{21} & A_{22} & 0 & A_{23} & 0 & \cdots & 0 \\ \hline A_{21} & 0 & A_{22} & A_{23} & 0 & \cdots & 0 \\ 0 & 0 & A_{32} & A_{33} & 0 & A_{34} & \cdots \\ \hline 0 & 0 & A_{32} & 0 & A_{33} & A_{34} & \cdots \\ \vdots & \vdots & \vdots & \vdots & \vdots & \vdots & \ddots \end{array}\right], \; \hat{B} = \left[\begin{array}{c|c|c|c} 0 & 0 & \cdots & 0 \\ b_1 & 0 & \cdots & 0 \\ \hline 0 & 0 & \cdots & 0 \\ 0 & b_2 & \cdots & 0 \\ \hline 0 & 0 & \cdots & 0 \\ \vdots & \vdots & \vdots & \vdots \end{array}\right]$$

$$, \; \hat{D} = \left[\begin{array}{c|c|c|c} D_1 & 0 & \cdots & 0 \\ 0 & 0 & \cdots & 0 \\ \hline 0 & D_2 & \cdots & 0 \\ 0 & 0 & \cdots & 0 \\ \hline 0 & 0 & \cdots & 0 \\ \vdots & \vdots & \vdots & \vdots \end{array}\right]. \tag{5.11}$$

It should be noted that these matrices meet the requirements set in $\check{S}iljak$ [68] as shown below,

$$V\bar{A} = \hat{A}V \ , \ \ V\bar{B} = \hat{B} \ , \ \ V\bar{D} = \hat{D} \, , \tag{5.12}$$

where

$$V = \begin{bmatrix} I_1 & 0 & 0 & \cdots & 0 \\ 0 & I_2 & 0 & \cdots & 0 \\ 0 & I_2 & 0 & \cdots & 0 \\ 0 & 0 & I_3 & \cdots & 0 \\ \vdots & \vdots & \vdots & \ddots & \vdots \\ 0 & 0 & 0 & 0 & I_n \end{bmatrix} . \tag{5.13}$$

In compact form, the resulting new state-space equation with overlapping states can be described by

$$\hat{\Sigma} : \ \ \dot{\hat{x}}(t) = \hat{A}\hat{x}(t) + \hat{B}v(t) + \hat{D}w(t) \, . \tag{5.14}$$

For large structures, the number of states causes the problem to be intractable making it necessary to not only create a problem formulation that will result in a controller that can be implemented in a decentralized manner, but to solve the LMI in a decentralized manner. To achieve this, we will formulate the decentralized control problem by focusing on the diagonal subblocks of $\hat{A}$ in (5.11).

5.1.3 LMI-based Constrained Input-Output Optimization Problem

In this section, the input and output constrained optimization problem for the wing in the framework of decentralized control is formulated. It should first be noted that input constraints in (5.6) are in fact converted into state constraints in (5.14), which can then be shown to be equivalent to output constraints by introducing those states as part of control outputs. Consider the following decentralized models derived from (5.14),

$$\hat{\Sigma}_i \ : \ \begin{cases} \dot{\hat{x}}_i(t) = \hat{A}_i \hat{x}_i(t) + \hat{B}_i v_i(t) + \hat{D}_i w(t) \\ y_i(t) = \hat{H}_i x_i(t) \, , \quad i = 1, 2, \ldots, m \end{cases} \tag{5.15}$$

where $\hat{\Sigma}_i$ is the ith substructure that is controlled by an active voxel v_i located at $\hat{B}_i$. In addition, y_i denotes the control outputs, which can be used to monitor both the local structural responses and the control input u_i. Furthermore, the system matrices are given by

$$\hat{A}_i = \begin{bmatrix} A_{i,i} & A_{i,i+1} \\ A_{i+1,i} & A_{i+1,i+1} \end{bmatrix} , \ \hat{B}_i = \begin{bmatrix} 0 \\ b_i \end{bmatrix} , \ \hat{D}_i = \begin{bmatrix} D_i \\ 0 \end{bmatrix} , \ \hat{H}_i = \begin{bmatrix} H_i & 0 \\ 0 & 1 \end{bmatrix} .$$

Note that H_i indicates interested structural response locations at $\hat{\Sigma}_i$, and "1" in $\hat{H}_i$ corresponds to where u_i is located. One critical aspect of decentralized control for large systems is the diagonal dominance of $\hat{\Sigma}$, which makes the control design much tractable since it only involves designing for a subsystem of smaller dimension, such as $\hat{\Sigma}_i$.

It should be noted that, in $\hat{\Sigma}_i$, constraints on the control inputs u_i are converted into the constraints on output y_i, and the allowable control authority is known apriori. Moreover, since the overall control design objective is to suppress the motion as much as possible, it is practical to pre-set an acceptable or desirable level of structural vibration as design criteria. Now, we can formulate the output covariance constrained optimization problem, which can then be solved as a standard $\mathcal{H}_2$ performance problem [87]. Also, the existence of such solution can be determined by checking if a feasible solution exists to a coupled linear matrix inequalities (LMIs) [74]. Therefore, the numerically efficient LMI-based convex optimization tools and algorithms can be applied for control design analysis and synthesis. The following theorem contains the main result.

Theorem 1: *Consider the system $\hat{\Sigma}$ described in (5.14). Suppose $\bar{Y} > 0$ and $\bar{U} > 0$ are known. The output covariance constrained optimization problem is solvable, if there exist matrices G_i and positive definite symmetric matrices Z_i, $i = 1, 2, \ldots, m$, that minimize the output covariance performance cost*

$$\min_{G,Z} \quad trace\,(\, H_i Z_i H_i^t \,)\,, \quad i = 1, 2, \ldots, m\,, \tag{5.16}$$

subject to

$$\begin{bmatrix} \hat{A}_i Z_i + Z_i \hat{A}_i^t + G_i^t \hat{B}_i^t + \hat{B}_i G_i & \hat{D}_i W^{\frac{1}{2}} \\ \star & -I \end{bmatrix} < 0\,, \quad i = 1, 2, \ldots, m\,, \tag{5.17}$$

$$\begin{aligned} \bar{Y} - \begin{bmatrix} H_i & 0 \end{bmatrix} Z_i \begin{bmatrix} H_i \\ 0 \end{bmatrix} \geq 0\,, \quad i = 1, 2, \ldots, m\,, \\ \bar{U} - \begin{bmatrix} 0 & 1 \end{bmatrix} Z_i \begin{bmatrix} 0 \\ 1 \end{bmatrix} \geq 0\,, \quad i = 1, 2, \ldots, m\,. \end{aligned} \tag{5.18}$$

If a feasible solution exists to the above LMIs, then the full state feedback control law is given by

$$v(t) = \hat{K}\hat{x} \tag{5.19}$$

where $\hat{K}$ is of the form

$$\hat{K} = \begin{bmatrix} K_{11} & K_{12} & 0 & \\ 0 & K_{22} & K_{23} & \\ & & & \ddots \end{bmatrix} \tag{5.20}$$

and

$$\begin{bmatrix} K_{i,i} & K_{i,i+1} \end{bmatrix} = G_i Z_i^{-1} \,. \tag{5.21}$$

Proof: The proof combines results from *Zečević*[86] for decentralized modeling and control architecture, and *Swei et al.* [74] for output covariance constrained optimization.

5.1.4 Proposed Structure Configuration and Simulation Setup

One of the proposed applications for active twist technology mentioned in Section 5.1.4 are HALE aircraft. For HALE's it is critically important to have large lifting surfaces to allow for low flight speeds in high altitudes. With that in mind, I propose a 200 voxel long array that will simulate a half wingspan. Each voxel strut is 0.2m long, hence resulting in a voxel length of about 0.283m, which results in a wing half span of approximately 57m which is of comparable wingspan as the HALE proposed by [18]. Assuming a wing thickness of 12% the proposed aircraft would have a cord length of 2.36m which is about the cord length of NASA's Helios Prototype. [11]

An important part of the formulation of the decentralized structural control model is the selection of the actuation/sensor locations and the partitioning of the full model into smaller section. For simplicity of the models, the actuation points were selected to be evenly distributed through the whole structure, for example, if there were 20 active voxels, then there would be ten voxels between each active voxel. The boundaries between each active voxel are chosen to be exactly half way between as is shown in Figure 5.5.

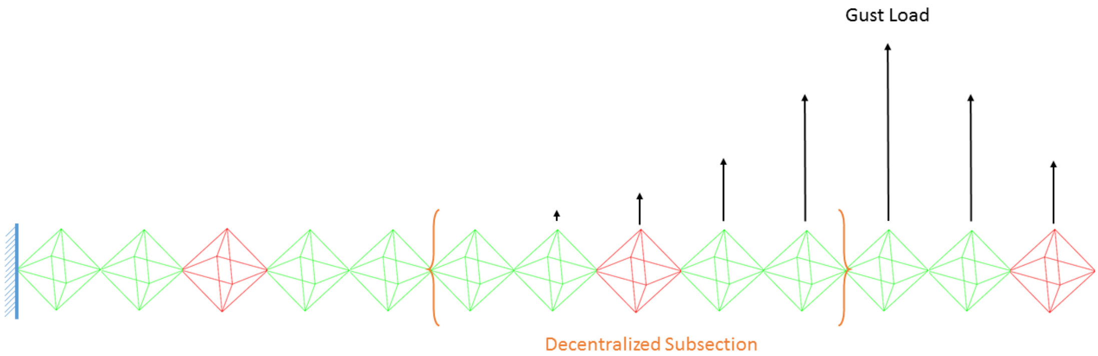

Figure 5.5: Example of the equally spaced active voxels and the split up of the decentralized control sections

The simulation is set up to have the wing be rigidly attached to the base forming a cantilevered beam where a representative gust load it applied. It is assumed that the wing is in a statically deformed configuration and that the gust will take the form of a variation in wind speed. The gust shape is a normal distribution centered $40m$ from the wing root with a maximum value of $2.3\frac{m}{s}$ and a standard deviation of $10m$. It is assumed that the gust is a normal distribution in the time domain and is centered at $2s$ with a standard deviation of $1s$. The variation in wind speed is translated to loading by assuming the aircraft is at cruise conditions and calculating that the lift coefficient would need to be .270 to maintain altitude considering only the weight of the voxels. Assuming just the weight of the voxels is not a perfect assumption but it does allow for and an estimate of the lifting coefficient.

5.1.5 Simulation Results

The decentralized controllers were simulated with the structure proposed in Section 5.1.4 with 25, 40, and 50 active voxels. We used the approach suggested by SeDuMi and YALMIP [40] to solve the LMIs presented in Section 5.1.3. The same weighting matrices were used for all of the simulations to try and make them as comparable as possible. This can be done without fear of stability issues because the off-diagonal components for each model are identical therefore the selected Q that meets the stability requirement for a single case applies to all of them. The simulations were run for 200 seconds using MATLAB's ODE45 solver with commanded time steps of 100ms.

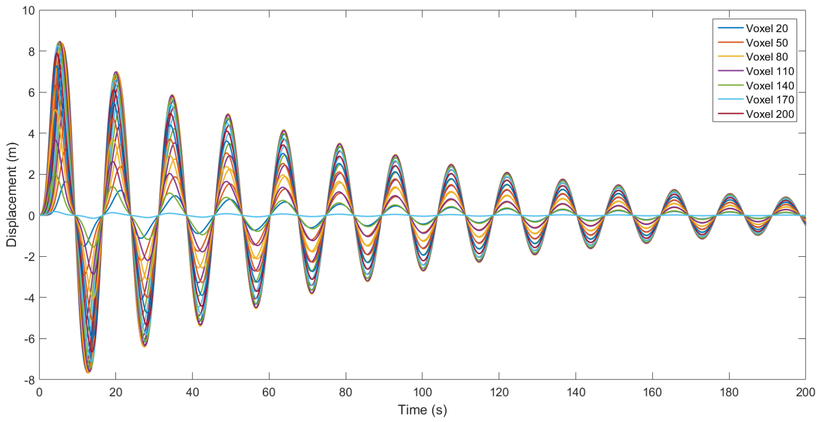

Figure 5.6: The uncontrolled position provides a reference for how much the voxels oscillate.

From Figure 5.6 it can be seen that the disturbance excites the wing causing a primary mode to be dominant though at least early in the simulation the voxels at the tip have a time delay compared to the ones towards the root. At the same time Figure, 5.7 shows the velocity of the uncontrolled simulation and demonstrates the secondary modes that are evident in the tipward voxels.

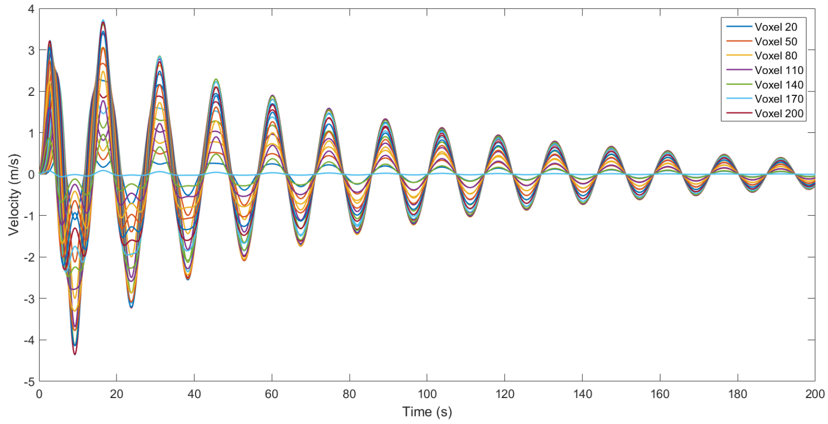

Figure 5.7: The uncontrolled velocity shows that the waveforms on the outer half of the wingspan behave differently with a larger secondary mode shape than the wing root half of the wing.

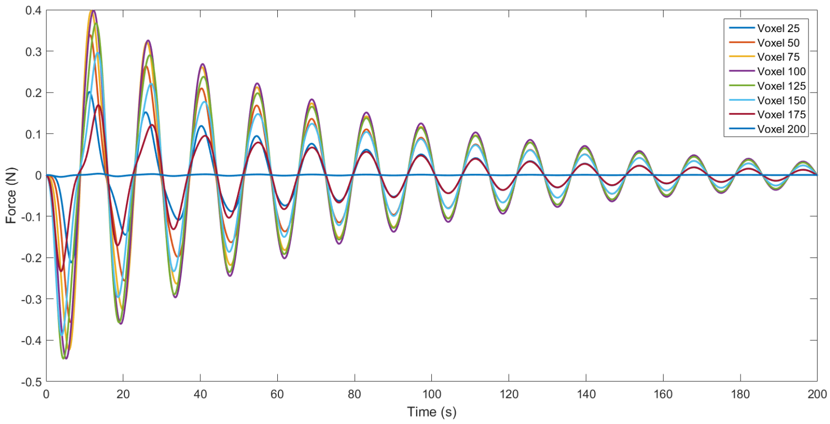

Figure 5.8: The control forces are larger towards the center of the wing. The control forces towards the tip are delayed in the time domain compared to the ones toward the root.

As a reference, a 40 active voxel case study of the controlled simulation control forces is shown. Figure 5.8 indicates that the force profile follows the waveform of the voxel position heavily. Much like the position values the control forces act differently depending on if they are closer to the tip or the root. It should be noted that the magnitude of the forces applied is very small because the controllers are focused on only aiding the wing in removing energy over time. Figure 5.9 shows the comparison of the voxel with the largest displacement for all the of configurations studied here. The 50 active voxel configuration shows an increase in the frequency and the most significant reduction in the magnitude of the voxel displacement.

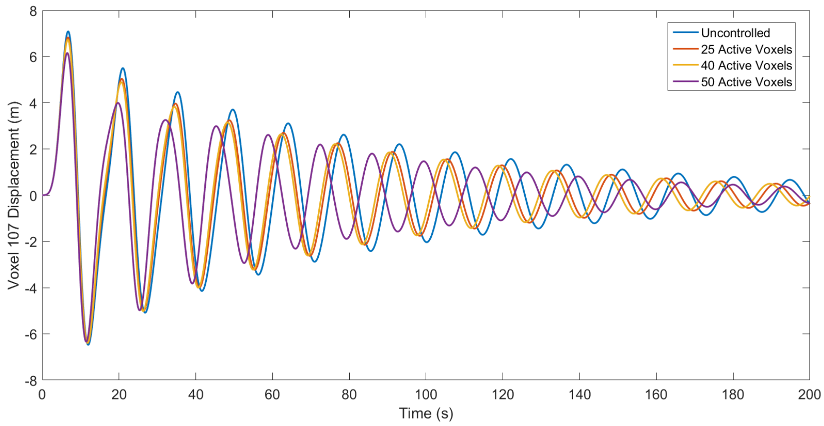

Figure 5.9: Comparision of the maximum displaced voxel for each number of active voxels

From Table 5.1 we can see that all of the controllers do a good job of limiting vibrations and removing energy from the system. As would be expected the more active voxels that are added to the system the more energy is removed from the system. The relationship is not a linear one though the addition of 15 voxels to go to 40 from 25 active voxels only removed an additional $5.5e^3 Js$ of energy while the additional ten voxels from 40 to 50 active voxels resulted in a reduction of $30.4Js$. This is also shown in Table 5.1 with the energy removed per voxel column where the largest amount of energy removed per voxel is the 25 active voxel configuration followed by the 50 active voxel configuration. This suggests that there is a significant influence from the configuration as well as the number of active voxels.

Table 5.1: Controller Performance Metrics

Number of Active Voxels	Total Energy (Js)	Mean Energy (Js)	Control Force (Ns)	Energy Removed per Voxel (J)
0	$319.7e^3$	159.77	-	-
25	$277.2e^3$	138.5	$3.61e^3$	1.7
40	$271.7e^3$	135.8	$5.131e^3$	1.2
50	$241.3e^3$	120.6	$13.99e^3$	1.57

5.2 Decentralize Transfer Matrix Method Control

As was mentioned in Section 5.1.2 one of the primary issues with the lattice based structures is the dimensionality. One approach is the one we took in Section 5.1.2 where the key is transforming the preexisting model into a more manageable sized component another is to create an control centered model to do this the extended discrete-time transfer matrix method (E-DT-TMM) is proposed to model and analyze large dynamical aerostructures. The basic idea behind this approach was inspired by the work of Tan *et al.* [75], where the notion of modified transfer matrix method (M-TMM) approach was developed in continuous-time, based mainly on the dynamic stiffness matrix of a finite element [9], where the elemental mass and stiffness matrices are symmetric and positive semi-definite. By applying recursively the elemental transfer method that relates two adjacent elements, a reduced order model can be obtained. The primary goal there was to reduce the computational efforts involved in structural analysis and controls for flexible space structures. In addition to incorporating the notion of M-TMM, we also utilize the numerical integration approach, known as the discrete-time transfer matrix method (DT-TMM), proposed by Kumar and Sankar [35], in which a series of mass-spring-damper models were used. The focus there was on developing numerically tractable algorithms to perform structural analysis.

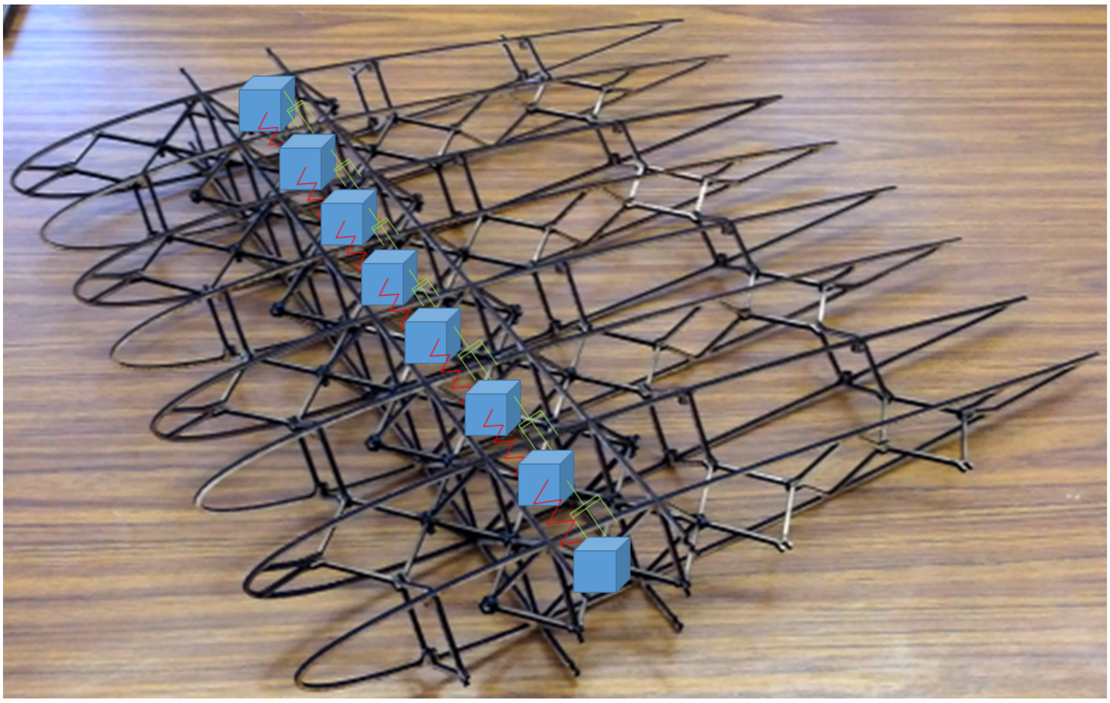

Figure 5.10: Lattice-based composite cellular wing structure and its lumped mass model.

The proposed E-DT-TMM is an integration of approaches mentioned above through which a computationally efficient and lower order model can be attained. This framework is especially appealing to aeronautics applications, where the aeroelastic coupling effects would result in sign-indefinite and un-symmetrical pertinent structural matrices (mass, stiffness, and damping). Hence, the proposed E-DT-TMM forms the foundation for modeling of the lattice-based aerostructures.

Some previous research have used the DT-TMM as a means of controlling the flexible robots [31, 32] and the multi-body systems [62, 63, 21]. Krauss [32], Krauss and Okasha [31], and Hendy *et al.* [21] used the computational efficiency of the transfer matrix method for system identification and controller tuning for full order model. These works had shown that the transfer matrix method could be used to design an efficient controller, however, to the author's knowledge no research publication so far has addressed the use of discrete-time transfer matrix method for model reduction and designing decentralized structural controls.

5.2.1 A Discrete-Time Reduced-Order Model

Figure 5.10 shows a section of aircraft wing built by utilizing the lattice-based cellular structure concept. The composition of this discrete construction renders itself naturally to lumped-mass system setup. Each rib of the wing provides a logical location for a lumped mass, and the connecting components between each airfoil can be modeled as spring and damper. In this section, we introduce the concept of E-DT-TMM and apply it to attain the reduced-order structural model that is best suited for control synthesis. Specifically, we model the half-span wing section connected to the fuselage as a clamp-free structure.

Before proceeding, we provide a brief overview of DT-TMM concept developed by Kumar and Sankar [35].

5.2.2 Overview of DT-TMM

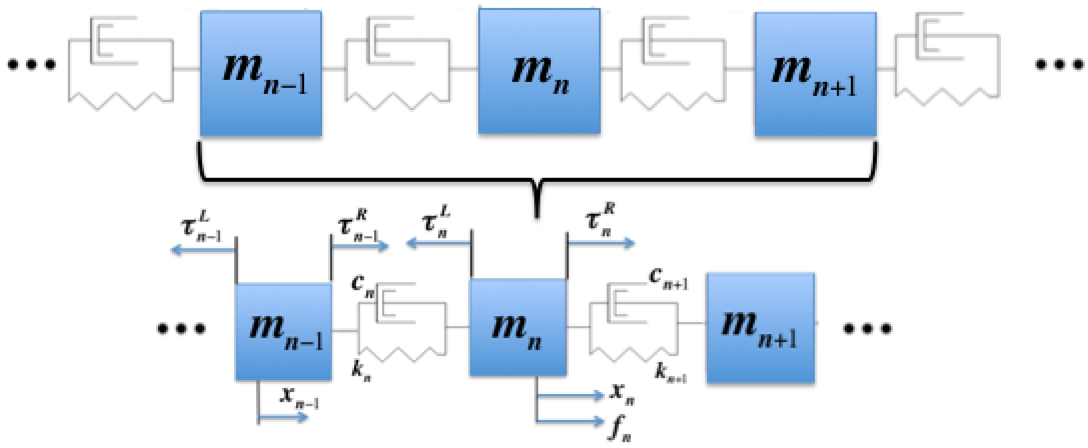

Figure 5.11: A lumped-mass model with free-body diagram for mass m_n.

Figure 5.11 shows a sequence of lumped masses which are interconnected by stiffness and damping components modeled by spring and damper. The discrete-time equation of motion for a given subsystem n centered at mass m_n at time step t_i can be described by [35]

$$m_n \ddot{x}_n(t_i) = \tau_n^R(t_i) - \tau_n^L(t_i) + f_n(t_i) \tag{5.22}$$

where $\ddot{x}_n$ denotes the acceleration of mass m_n, τ_n^R and τ_n^L the forces from right and left side of mass m_n, and f_n the control force applied to mass m_n. Furthermore,

τ_n^L can be derived from the free-body diagram in Figure 5.11 and is described by

$$\tau_n^L = k_n \left[x_n(t_i) - x_{n-1}(t_i)\right] + c_n \left[\dot{x}_n(t_i) - \dot{x}_{n-1}(t_i)\right] \tag{5.23}$$

where x_n and $\dot{x}_n$ denote the displacement and velocity of mass m_n, and (k_n, c_n) denotes the pair of stiffness and damping components at the left side of m_n. Because of symmetricity and repetitiveness of the construction, the internal forces between two adjacent masses are the same, that is

$$\tau_n^L = \tau_{n-1}^R \, . \tag{5.24}$$

The generalized form of acceleration and velocity can be represented numerically as

$$\ddot{x}_n(t_i) = A_n(t_i)x_n(t_i) + B_n(t_i) \tag{5.25a}$$

$$\dot{x}_n(t_i) = D_n(t_i)x_n(t_i) + E_n(t_i) \tag{5.25b}$$

where the format of (A_n, B_n, D_n, E_n) depends on the chosen numerical integration scheme. Now, substituting (5.24) and (5.25) into (5.22) yields

$$m_n \left[A_n x_n + B_n\right] = \tau_n^R - \tau_n^L + f_n \tag{5.26}$$

where

$$\tau_n^L = k_n(x_n - x_{n-1}) + c_n \left[(D_n x_n + E_n) - (D_{n-1}x_{n-1} + E_{n-1})\right] \, . \tag{5.27}$$

Note that, for simplicity, we have dropped the functional dependency on current time step t_i. Since $x_n^R = x_n^L$, we can rewrite (5.26) in the matrix representation as

$$\begin{Bmatrix} x \\ \tau \\ 1 \end{Bmatrix}_n^R = \begin{bmatrix} 1 & 0 & 0 \\ m_n A_n & 1 & m_n B_n - f_n \\ 0 & 0 & 1 \end{bmatrix} \begin{Bmatrix} x \\ \tau \\ 1 \end{Bmatrix}_n^L , \tag{5.28}$$

which can be described in a compact form as

$$v_n^R = P_n v_n^L , \tag{5.29}$$

where v_n denotes the "state vector" at subsystem n or at mass m_n. Note that (5.27) can be rewritten as follows,

$$x_n = \frac{1}{k_n + c_n D_n} \left[\tau_n^L + (k_n + c_n D_{n-1}) x_{n-1} - c_n (E_n - E_{n-1}) \right] , \tag{5.30}$$

and together with (5.24), results in

$$\begin{Bmatrix} x \\ \tau \\ 1 \end{Bmatrix}_n^L = \begin{bmatrix} \frac{k_n + c_n D_{n-1}}{k_n + c_n D_n} & \frac{1}{k_n + c_n D_n} & \frac{-c_n (E_n - E_{n-1})}{k_n + c_n D_n} \\ 0 & 1 & 0 \\ 0 & 0 & 1 \end{bmatrix} \begin{Bmatrix} x \\ \tau \\ 1 \end{Bmatrix}_{n-1}^R , \tag{5.31}$$

or can be equivalently written as

$$v_n^L = F_n v_{n-1}^R . \tag{5.32}$$

It should be noted that Eqs. (5.29) and (5.32) can be combined to propagate the state vector "v" spatially forward from left to right, all at time step t_i.

5.2.3 Introduction to E-DT-TMM

The purpose of DT-TMM [35] was to facilitate the numerical analysis for lumped mass structures. Hence the notion of state propagation only needed to apply in one direction, from left to right. However, we can formulate the propagation from right to left by following the similar process as described in Section 5.2.2. This recursive state propagation from either direction is the essence of E-DT-TMM.

To formulate the propagation from right to left, we first rewrite (5.28) as

$$\begin{Bmatrix} x \\ \tau \\ 1 \end{Bmatrix}_n^L = \begin{bmatrix} 1 & 0 & 0 \\ -m_n A_n & 1 & -m_n B_n + f_n \\ 0 & 0 & 1 \end{bmatrix} \begin{Bmatrix} x \\ \tau \\ 1 \end{Bmatrix}_n^R , \tag{5.33}$$

or equivalently as

$$v_n^L = J_n v_n^R . \tag{5.34}$$

As illustrated in Figure 5.11 and Eq. (5.27), we can derive τ_{n+1}^L as

$$\begin{cases} \tau_{n+1}^L = \tau_n^R \\ \tau_{n+1}^L = k_{n+1}(x_{n+1} - x_n) + c_{n+1}\left[(D_{n+1}x_{n+1} + E_{n+1}) - (D_n x_n + E_n)\right] \end{cases}$$

Similarly, we can represent the above in matrix representation as

$$\begin{Bmatrix} x \\ \tau \\ 1 \end{Bmatrix}_n^R = \begin{bmatrix} \frac{k_{n+1}+c_{n+1}D_{n+1}}{k_{n+1}+c_{n+1}D_n} & \frac{-1}{k_{n+1}+c_{n+1}D_n} & \frac{-c_{n+1}(E_n-E_{n+1})}{k_{n+1}+c_{n+1}D_n} \\ 0 & 1 & 0 \\ 0 & 0 & 1 \end{bmatrix} \begin{Bmatrix} x \\ \tau \\ 1 \end{Bmatrix}_{n+1}^L , \tag{5.35}$$

or can be equivalently described as

$$v_n^R = H_{n+1} v_{n+1}^L , \tag{5.36}$$

which is to propagate the state vector "v" from right to left.

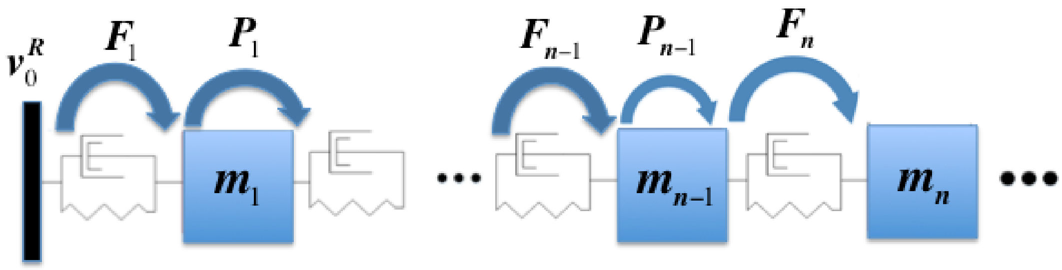

Figure 5.12: Transfer matrix propagation from left end to mass m_n.

5.2.3.1 Matrix formulation from left end to mass m_n

In this section, we work to develop a relationship between the left edge boundary conditions and the states at mass m_n, as depicted in Figure 5.12. We start by combining (5.29) and (5.32) to render

$$v_n^L = F_n P_{n-1} v_{n-1}^L \,, \tag{5.37}$$

and we can continue this process until we reach to the left edge, hence we obtain

$$v_n^L = F_n Q_{n-1} v_0^R \,, \tag{5.38}$$

where

$$Q_{n-1} = \prod_{i=1}^{n-1} P_i F_i \,; \; Q_0 = 1 \,, \tag{5.39}$$

and Q_{n-1} denotes the transfer function matrix relating the left edge boundary conditions v_0^R to subsystem m_{n-1}, and $F_n Q_{n-1}$ relating v_0^R to subsystem m_n.

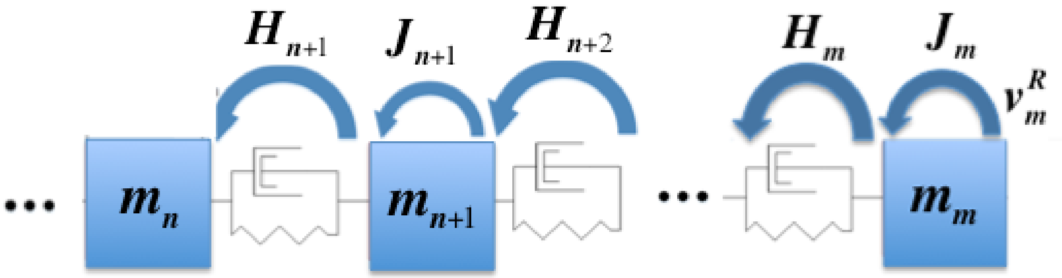

Figure 5.13: Transfer matrix propagation from right end to mass m_n.

5.2.3.2 Matrix formulation from right end to mass m_n

We have shown the states propagation from left to right and arrived at subsystem n. In this section, we establish the relationship between the right edge m_m and the subsystem n by propagating from right to left; see Figure 5.13. Combining Eqs. (5.34) and (5.36) we obtain

$$v_n^R = H_{n+1} J_{n+1} v_{n+1}^R \,, \tag{5.40}$$

and this process can continue and eventually results in

$$v_n^R = T_{n+1} v_m^R \,, \tag{5.41}$$

where v_m^R is the right edge boundary conditions, and

$$T_{n+1} = \prod_{i=m}^{n+1} H_i J_i \,, \tag{5.42}$$

which represents the transfer function matrix relating the right edge subsystem m to subsystem n.

5.2.3.3 Combining left and right propagation

The proposed transfer matrix propagation approach described earlier can be applied recursively, and by combining the process shown in Sections 5.2.3.1 and 5.2.3.2 yields

$$\begin{cases} v_n^L = F_n Q_{n-1} v_0^R \\ v_n^R = T_{n+1} v_m^R \\ m_n \left[A_n x_n + B_n \right] = \tau_n^R - \tau_n^L + f_n \end{cases} \tag{5.43}$$

The first equation relates the propagation from the left side of mass m_n, the second equation from the right side, and then the last equation relates both ends of m_n. Given the boundary conditions at both edges, the state vectors v_n^R and v_n^L at subsystem n and at time step t_i can be solved from (5.43), which apparently is a reduced-order system. The state vectors at other subsystems at time t_i can be derived recursively by propagating v_n^R and v_n^L as the right and left boundary conditions in Eqs. (5.37) and (5.40), respectively, as illustrated in Figure 5.14. The velocity and acceleration at mass m_n can then be calculated using (5.25). To move forward in time, the same procedure can be repeated for time step t_{i+1}.

However, in situations where either the chosen sampling time step is too small or the number of subsystems is too large; depending on the numerical integration scheme used which typically is proportional to the inverse of time step squared, the matrices Q_{n-1} and T_{n+1} can be excessively large. As a result, a significant numerical error can be observed. To overcome this numerical issue, we propose to further decompose the first two equations in (5.43).

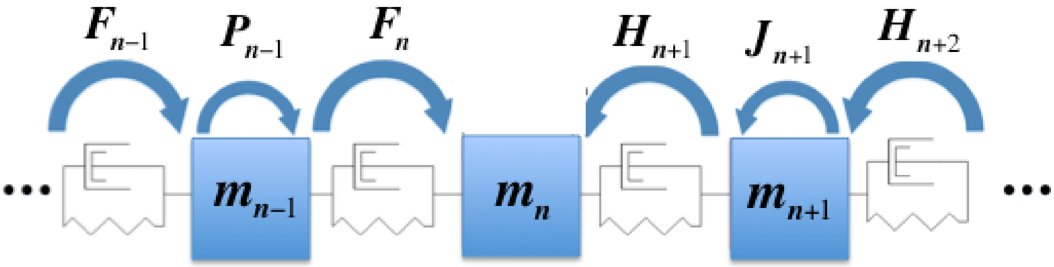

Figure 5.14: Combination of left and right propagation to mass m_n.

Let the mass m_p be any subsystem p which is between n and the left edge clamped boundary. Then, we can follow Section 5.2.3.1 to formulate a Q_p matrix that relates the clamped boundary to subsystem p as

$$v_p^R = Q_p v_0^R \,, \; Q_p = \prod_{i=1}^{p} P_i F_i \,. \tag{5.44}$$

Next, using the approach presented in Section 5.2.3.2 we can generate a matrix G_p that relates v_{n-1}^R to subsystem p as

$$v_p^R = G_p v_{n-1}^R \,, \; G_p = \prod_{i=n-1}^{p} H_i J_i \,. \tag{5.45}$$

Therefore, equating (5.44) and (5.45) renders

$$Q_p v_0^R = G_p v_{n-1}^R \,.$$

Relating v_{n-1}^R to v_n^L by utilizing Eq. (5.36) and substituting that relation into above yields

$$Q_p v_0^R = G_p H_n v_n^L \,. \tag{5.46}$$

Similarly, we choose a mass m_q be any subsystem q in between n and the right edge m. Using the approach presented in Section 5.2.3.1 we can generate a transfer matrix that relates v_m^R to subsystem q as

$$v_q^R = T_{q+1} v_m^R \,,\; T_q = \prod_{i=m}^{q+1} H_i J_i \,, \tag{5.47}$$

and following Eq. (5.29) to formulate a transfer matrix that relates v_{n+1}^L to subsystem q as follows,

$$v_q^R = R_q v_{n+1}^L \,,\; R_q = \left(\prod_{i=n+2}^{q} P_i F_i \right) P_{n+1} \,. \tag{5.48}$$

It follows from (5.47) and (5.48) that

$$T_{q+1} v_m^R = R_q v_{n+1}^L \,,$$

and utilizing (5.32) to relate v_{n+1}^L to v_n^R and substituting this relation into above yields

$$T_{q+1} v_m^R = R_q F_{n+1} v_n^R \,. \tag{5.49}$$

Finally, Eq. (5.43) can be replaced by the following expressions,

$$\begin{cases} Q_p v_0^R = G_p H_n v_n^L \\ T_{q+1} v_m^R = R_q F_{n+1} v_n^R \\ m_n \left[A_n x_n + B_n \right] = \tau_n^R - \tau_n^L + f_n \end{cases} \tag{5.50}$$

The process presented above is to derive a single localized subsystem for mass m_n. The choice of subsystem n usually corresponds to where the control actuation is applied. In case there are multiple control inputs, we may derive a localized subsystem for each control input by following the same propagation method to attain a reduced-order representation, as shown in (5.50).

5.2.4 Decentralized Control Problem Formulation

In this section, we develop a control-centric reduced-order dynamic model based on the E-DT-TMM approach presented in Section 5.2.3.3. We consider the clamp-free lumped-mass system subject to a single control input applied to mass m_n. To this end, we can explicitly express Eq. (5.50) as follows,

$$\begin{bmatrix} Q_{11} & Q_{12} & Q_{13} \\ Q_{21} & Q_{22} & Q_{23} \\ 0 & 0 & 1 \end{bmatrix} \begin{bmatrix} 0 \\ \tau_0 \\ 1 \end{bmatrix} = \begin{bmatrix} G_{11} & G_{12} & G_{13} \\ G_{21} & G_{22} & G_{23} \\ 0 & 0 & 1 \end{bmatrix} \begin{bmatrix} H_{11}^n & H_{12}^n & H_c^n(E_{n-1} - E_n) \\ 0 & 1 & 0 \\ 0 & 0 & 1 \end{bmatrix} \begin{bmatrix} x_n \\ \tau_n^L \\ 1 \end{bmatrix}$$

$$\begin{bmatrix} T_{11} & T_{12} & T_{13} \\ T_{21} & T_{22} & T_{23} \\ 0 & 0 & 1 \end{bmatrix} \begin{bmatrix} x_m \\ 0 \\ 1 \end{bmatrix} = \begin{bmatrix} R_{11} & R_{12} & R_{13} \\ R_{21} & R_{22} & R_{23} \\ 0 & 0 & 1 \end{bmatrix} \begin{bmatrix} F_{11}^{n+1} & F_{12}^{n+1} & F_c^n(E_n - E_{n+1}) \\ 0 & 1 & 0 \\ 0 & 0 & 1 \end{bmatrix} \begin{bmatrix} x_n \\ \tau_n^R \\ 1 \end{bmatrix}$$

$$m_n \left[A_n x_n + B_n\right] = \tau_n^R - \tau_n^L + f_n \tag{5.51}$$

As mentioned, by decomposing the propagation as above we are able to avoid some numerical issues and the problem becomes more tractable. In solving (5.51), we are able to attain a system representation that is based solely on the current subsystem and the adjacent subsystems, as shown below

$$C_{x_n} x_n = C_{E_{n-1}} E_{n-1} + C_{E_n} E_n + C_{E_{n+1}} E_{n+1} + C_R + C_L - m_n B_n + f_n \,, \tag{5.52}$$

where all the coefficients are defined in Appendix A. It is important to note that $Q_{i,i}$, $T_{i,i}$, and $G_{i,i}$ in (5.51) contain information on the configuration of the spring, mass, and damper systems that were present between subsystem n and the boundary conditions. The configuration of C_{x_n} and C_{E_n} also change depending on the boundary conditions. This allows the decentralized subsystem n to act as if it is directly connected to the boundary conditions through a series of combined mass, spring, damper systems.

Kumar and Sankar [35] provided a comprehensive list of numerical integration schemes, including Fox-Euler, Newmark β, and Houbolt methods. In this paper, we make use of the Houbolt integration method because its framework can be readily incorporated into formulating the discrete-time control problem. The Houbolt integration coefficients are given by [35],

$$\begin{cases} A_n(\Delta Tk) = \frac{2}{\Delta T^2} \\ B_n(\Delta Tk) = -\frac{1}{\Delta T^2}[5x(\Delta Tk) - 4x(\Delta T(k-1)) + x(\Delta T(k-2))] \\ D_n(\Delta Tk) = \frac{11}{6\Delta T} \\ E_n(\Delta Tk) = -\frac{1}{6\Delta T}[18x(\Delta Tk) - 9x(\Delta T(k-1)) + 2x(\Delta T(k-2))] \end{cases} \tag{5.53}$$

where ΔT denotes the sampling time and $k = 1, 2, \ldots$. It is important to note that the Houbolt integration method is only valid after 3 time steps have passed. Kumar and Sankar provided an extended set of coefficients for the earlier time steps, but they are not particularly important from the controls point of view and thus ignored here.

Substituting (5.53) into (5.52) results in a discrete-time model which has smaller dimension, as shown below

$$
\begin{bmatrix} x_n(\Delta T(k+1)) \\ x_n(\Delta Tk) \\ x_n(\Delta T(k-1)) \end{bmatrix} =
$$

$$
\begin{bmatrix} \frac{1}{C_{x_n}}(\frac{-3C_{E_n}}{\Delta T} + \frac{5m_n}{\Delta T^2}) & \frac{1}{C_{x_n}}(\frac{3C_{E_n}}{2\Delta T} + \frac{-4m_n}{\Delta T^2}) & \frac{1}{C_{x_n}}(\frac{-C_{E_n}}{3\Delta T} + \frac{m_n}{\Delta T^2}) \\ 1 & 0 & 0 \\ 0 & 1 & 0 \end{bmatrix} \begin{bmatrix} x_n(\Delta Tk) \\ x_n(\Delta T(k-1)) \\ x_n(\Delta T(k-2)) \end{bmatrix} \tag{5.54}
$$

$$
+\frac{1}{C_{x_n}}(C_{E_{n-1}}E_{n-1} + C_{E_{n+1}}E_{n+1} + C_R + C_L + f_n)
$$

which can be equivalently rewritten as

$$
X_n(k+1) = \mathcal{A}_{nn}X_n(k) + \mathcal{B}_n(\alpha(k) + f_n(k))\,, \tag{5.55}
$$

where $X_n(k) = [x_n(\Delta Tk),\, x_n(\Delta T(k-1)),\, x_n(\Delta T(k-2))]^T$, the system matrices $(\mathcal{A}_{nn}, \mathcal{B}_n)$ and the exogenous input α are given by

$$
\mathcal{A}_{nn} = \begin{bmatrix} \frac{1}{C_{x_n}}(\frac{-3C_{E_n}}{\Delta T} + \frac{5m_n}{\Delta T^2}) & \frac{1}{C_{x_n}}(\frac{3C_{E_n}}{2\Delta T} + \frac{-4m_n}{\Delta T^2}) & \frac{1}{C_{x_n}}(\frac{C_{E_n}}{3\Delta T} + \frac{m_n}{\Delta T^2}) \\ 1 & 0 & 0 \\ 0 & 1 & 0 \end{bmatrix}, \qquad \mathcal{B}_n = \begin{bmatrix} \frac{1}{C_{x_n}} \\ 0 \\ 0 \end{bmatrix} \tag{5.56}
$$

$$
\alpha = C_{E_{n-1}}E_{n-1} + C_{E_{n+1}}E_{n+1} + C_R + C_L\,. \tag{5.57}
$$

Note that the pair $(\mathcal{A}_{nn}, \mathcal{B}_n)$ is controllable. Equation (5.55) is the equation of motion for the mass m_n, where α consists of the contribution of forces from neighboring masses, and f_n the control input applied at mass m_n. To design a stabilizing decentralized controller, we first note that α is a "weak" coupling between mass m_n and its neighbors, and therefore we can treat (5.55) as a local subsystem [67].

If there are r number of control inputs applied at various lumped-mass positions, then for each control input we would end up a subsystem representation as in (5.55), and by following the same argument as above, we obtain

$$\begin{cases} X_1(k+1) = \mathcal{A}_{11} X_1(k) + \mathcal{B}_1(\alpha_1(k) + f_1(k)) \\ X_2(k+1) = \mathcal{A}_{22} X_2(k) + \mathcal{B}_2(\alpha_2(k) + f_2(k)) \\ \vdots \\ X_r(k+1) = \mathcal{A}_{rr} X_1(k) + \mathcal{B}_r(\alpha_r(k) + f_r(k)) \end{cases} \tag{5.58}$$

where each reduced-order subsystem in (5.58) is driven by a single control input and the pair $(\mathcal{A}_{ii}, \mathcal{B}_i)$, $i = 1, \ldots, r$, is controllable.

5.2.5 Discrete-time decentralized optimal control design

In this paper, we propose a discrete-time linear quadratic regulator (LQR) controller to stabilize the subsystem n described in (5.55) while minimizing the following performance cost function J_n,

$$J_n = \sum_{k=0}^{\infty} \left[X_n^T(k) Q X_n(k) + R f_n^2(k) \right] , \tag{5.59}$$

where Q is a positive definite symmetric weighting matrix for the states, and $R > 0$ a scalar weighting factor for control input. The resulting optimal controller can be obtained as

$$f_n(k) = -K_n X_n(k)\,, \tag{5.60}$$

where K_n is the control gain matrix given by

$$K_n = (R + \mathcal{B}_n^T P_n \mathcal{B}_n)^{-1} \mathcal{B}_n^T P_n \mathcal{A}_{nn}\,, \tag{5.61}$$

and P_n is the unique stabilizing solution to the following algebraic Riccati equation

$$P_n = Q + \mathcal{A}_{nn}^T (P_n - P_n \mathcal{B}_n (R + \mathcal{B}_n^T P_n \mathcal{B}_n)^{-1} \mathcal{B}_n^T P_n) \mathcal{A}_{nn}\,.$$

It should be reminded that, since the Houbolt integration scheme is used in developing the reduced-order subsystem, we need to wait for three time steps before the state $X_n(k)$ is populated initially. In case there are multiple control inputs, as was shown in (5.58), we follow the same LQR controller design process shown above for each reduced-order subsystem and solve the linear equations simultaneously for closed-loop response at any particular subsystem of interest. For instance, in order to compute the closed-loop response at mass m_j, we first need to apply the left and right propagation as presented in Section 5.2.3.3 with respect to each individual subsystem in (5.58) and solve for the individual response at subsystem j. Then, summation of these individual contributions would yield the total response at subsystem j.

5.2.5.1 Stability of decentralized control

An important aspect of utilizing the proposed discrete-time transfer matrix method is the ability to formulate a diagonally dominant system matrix. To illustrate this, we consider the clamped-free lumped-mass system subject to a single control input, where the control is applied at mass m_n. We can apply the E-DT-TMM to generate a discrete-time "full state" representation by explicitly expressing all m subsystems as

$$\begin{bmatrix} X_1(k+1) \\ \vdots \\ X_n(k+1) \\ \vdots \\ X_m(k+1) \end{bmatrix} = \underbrace{\begin{bmatrix} \mathcal{A}_{11} & \mathcal{A}_{12} & \cdots & \mathcal{A}_{1m} & \cdots & \mathcal{A}_{1m} \\ \vdots & \vdots & \cdots & \vdots & \cdots & \vdots \\ \mathcal{A}_{n1} & \mathcal{A}_{n2} & \cdots & \mathcal{A}_{nn} & \cdots & \mathcal{A}_{nm} \\ \vdots & \vdots & \cdots & \vdots & \cdots & \vdots \\ \mathcal{A}_{m1} & \mathcal{A}_{m2} & \cdots & \mathcal{A}_{mn} & \cdots & \mathcal{A}_{mm} \end{bmatrix}}_{\Pi} \begin{bmatrix} X_1(k) \\ \vdots \\ X_n(k) \\ \vdots \\ X_m(k) \end{bmatrix} + \begin{bmatrix} 0 \\ \vdots \\ \mathcal{B}_n \\ \vdots \\ 0 \end{bmatrix} f_n(k) \tag{5.62}$$

where $\mathcal{A}_{ii}$ is defined as

$$\mathcal{A}_{ii} = \begin{bmatrix} \frac{1}{C_{x_i}}(\frac{-3C_{E_i}}{\Delta T} + \frac{5m_i}{\Delta T^2}) & \frac{1}{C_{x_i}}(\frac{3C_{E_i}}{2\Delta T} + \frac{-4m_i}{\Delta T^2}) & \frac{1}{C_{x_i}}(\frac{C_{E_i}}{3\Delta T} + \frac{m_i}{\Delta T^2}) \\ 1 & 0 & 0 \\ 0 & 1 & 0 \end{bmatrix},$$

and when $i \neq j$, $\mathcal{A}_{ij}$ is defined as

$$\mathcal{A}_{ij} = \begin{bmatrix} \frac{1}{C_{x_i}}\left(\frac{-3C_{E_j^i}}{\Delta T}\right) & \frac{1}{C_{x_i}}\left(\frac{3C_{E_j^i}}{2\Delta T}\right) & \frac{1}{C_{x_i}}\left(\frac{C_{E_j^i}}{3\Delta T}\right) \\ 1 & 0 & 0 \\ 0 & 1 & 0 \end{bmatrix},$$

where $C_{E_j^i}$, which is defined in Appendix A, is the constant relating subsystem j to subsystem i. It should be noted that the subsystem n described in (5.55) can be readily readout from (5.62). Furthermore, all the diagonal matrices $\mathcal{A}_{ii}$ are Hurwitz.

To ensure the diagonal dominance in matrix Π, the parameter $C_{E_j^i}$ has to be made sufficiently small, such that $-3C_{E_i} + \frac{5m_i}{\Delta T} >> C_{E_j^i}$. A critical path to make this happen is that the parameters $|F_c^n|$ and $|H_c^n|$ be much less than 1. Note that

$$F_c^n = \frac{-c_{n+1}}{k_{n+1} + c_{n+1}D_n} \ , \ H_c^n = \frac{-c_n}{k_n + c_n D_n} \ ,$$

where $D_n = \frac{11}{6\Delta T}$. If we assume that the stiffness and damping used in the lumped-mass system are all the same, then $F_c^n = H_c^n$. It should be noted that when $k_n << c_n$ or $k_n \approx c_n$, the time step ΔT must be reduced in order for $|F_c^n| << 1$. When $k_n >> c_n$ and $m_n << 1$, the time step must be reduced to ensure that $\frac{m_n}{\Delta T} >> C_{E_j^n}$ for diagonal dominance. Therefore, substituting the LQR controller (5.60) into the subsystem n enhances the stability of the overall system while maintaining the diagonal dominance. Similarly, the same argument can be applied when there are multiple control inputs.

5.2.6 Numerical Simulations

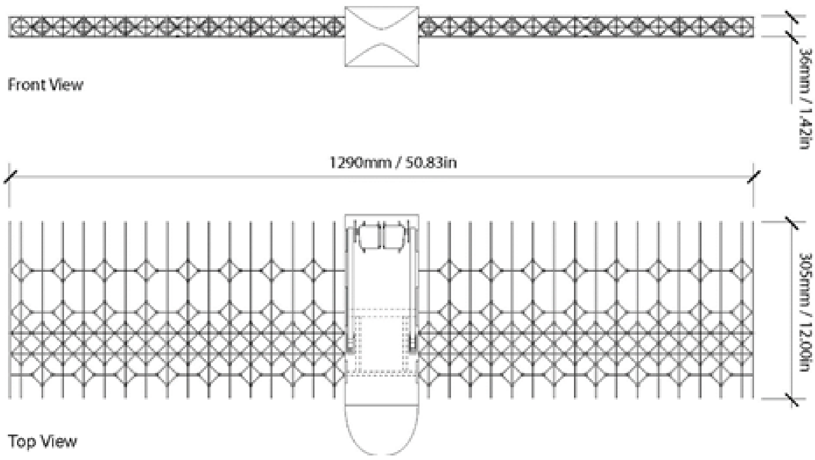

Figure 5.15: Configuration of lattice-based digital wing.

In this section, we show simulation results by comparing the proposed E-DT-TMM based decentralized LQR controller for the reduced-order local subsystem to the

Table 5.2: Parameters for simulated lumped mass system.

Parameter	Value
Number of Masses	16
Mass	$0.00640kg$
Rotational Spring Stiffness	$2810.9398N$
Damping Constant	$1e^{-7}\frac{N}{s}$
Time Step	$500\mu s$

full state continuous-time LQR controller for full order system. Also, we analyze the effectiveness of the proposed decentralized controller for various spatial configurations. The simulations are performed using parameters from the prototype lattice-based composite wing structure shown in Figure 5.15. We can see that there are 16 ribs on each wing and they represent a clamped-free lumped-mass system, as illustrated in Figure 5.10. The pertaining structural properties are listed in Table 5.2. The rotational spring stiffness is calculated based on the bending stiffness of the wing, while the mass is estimated by taking the weight of the wing divided by the number of ribs. The damping is an estimate of the combined internal damping and energy loss due to joint friction, and it is assumed to be tiny. As indicated, we utilize the Houbolt integration scheme.

In this study, it is assumed that the wing is subjected to a uniform impulse torsional disturbance of $1N-m$ over $10\mu s$, and initially, the control input is applied to mass m_9. This is a single control input case. By following the left and right propagation

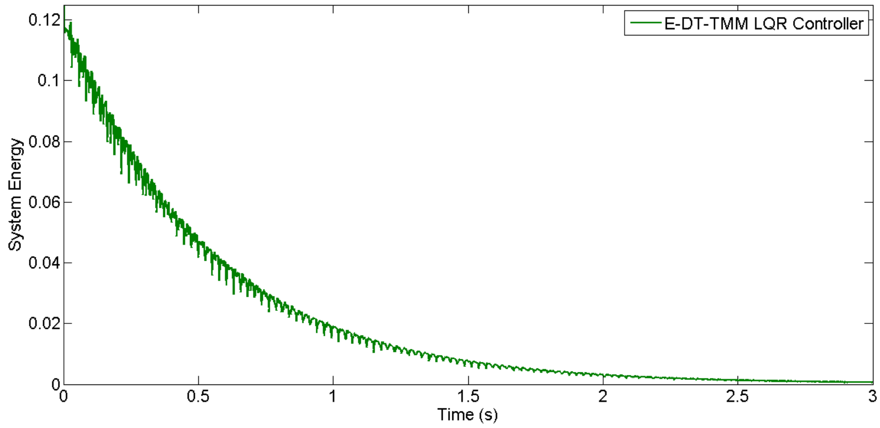

Figure 5.16: Total system energy with E-DT-TMM based decentralized LQR controller.

presented in Section 5.2.3.3, a reduced-order localized subsystem can be developed as shown in (5.55). From there a discrete-time LQR controller can be designed using $Q = I_3$ and $R = 1e^5$. Figure 5.16 shows the total system energy of the lumped-mass system, from which we can see that the proposed E-DT-TMM based decentralized controller does regulate the overall system. The total system energy considered here consists of kinetic and potential energy of the entire mass-spring-damper system. Though not shown here, for an open-loop case, the average total system energy is more than an order of magnitude higher than the highest shown in Figure 5.16. To better understand how well the E-DT-TMM based controller performs compared to the full state continuous LQR controller, the Pareto optimal curves for both controllers are generated, and the comparisons can be seen in Figure 5.17. The result shows that when the available control energy is low, the full state continuous LQR controller performs better, but as the allowable control energy increases the performance of these two controllers becomes comparable. This suggests that the proposed E-DT-TMM based controller, which only

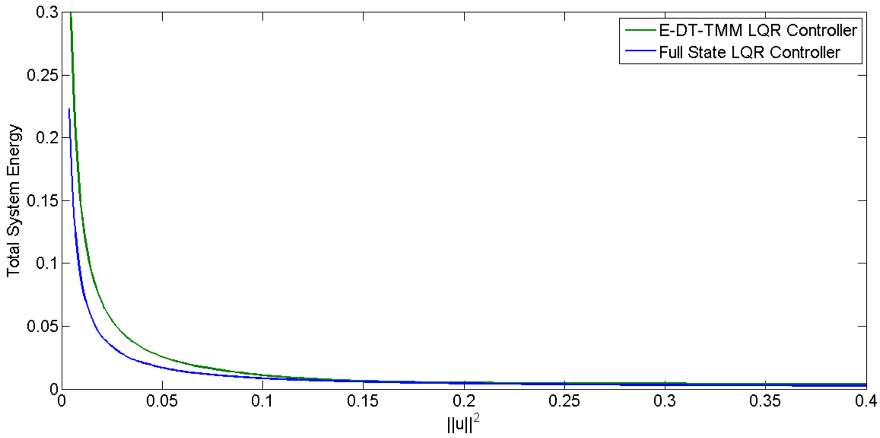

Figure 5.17: Comparison of the Pareto optimal curves between E-DT-TMM based decentralized LQR controller and full state LQR controller.

uses the local state information, is as effective in controlling the overall system. This observation will be further illustrated later.

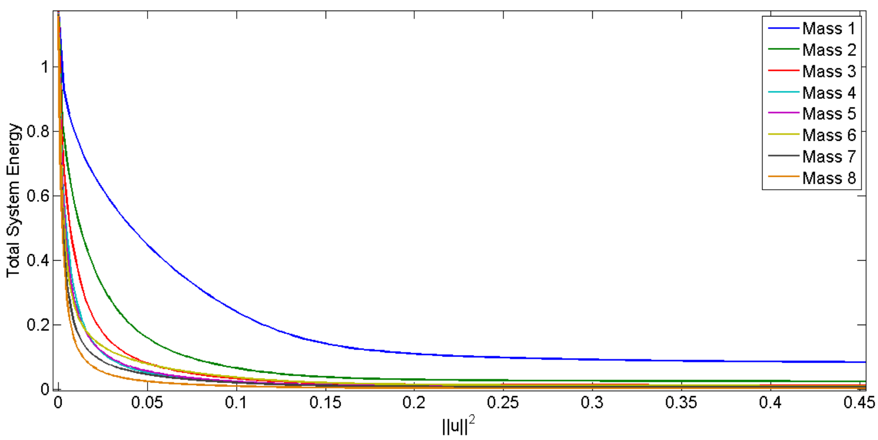

Figure 5.18: Total system energy with E-DT-TMM based decentralized LQR controller as control input applied from mass m_1 through mass m_8.

Next, the performance and effectiveness of the proposed E-DT-TMM based controller are studied by varying its applied location from m_1 to m_{16}. Figure 5.18 shows the total system energy when the control input is applied one at a time from m_1

to m_8, while Figure 5.19 shows from m_9 to m_{16}. As expected, depending on the location

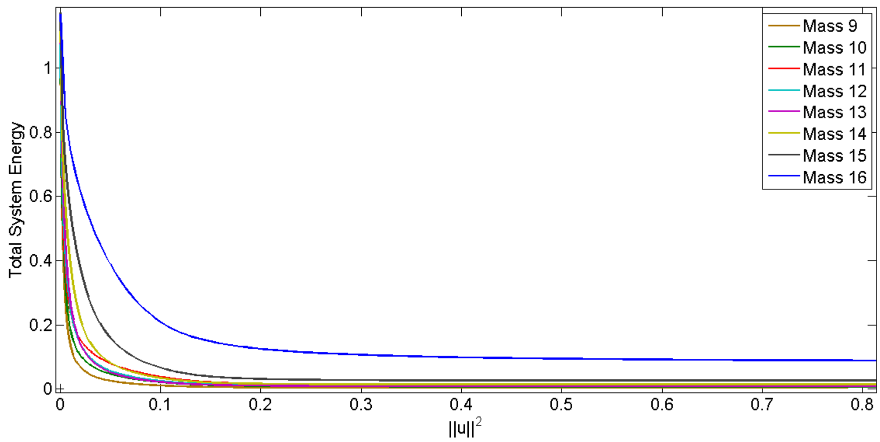

Figure 5.19: Total system energy with E-DT-TMM based decentralized LQR controller as control input applied from mass m_9 through mass m_{16}.

of applied input and its relationship with the corresponding mode shapes, the control performance at some locations are deemed better than the others. This confirms with the common understanding in structural control that the level of controllability of a structural mode is directly affected by the location of control input. Therefore, as we can see from the Pareto optimal curves, the control actuation is more effective when it is applied near the center, where all the structural modes appear to be eminent, and least effective when it is applied at both ends, where some primary modes are least controllable hence require higher control energy. To compare the closed-loop responses between the proposed discrete decentralized LQR controller and the full state continuous LQR controller, Figures 5.20a through 5.20c shows the torsional displacement comparisons at m_1, m_9, and m_{16}, respectively, when the control input is applied at mass m_9.

These figures show the performance of the full state LQR controller is some-

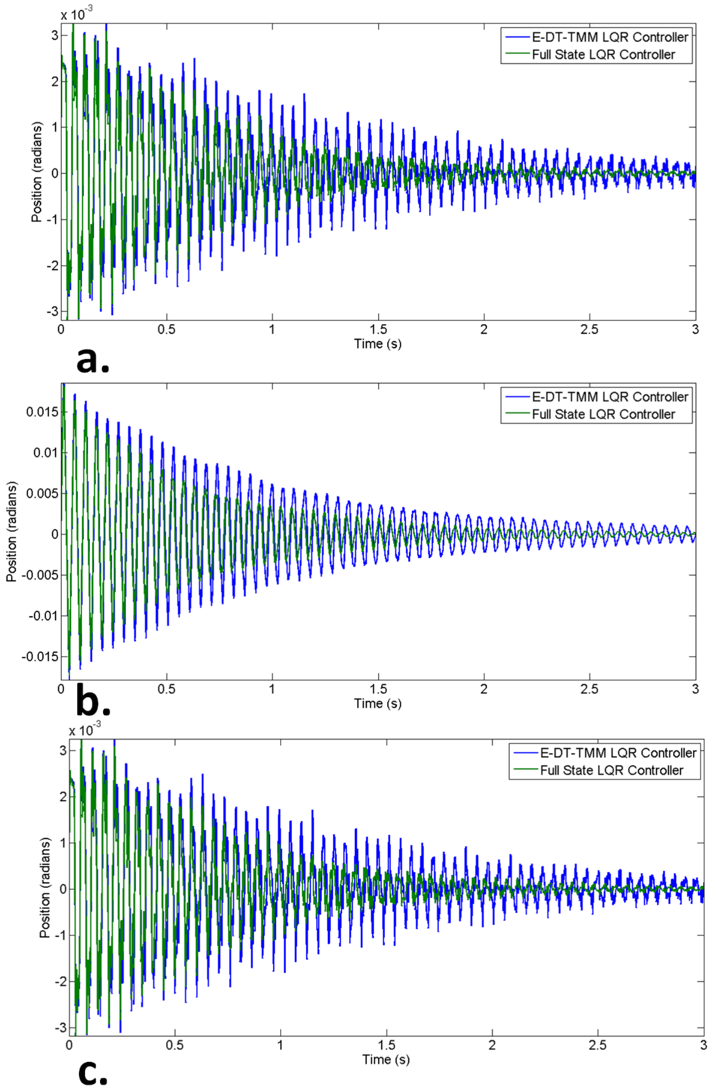

Figure 5.20: a) Torsional displacement at mass m_1, b) torsional displacement at mass m_9, and c) torsional displacement at mass m_{16}, when input is applied at m_9.

Table 5.3: Total system energy comparison: Two control inputs

Control inputs	(8,9)	(7,10)	(5,13)	(3,15)
Total System Energy (J)	22.968	8.530	8.678	23.934

what better, which is because, in generating these time responses, we have used the same lower control energy for both controllers. Therefore, as was shown in Figure 5.17 the total system energy for E-DT-TMM case is higher at lower control energy. Hence we observe shallower rate of convergence for the closed-loop response. Nonetheless, these figures demonstrate that the proposed E-DT-TMM based decentralized controller can suppress the torsional vibration effectively, by utilizing only the local state information.

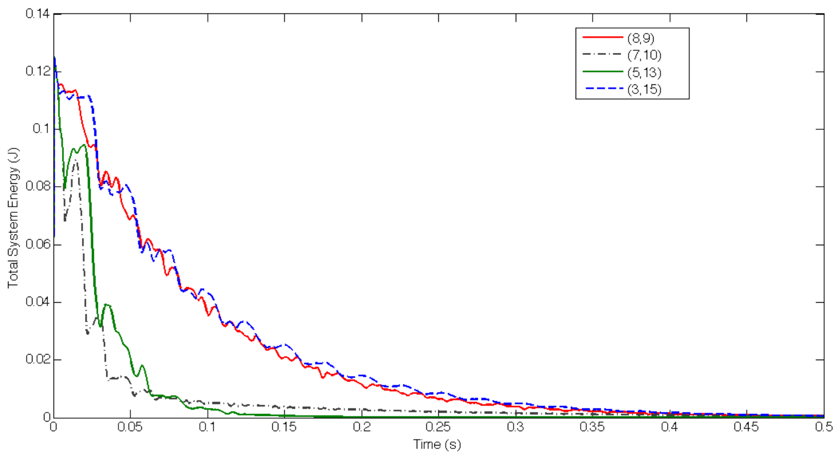

Figure 5.21: Time response of the total system energy at the four pairs of input locations.

For a single input case, we showed that it was most efficient when applied at or near the center of the structure. However, in the case of multiple control inputs, the placement of actuation becomes a little sophisticated. For illustration, here we consider a case of two control inputs. By following the model reduction process presented in Section 5.2.1 for each control input, we obtain two reduced-order models as shown in (5.58), and their mathematical descriptions would depend on where the control inputs are applied. For comparisons, we consider only four pairs of mass locations: (8,9), (7,10), (3,15), and (5,13). Table 5.3 shows the comparisons of the total system energy for the four pairs of input locations, while subjected to similar levels of control input energy. Figure 5.21 shows the time response of the total system energy and Figure 5.22 the time response at the tip mass (i.e. m_{16}). It was shown earlier for single input case that control actuation at either mass 8 or mass 9 rendered the best performance. It is interesting to observe that the combined actuation at these two locations does not make a favorable result, as evidenced in Table 5.3 and Figures 5.21-5.22. The reason

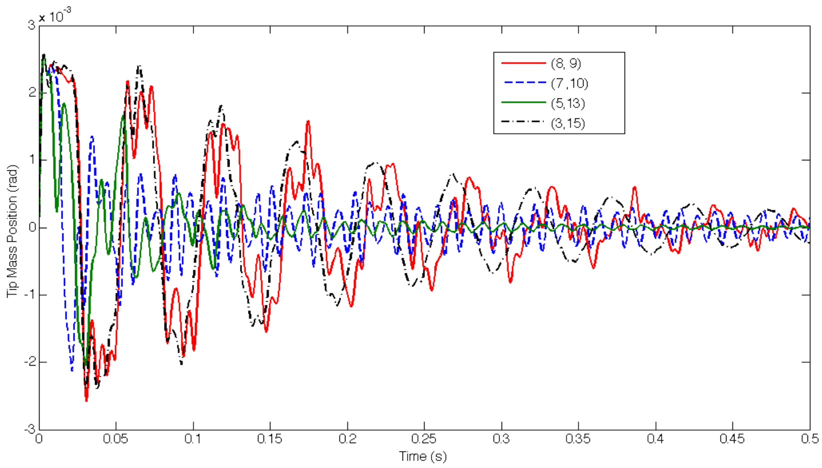

Figure 5.22: The tip mass displacement comparisons at the four pairs of input locations.

is that when two actuation are adjacent to each other, their effective range becomes redundant or may even cancel out the total efficiency. In the case of the pair (3,15), though the two masses are farther apart, their individual performance was rather poor; see Figures 5.18 and 5.19, hence the combined effect is not getting better. Pairs (7,10) and (5,13) show a good spatial separation as well as a good individual performance from the earlier analysis. Hence their collective efforts are best reflected in the proposed state propagation approach and are more efficient in suppressing overall vibrational motion. In summary, the study shown here can be used as a guideline for determining the placement of control actuation when there are multiple control inputs.

5.3 Active Twist Aircraft Control and Estimation

To effectively create a controller to enable active twist, the control derivatives of the flight platform must be estimated. The development of an aerodynamic database containing the appropriate collection of control derivatives will be the first sub-task, and the subsequent evolution of the control laws will be the second subtask.

5.3.1 Creation of Aerodynamic Database

The creation of an aerodynamic database is necessary to create a useful localized linear model. The ideal scenario would be to generate the aerodynamic derivatives via a combination of wind tunnel and flight testing, but for this project, we will be using the methodology highlighted in Section 3, which allows for the active twist of the wing to be simulated.

Figure 5.23 shows the geometry of the wings used to develop the aerodynamic database. To determine the appropriate amount of panels for the simulation (for nu-

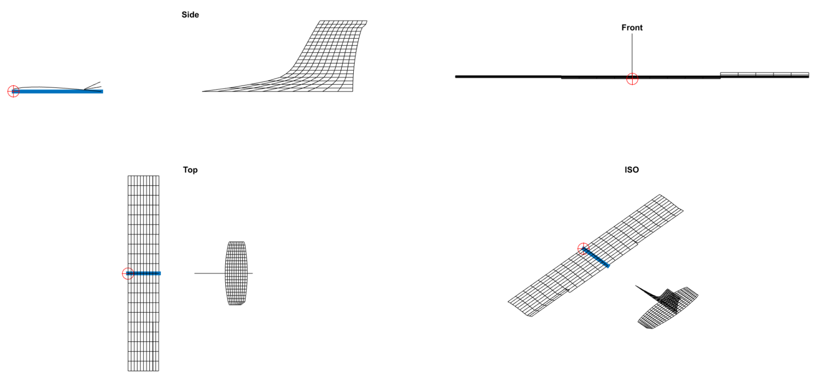

Figure 5.23: Simulated wing geometry used to generate the aerodynamic database in the Dynamic Tornado VLM tool

merical convergence), we inspected the convergence of the pitch stability derivative as a function of the spanwise and chordwise resolution of segments. This was done by first setting the number of chordwise segments and then increasing the number of spanwise segments until convergence was reached. The number of spanwise segments where the pitch stability derivative converged was then used as the number of chordwise segments was then varied until the pitch stability derivative converged. The convergence plots are shown in Figure 5.24.

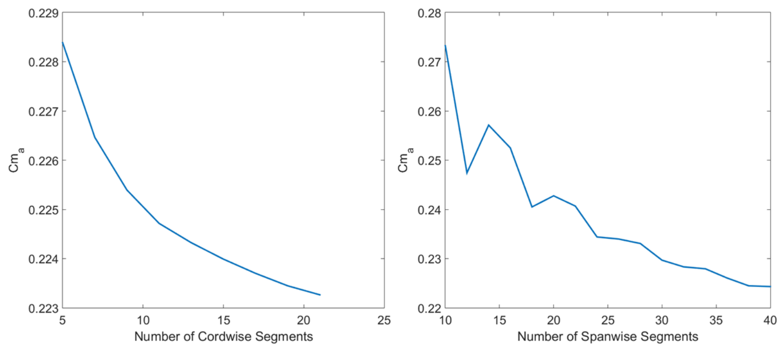

Figure 5.24: Pitch stability derivative convergence study

Figure 5.25 shows a comparison between the flaperons and tip twist effect on the pitch moment coefficient as angle of attack changes. It can be seen that the angle of attack has the largest effect on the pitching moment, which is to be expected, and that both control approaches retain their shape as the angle of attack changes. This was also true for the sideslip and airspeed, suggesting that the linearization presented in the next section is a reasonable assumption. The pitching moment coefficient also remains fairly flat for the flaperon in comparison to the tip twist, which validates the assumption that the flaperons do not contribute much to the pitching moment around the primary wing and can be ignored.

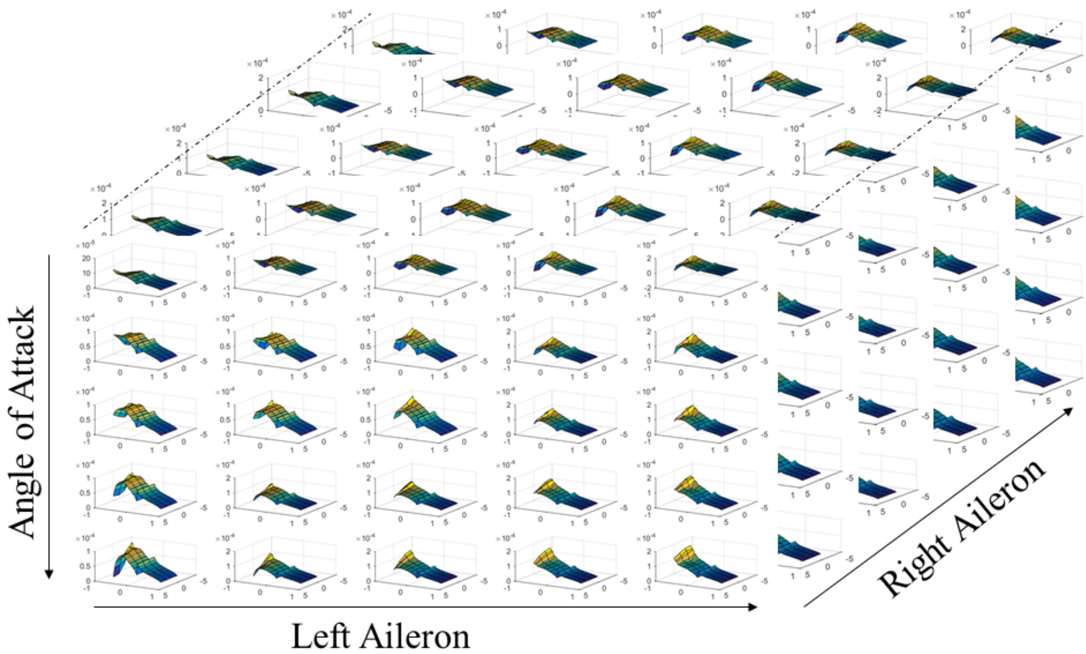

Figure 5.25: Comparison of changing C_m with alpha and flaperons and alpha and tip twist

5.3.2 Control and Estimation Development

The goal of the control design is to have a standard autopilot for this effort a Pixhawk perform the rigid body control to determine the necessary yaw, pitch, and roll, while a lower level controller will control the ailerons and the wing twist. This hierarchical control architecture gives the added advantage of allowing the autopilot to be used to easily extend the autonomous flight zone. Figure 5.26 shows a block diagram of the control design.

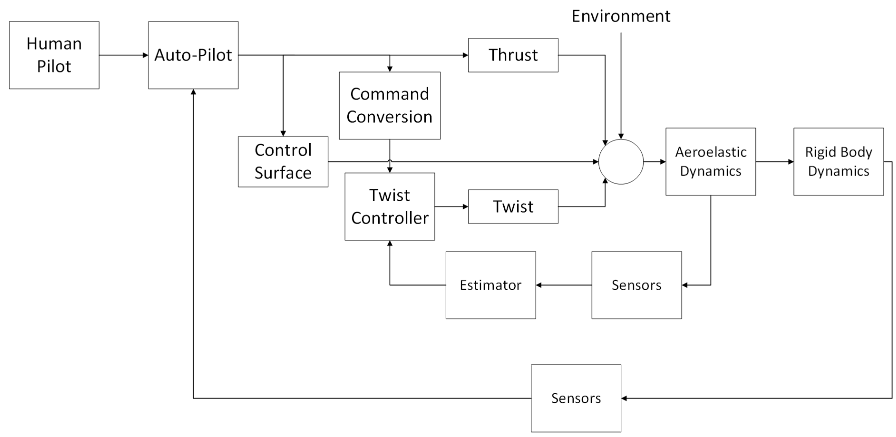

Figure 5.26: Hierarchical control architecture includes an outer-loop controls the rigid-body dynamics of the aircraft while an inner-loop provides aileron and wing twist control

The "Command Conversion" block on the chart exists to perform an appropriate conversion between the output of the off the shelf autopilot, and the necessary commanded control surface positions. The twist controller block is where the lower level twist controller is implemented. It starts with the creation of the aeroelastic model. In this case, we will be only looking at the twist because of the wing design there should be very little bending in the spanwise and chordwise directions. Equation5.63 shows the coupled aeroelastic state equation where M is the beam theory mass matrix for the twisting wing, C is the beam theory damping matrix, K is the beam theory elastic matrix, $M(\alpha, \beta, U_\infty, \theta, \delta)$ is the aerodynamic moment function that is dependent on, α - angle of attack, β - side slip, U_∞ - airspeed, θ - tip twist, δ - control surface displacement, B_{Twist} is the input matrix, and U is the torque input.

$$M\ddot{\theta} + C\dot{\theta} + K\theta + M(\alpha, \beta, U_\infty, \theta, \delta) = B_{Twist}U \tag{5.63}$$

The model can then be linearized and combined with the output and reference matrices to achieve the below system of equations.

$$\begin{aligned} \dot{X} &= AX + Bu + E \\ y &= CX \\ \theta_{tip} &= HX \end{aligned} \tag{5.64}$$

where,

$$A = \begin{bmatrix} 0 & I \\ M^{-1}(K + qScC_{m_\theta}) & 0 \end{bmatrix} \tag{5.65}$$

and q is the dynamic pressure, S is the sectional wing area, c is the sectional cord, and C_{m_θ} is the diagonal matrix containing the local twists pitching coefficient.

The torques is being directly applied to the wing resulting in

$$B = \begin{bmatrix} 0 \\ M^{-1} \begin{bmatrix} 0 \\ \vdots \\ 1 \end{bmatrix} \end{bmatrix} \tag{5.66}$$

and

$$E = \begin{bmatrix} 0 \\ qSc(C_m \alpha I + C_{m_\beta} \beta I) + M_{U_\infty} U_\infty I) \end{bmatrix} \tag{5.67}$$

where C_{m_α} is the coefficient of the pitch on angle of attack, C_{m_β} is the coefficient of pitch on sideslip, and M_{U_∞} is the pitching moment with respect airspeed. C s the linearized conversion from tip twist to acceleration and H is returning tip twist. The flaperons pitching moment contributions are not included in the linearized model because preliminary results of the aerodynamic database showed that $M^{-1}C_{m_\delta} << M^{-1}B_{Twist}$. The A matrix and the E matrix are populated from the aerodynamic database.

For the controller design, an LQ setpoint tracking controller similar to the one presented by Young *et. al.*[85] was used where the error between the set point and the desired tip twists are minimized, the error equation is shown below.

$$e = \theta_{cmd} - \theta_{tip} \tag{5.68}$$

Resulting in

$$e = \theta_{cmd} - HX = M\theta_{cmd} - HX \tag{5.69}$$

where M is the identity matrix. The States are then augmented with the integration of the error.

$$z = \begin{bmatrix} x : x_i \end{bmatrix}^T \tag{5.70}$$

A controller can then be developed to minimize the cost function

$$J = \frac{1}{2}\int_0^\infty (z^T Q z + u^T R u)dt \tag{5.71}$$

which gives the following gain matrices

$$\begin{gathered} K_x = R^{-1}B^T P \\ K_{\theta_{cmd}} = R^{-1}B^T(PVR^{-1}B^T - A^T)^{-1}(H^T QM + PG) \end{gathered} \tag{5.72}$$

where P is the solution to the algebraic Ricattic equation and G is the solution to the feedforward gain vector equation. We will combine these with an additional feedforward gain to counter E, resulting in the control shown below.

$$u = -K_x X - K_{\theta_{cmd}}\theta_{cmd} \tag{5.73}$$

The aeroelastic model was created as described above where the state matrix was the combinations of the elastic beam twisting matrix and the local pitching coefficients that are calculated using N-dimensional linear interpolation of the aero database. The simulation contains implementable controllers and a hybrid extended Kalman filter.

The extend Kalman filter assumes a system model of

$$\begin{aligned} \dot{x}(t) &= f(x(t), u(t)) + w(t) \\ z(t) &= Cx(t) + v(t) \end{aligned} \tag{5.74}$$

where $w(t)$ is the model noise, $v(t)$ is sensor noise, $x(t)$ are the twist states, z(t) is the sensor output, and

$$f(x(t), u(t)) = \begin{bmatrix} 0 & \dot{\theta} \\ M^{-1}(K + qScM(\alpha, \beta, U_\infty, \delta)) & 0 \end{bmatrix} + B_{Twist}U \tag{5.75}$$

The estimation of the state and covariance derivatives are

$$\dot{\hat{X}} = F(t)X + B_{Twist}U\dot{P}(t) = F(t)P(t) + P(t)F(t)^T + Q(t) \tag{5.76}$$

where,

$$F(t) = \left.\frac{\partial f(x)}{\partial x}\right|_{\hat{x}} \tag{5.77}$$

which is estimated by the interpolation of the aero database. Estimates of $\hat{X}_{k|k-1}$ and $P_{k|k-1}$ are taken from the integration of the calculated derivatives above. This integration is done by a fourth order Runga-Kutta method, the results of which are used to create the Kalman gain

$$K_k = P_{k|k-1} H_k^T (H_k P_{k|k-1} H_k^T + R_k)^{-1} \tag{5.78}$$

The Kalman gain is then used to create an estimate of state and covariance matrix.

$$\begin{aligned} \hat{X}_{k|k} &= \hat{X}_{k|k-1} + K_k(z_k - C\hat{X}_{k|k-1}) \\ P_{k|k} &= (I - K_k C) P_{k|k-1} \end{aligned} \tag{5.79}$$

5.3.3 Numeric Results

Two simulations were performed to access the capabilities of the active twist configuration, the first is the ability of the configured wing to generate proverse yaw and the second is the ability to avoid tip-induced stall.

5.3.3.1 Proverse Yaw Turn Numeric Simulation

This simulation was intended to mimic flight patterns so the angle of attack started off at eight degrees and slowly decreased until the plane reaches cruise conditions, as is shown in Figure 5.27 a). To create a proverse yaw effect the ailerons and twists were commanded in opposing saw tooth patterns an example of the twist pattern is shown in Figure 5.27 b).

In the simulation, the sensor noise is added by decomposing the known twist angles into their proportional gravitational values and then added in the white noise observed from the accelerometers reading into the Beaglebone Black. The noise is then

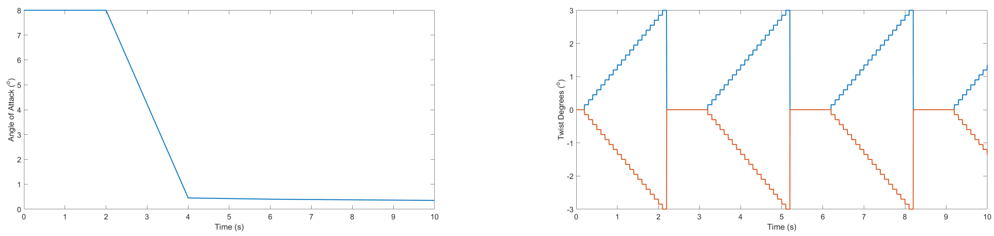

(a) Angle of Attack (b) Twist Pattern

Figure 5.27: Simulation parameters, the angle of attack replicating take off and the commanded twist pattern

rounded off to the nearest least significant digit to simulate the ADC. Then the inverse tangent is taken of the noisy measurements in the same way it would be from raw data to create the local twist. The same process is done for the gyro readings though since they directly measure the twist rate the noise can be directly added. A periodic disturbance is applied to the wing to represent environmental conditions. The controller as described above is implemented with the integration of the error being done by a fourth order Runge-Kutta method. There are also sample times enforced for the actuation, sensing, and estimation of the state matrix.

The figure above shows that the estimator does a good job but that the controller can achieve the commanded tip twist prior the next discrete command is given which is an indication that the performance desired twist pattern can be achieved.

5.3.3.2 Stall Mitigation Numeric Simulation

Part of the project goal is to show tip-induced stall mitigation. For the current configuration, the whole wing will go into stall due to its uniform stiffness but we can still

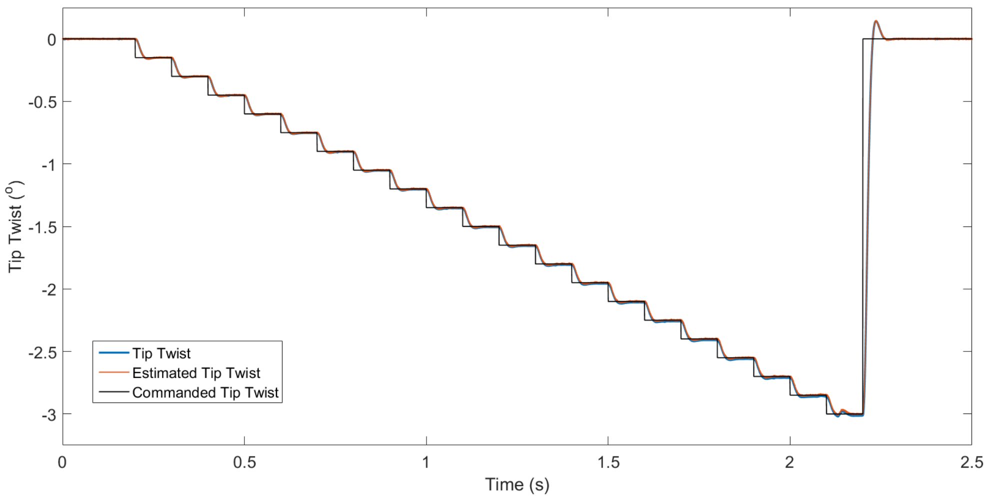

Figure 5.28: Comparison of the commanded, estimated, and actual tip twist in the simulation

simulation the necessary techniques to avoid stall.Stall begins around eight degrees angle of attack. As a means of avoiding stall, a stall avoidance protocol was implemented. This protocol uses the same control law developed above but with the command switching from zero to eight degrees minus the current angle of attack when the angle of attack is above eight degrees.

All the same parameters for the noise and disturbances as described in the previous section were applied here as well. In this case, though the ailerons were not altered as it is assumed the plane is flying in a straight line. The angle of attack was an oscillating sine wave of amplitude three degrees about seven degrees.

The figure above shows that when the angle of attack exceeded the stall quotient that the tips twisted down to avoid stall.

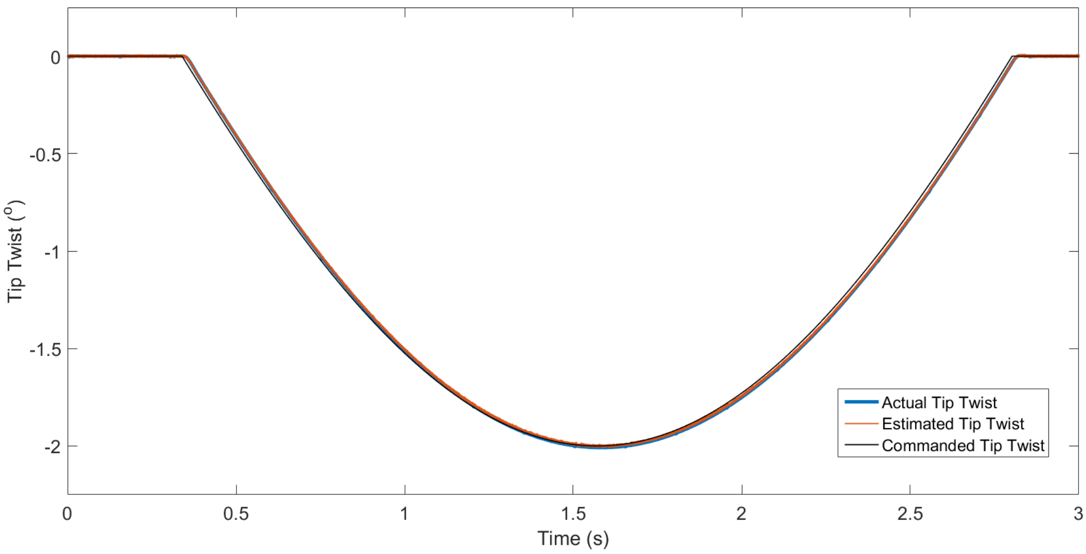

Figure 5.29: Actual, estimated, and commanded tip twist for stall mitigation

5.4 Optimal Active Wing Twist Patterns

The controllers that we established in the earlier sections addresses the structural stability of wing and aeroelastic tracking of the wing tip. What still needs to be addressed is the what sort of tracking profiles is optimal for the desired flight regime.

Since the developed digital wing is capable of band-limited active twisting, a unique and intriguing aerodynamic phenomenon was observed during the wind tunnel tests, in which we found that the aerodynamic lift /drag performance can be modulated as a function of wing twist frequency, and there revealed an apparently preferred wing twist pattern for improved aerodynamic performance. Here is a summary figure to highlight this frequency-dependent aerodynamic performance. Figure 5.30 shows the lift-drag ratio as a result of tip twist oscillation at 4 Hz. The green line is the static

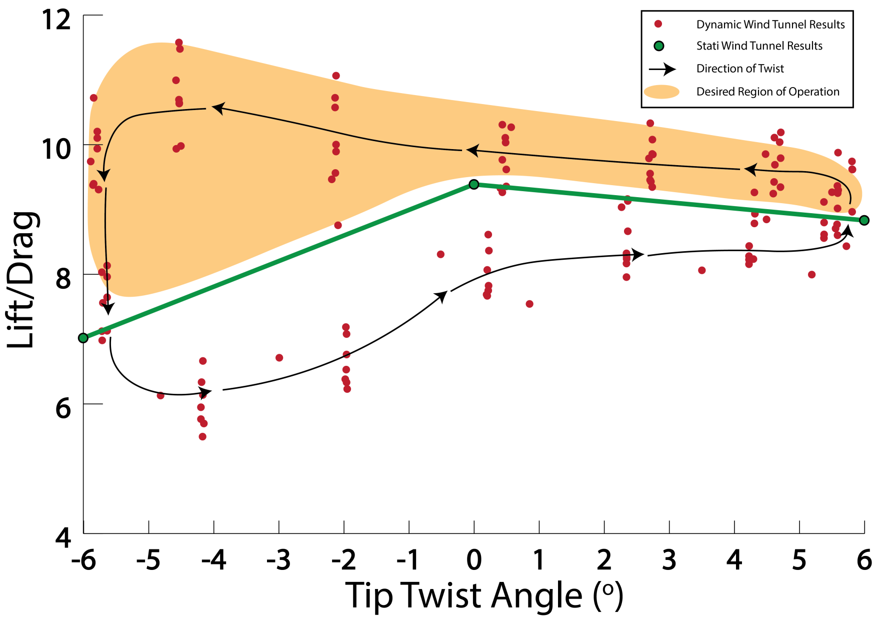

Figure 5.30: Lift drag ratio of the dynamic twisting at 4 Hz frequency compared with the static wind tunnel result

lift-drag ratios measured at those tip twist values, and the yellow region is an area of increased lift performance that we would like to be operated at. The wing twist frequency and its correlation with lift performance is a research subject that has never been explored in the past. This paper is inspired by this observation, and we leverage it to study the application of frequency-based lift/drag modulation to enable additional flight mission design capabilities.

To take advantage of this observed modulation, a mathematical aerodynamic wing model is developed by integrating the structural finite element modeling with the unsteady vortex lattice method. This is then used to simulate the wing twist patterns so that the results can be validated with the actual wind tunnel data for model verification. Second, a neural network model is trained to model/learn the aerodynamic and structural interaction arising from the active twist capabilities by utilizing the wind tunnel data. Finally, these two models are then used to determine the optimal wing twist patterns via constrained optimization process.

Neural networks have widely been researched and applied to various technical areas, including the fields of aerodynamic and aeroelasticity. For instance, in Linse and Stegel [39] neural networks were used to identify the aerodynamic coefficients so that a model-based flight controller can be developed. More recently, neural networks have been utilized as a means of airfoil shape optimization by combining multiple neural networks that were trained for single optimization, and then combined for multi-objective optimization [60, 58, 59]. Natarajan et. al [48, 49] used the neural networks to first train for faster simulation and then to perform optimization of distributed airfoil bumps for yaw control [48] and flutter suppression [49]. Additional works have focused on using the neural networks as a means of generating gain values for the adaptive controllers [38] or for the next time step control state prediction [82].

5.4.1 Aeroelastic modeling

The aeroelastic modeling used for this study is the same configuration shown in Section 3.2 except that instead of the full aeroelastic model we will only be looking at the twist states. Where the state vector is

$$\Theta = [\theta_1, \theta_2, \cdots, \theta_{m-1}, \theta_m]^T \tag{5.80}$$

This is done because of how stiff the wing is in the spanwise and chordwise directions making the contributions from those flexations slight. This change results in the following abbreviated aeroelastic definitions.

The local aeroelastic wind velocity vector at each collocation point can be given by

$$U_{i,j} = \begin{bmatrix} U_\infty & 0 \end{bmatrix} R^T(\alpha_{root}) + \begin{bmatrix} \dot{\theta}_i |d_j| & 0 \end{bmatrix} R^T(\theta_i)\,,\ i = 1, \cdots, m\,,\ j = 1, \cdots, q \tag{5.81}$$

where $R(\cdot)$ denotes a 3×3 rotational matrix, α_{root} is the angle of attack at the wing root, U_∞ is the airspeed, $|d_j|$ is the magnitude of the position vector d_j from torque tube axis to collocation point j, θ_i is the twist angle at ith panel, and $\dot{\theta}_i$ its rate. It should be noted that the local wind velocity $U_{i,j}$ defined in (5.81) is a tall matrix of dimension $mq \times 3$. To simplify the subsequent presentation, we rewrite its notation to be just U_i, where $i = 1, \cdots, mq$. Then, the local aeroelastic angle of attack at each collocation point can be determined by

$$\alpha_i = \tan^{-1}\left(\frac{U_{iz}}{U_{ix}}\right)\,,\ i = 1, \cdots, mq \tag{5.82}$$

where U_{ix} and U_{iz} denote the x and z components of U_i.

5.4.2 Friction drag estimation

The vortex lattice method described above only considers the lift-induced drag. While the lift-induced drag is a significant part of the overall drag, the skin friction can be a dominant drag force [77], especially at the flow of low Reynolds number. To compensate for the shortcoming of vortex lattice method, we adapt to use the equivalent parasite area method presented in [23]. The coefficient of drag from friction is defined as

$$C_{D_f} = \frac{1.1}{S}\sum_{i=1}^{3} F_i \tag{5.83}$$

where S is the reference surface area and

$$F_i = C_{F_i} \times CF \times IF_i \times FF_i \times S_{wet_i}\,. \tag{5.84}$$

Eq. 5.84 is the total friction force at each part of the aircraft component; in this case, fuselage and two wings. C_{F_i} is the skin friction coefficient at each region and the rest of the parameters are constants to modulate the skin friction coefficient. CF is the compressibility factor, IF_i the interference factor, FF_i the form factor, and S_{wet_i} the wetted surface area. The details of these values can be found in [23], except for C_{F_i} which we use the adjusted Prandtl-Schlinting formula to adjust for laminar flow and is given by [6]

$$C_{F_i} = \frac{0.455}{(\log_{10} Re_L)^{2.58}} - \frac{1700}{Re_L} \tag{5.85}$$

where Re_L is the Reynolds number. In addition, the wetted surface area of the wing S_{wet_i} is adjusted according to the arear curvature as given below [6],

$$S_{wet_i} \approx 2.0\left(1 + 0.2\frac{t}{c}\right) S_w \tag{5.86}$$

where t is the thickness of the airfoil, c is the cord length, and S_w is wetted surface area.

This estimate of C_{D_f} is then calibrated with the zero-lift drag coefficient from the wind tunnel data to help compensate for other unaccountable factors.

5.4.3 Neural Network Model Development

In this study, the MATLAB Neural Network package was used to generate and train the proposed neural networks model. We used a total of 174 wind tunnel test sets collected at 50 Hz, and no filtering was applied.

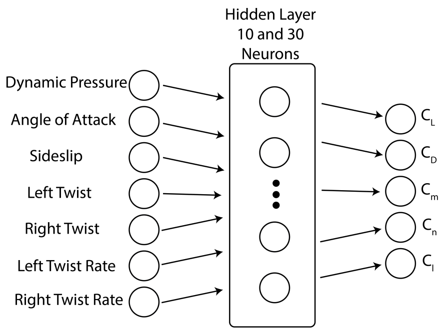

(a)

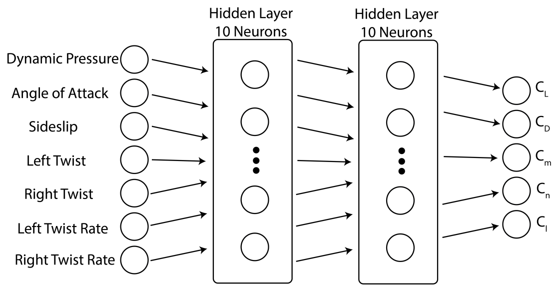

(b)

Figure 5.31: Neural network geometry, a) a single hidden layer with 10, 30 neurons b) two hidden layer with 10 neurons per layer

The collected wind tunnel data consists of 129 static wing twist tests and 45 dynamic wing twist tests. Of the 129 static tests, 100 were from the symmetric wing twist, while the remaining 29 tests were from the asymmetric twist. Also, all 45 dynamic wing twist tests were from symmetric wing twist, in which 33 of them were obtained by varying the dynamic pressure from 1 to 7 PSF.

To generate an appropriate neural network model for optimum wing tip twist pattern determination, a feed forward network configuration was used, where the wind tunnel data were divided randomly into training data, validation data, and testing data at a ratio of 65 %, 15 %, and 20 %, respectively. The input data are dynamic pressure, right wing twist angle, left wing twist angle, right wing twist velocity, left wing twist velocity, angle of attack, and sideslip angle.

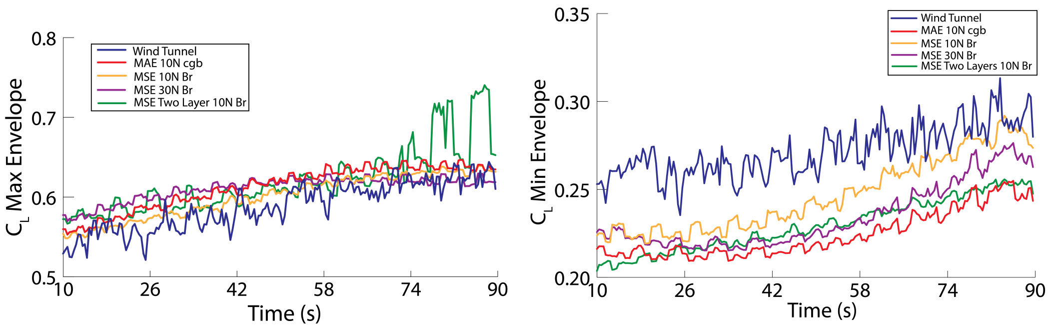

(a) (b)

Figure 5.32: Comparison of maximum (a) and minimum (b) C_L envelopes for neural networks

The data set described above was used to train several different neural network configurations by utilizing different gradient decent training methods to assess the effects of various neural network geometries and training methods on the accuracy of the resulting model. Figure 5.31 shows the geometry of the proposed neural networks. A single layer with ten neurons in the hidden layer and an output layer was the configuration most often used, but a configuration with 30 neurons in the hidden layer was also used. Finally, a network with two hidden layers with ten neurons in each layer was developed as well. Every layer included a biasing variable including the output layer and a log-sigmoid for the transfer function. The networks were either trained with Bayesian regularization back propagation (Bayesian) or scaled conjugate gradient backpropagation (SCG), and the cost function was either mean squared error (MSE) or mean absolute error (MAE). The training was completed either after 1000 iterations or once the error gradient was found smaller than $1e^{-7}$. The results of the training are given in Table 5.4. Table 5.4 shows that the two layers Bayesian regularization

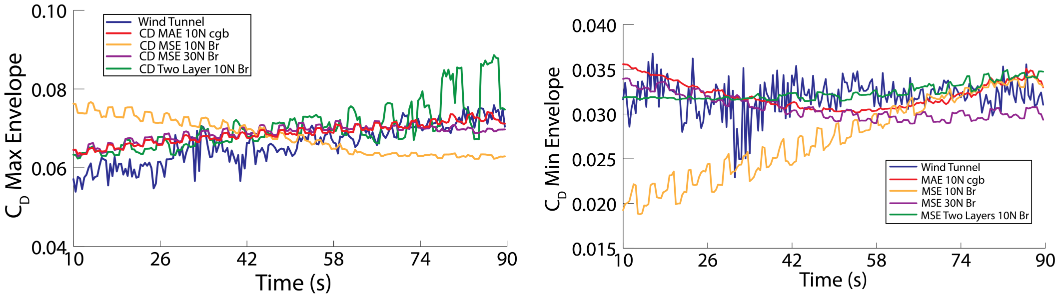

(a) (b)

Figure 5.33: Comparison of maximum (a) and minimum (b) C_D envelopes for neural networks

Table 5.4: Performance of neural networks on training data

Hidden Layers	Neurons/Layer	Training	Cost	Performance
1	10	SCG	MAE	0.0181
1	10	SCG	MSE	0.0014
1	10	Bayesian	MSE	$9.5029e^{-4}$
1	30	Bayesian	MSE	4.6576^{-4}
2	10	Bayesian	MSE	$4.4932e^{-4}$

neural network resulted in the best model. To provide some context of the performance difference, we consider the same test run presented in Section 4.4.2. Figure 5.32 shows the envelope of lift coefficient derived from the neural networks. Figure 5.32(a) shows the maximum lift coefficients within twenty samples, whereas Fig. 5.32(b) shows the minimum lift coefficients over the same sample group. Figure 5.33 shows the drag coefficient envelope for the same run. As shown in these results the neural network models were able to generate aerodynamic characteristics that are agreeable with those from the wind tunnel data. It should be noted in Figures 5.32 and 5.33 that the two-layer neural network model produces notable spikes toward the end of simulation time, this is because the dynamic pressure in the experiments was very noisy, and the two-layer model was more sensitive to the variations of dynamic pressure. This was a trade-off allowing for better accuracy in the mid-range dynamic pressures for worse accuracy at the high end, and this is acceptable because we would be performing the optimization in the mid-range.

5.4.4 Constrained Optimization

The aeroelastic model and the neural network model developed in the previous sections were for replicating and assessing the effectiveness of active wing twist on the aerodynamic effects. In this section, these models are used to determine an optimal wing twist pattern for a given flight profile. To formulate this problem, the Sparse Nonlinear OPTimizer (SNOPT) program developed by Gill *et al.* [17], in which a constrained optimization problem can be formulated as the minimization of a cost function subjected to a list of physical constraints, was used.

In this study, the design objective of optimal wing twist pattern determination is to find a wing twist pattern that minimizes the drag while subjecting to various of wing tip twist constraints for cruise trim conditions. Specifically, the constrained optimization problem considered in this study can be formulated, for either aeroelastic model or neural network model, as follows,

$$
\begin{aligned}
& && \min\{D\} \\
& \text{subject to:} && \text{Aeroelastic or Neural Network Model, and} \\
& && a)\ \ 0.99W \le L \le 1.01W \\
& && b)\ \ -6^\circ \le \theta \le 10^\circ \\
& && c)\ \ \ddot{\theta}_m \le |\ddot{\theta}_{max}| \\
& && d)\ \ \theta_m(t_0) = \theta_m(t_f)
\end{aligned}
\tag{5.87}
$$

where D and L denote the drag and lift forces, respectively, and W the aircraft weight. To maintain allowable cruise altitude, the lift was constrained to be within 1 % of W as in a). However, this bound can be made tighter if needed. In addition, the amount of tip twist angle is physically constrained by b), and the maximum frequency for the tip twist is approximately 5.4 Hz, which can be used to calculate the maximum tip twist acceleration as a means of enforcing actuator limitations without adding additional states, as shown in c). Furthermore, it is necessary to constrain the final tip twist to be equal to the initial tip twist as shown in d). otherwise, the trim conditions would be violated.

The optimization is performed assuming that the tip twist states are separated by 0.02 sec and that the simulation lasts for 2 sec. The angle of attack α is set to be 2.32°, an initial condition that meets the lift requirement without wing twist, and the sideslip angle β is assumed to be zero.

The results from the constrained optimization process reveal some interesting insights into the optimal wing twist behaviors. These results are presented next by utilizing the neural network and aeroelastic models developed earlier.

5.4.5 Results from the Neural Network Model

Recall the cost function described in Section 5.4.4. The optimization using the neural network model takes about 2 to 5 hours per optimization run. We can see in Fig. 5.34 that not one but multiple optimal twist patterns are identified when using the neural network model. This is because the cost function has a null space since there are many ways to minimize drag through maneuvers

Table 5.5: Optimized average C_L and C_D

Initial Frequency (Hz)	C_L	C_D
0	0 .120	0.0313
1	0.121	0.0320
2	0.120	0.0313
3	0.122	0.0318
4	0.120	0.0313
5	0.123	0.0311

To assess the sensitivity of the optimal wing twist pattern, the frequency of the intial sine wave was varied and its effects studied. Table 5.5 shows that the initial conditions do impact the final value of the cost function, though the variance is small. The variation in the optimal drag based on initial conditions is around 0.05 N or about 2.8 % of the average optimal drag.

From the static wind tunnel test data at a given lift requirement, the C_D coefficient is around 0.033, which results in a drag reduction of 3% to 5.75% for the drag values listed in Table 5.5. Figure 5.34 shows in blue the initial twist pattern, and in orange, the optimal twist pattern resulted from the constrained optimization. The initial conditions affect the general shape of the optimal twist pattern. It also shows that no matter what the initial frequency is, the optimal solution results in a sawtooth pattern but that the optimized result tends to retain the original frequency content. This could be used as a means of adapting to the requirements during actual implementation. Eventually, these optimal patterns can be extended to other patterns for various environmental conditions and flight demands, and they can be combined to best tailored to achieve a near optimal solution.

Figure 5.34 also shows the lift and drag coefficients for the optimal twist pattern. It should be noted that in general the drag is reduced via swift downward twists, but it does not start increasing at the same time the lift does. In fact, it does not start growing until lift induced drag dominates. This effect and the effect of viscosity explain the phase shift that seen between the twist pattern and the drag pattern. Note that these effects are somewhat frequency dependent, by the time it gets to 5 Hz, as shown in Figures 5.34 d), most of the behavior is dominated by lift-induced drag, resulting in a sharper more reactive drag pattern.

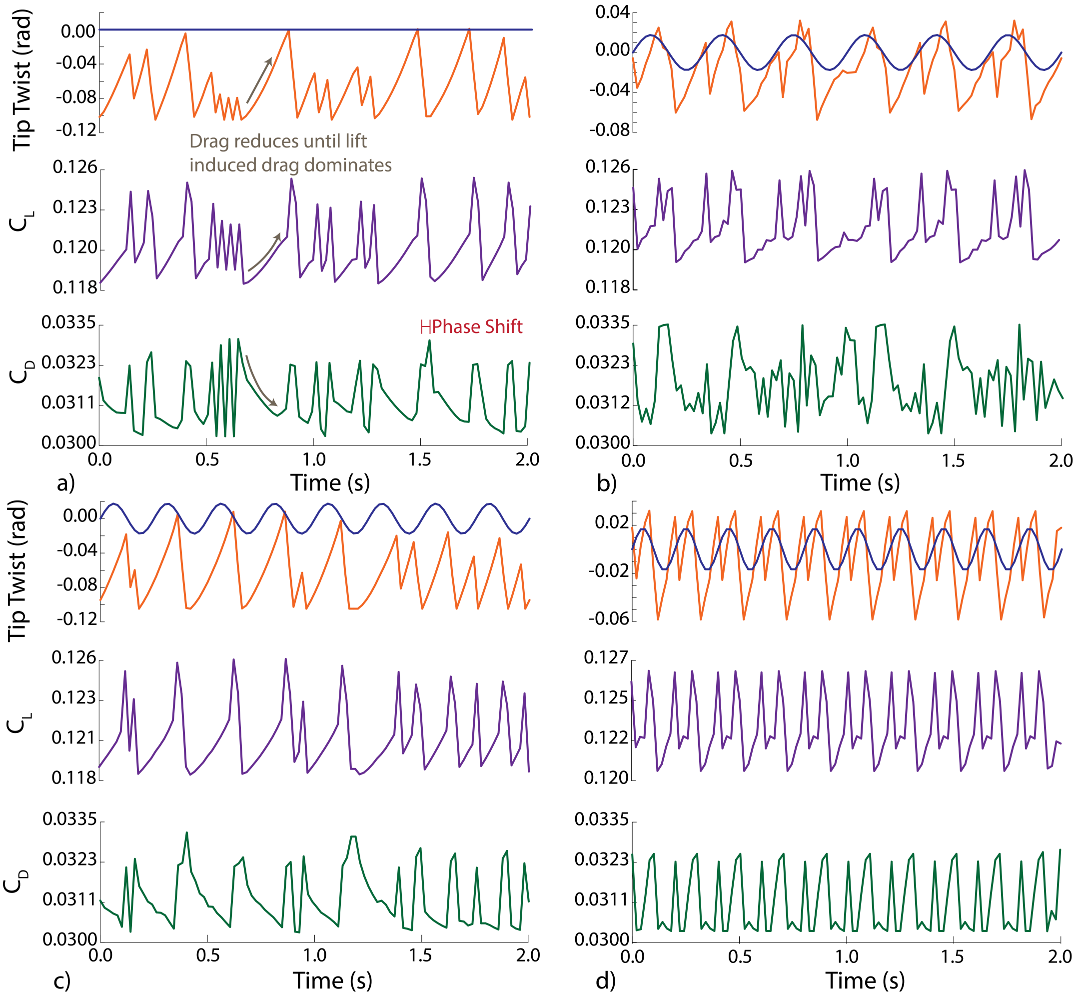

Figure 5.34: Initial twist pattern in blue, optimal twist pattern in orange, lift coefficient from optimal twist pattern in purple, and optimal drag pattern in green for initial twist patterns of: a) 0 Hz, b) 3 Hz, c) 4 Hz, d) 5 Hz.

5.4.6 Results from the Aeroelastic Model

The optimization run by using the aeroelastic model has an enormous run-time, which is in the order of 50-100 hours. This severely limits its capability to adequately test different flight conditions, cost functions, and constraints, let alone the possibility of performing in real-time during the flight. However, the validated aeroelastic model still plays a critical role during the preliminary design stage, where it can be utilized to generate simulated flight data to be used for training the neural networks.

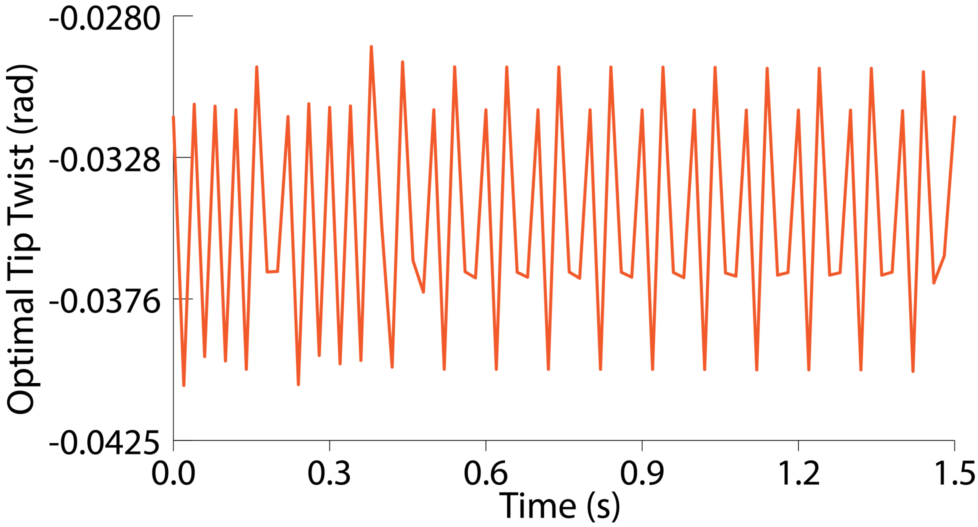

Figure 5.35: Inital input twist and resulting output twist from optimization of the aeroelastic model

In this case, the optimization is performed using twist frequency at 5 Hz as the initial value and the simulation time is reduced from 2 sec to 1.5 sec, to expedite the run time. Figure 5.35 shows the optimal tip twist pattern. We can see that the optimal result is a simple oscillation between -0.03 rad and -0.04 rad, with some M-shaped characteristics reminiscent of the pattern seen in the 5 Hz optimal pattern from

Figure 5.34d). The optimal twist pattern for a zero degree twist input is nearly identical to the 5 Hz initial conditions, meaning that the results are relatively independent of the initial conditions. This suggests that there is little or no null space in the solution set to the aeroelastic model. As a result, the twist pattern in Fig. 5.35 shows the optimal tip twist that occurs regardless of initial conditions.

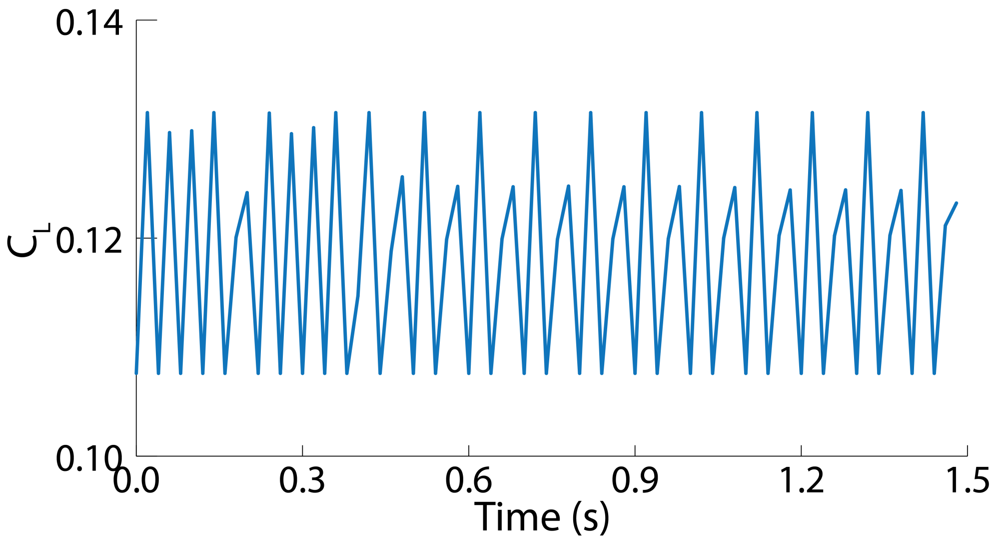

Figure 5.36: Optimized C_L resulting from optimal tip twist in Figure 5.35

Figures 5.36 and 5.37 show the resulting lift and drag coefficients for optimal tip twist pattern shown in Fig. 5.35. This correlates to a drag reduction of approximately 1.5 % when compared to the static drag coefficient for the same lift. In summary, while the optimal twist pattern from the aeroelastic model may be a little more conservative than the one from the neural network, we are confident that both optimal twist patterns would indeed result in drag reduction, even if they are not quite to the postulated magnitude. These two analysis models play a unique role in the development of flight

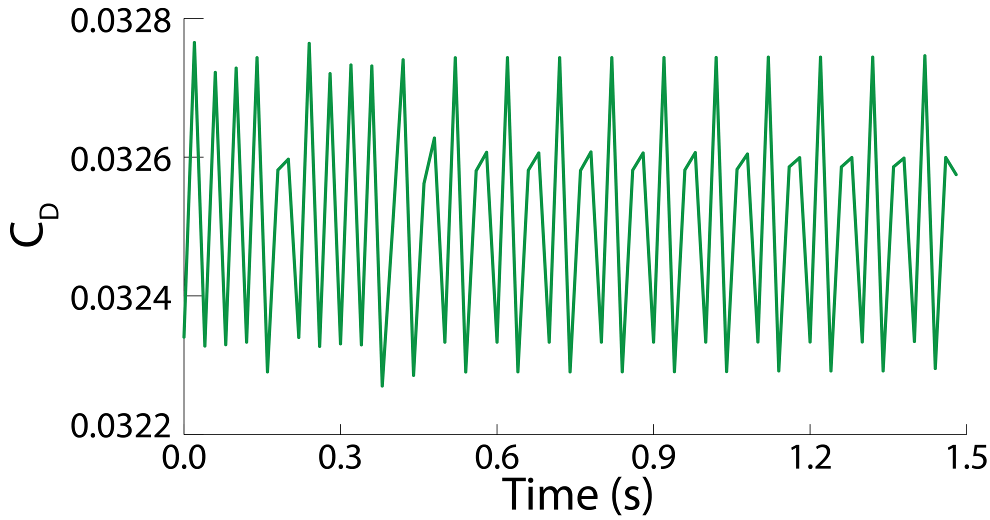

Figure 5.37: Optimized C_D curve resulting from optimal tip twist in Figure 5.35

systems. At initial preliminary design cycle, the aeroelastic model can be used to assess and determine the favorable wing twist patterns over a range of flight scenarios, and the simulated data can be generated and used to train and validate the neural networks to attain the most accurate neural network model. Subsequently, the trained neural network model can then be integrated with onboard flight control systems to enable real-time mission adaptive flight controls.

Chapter 6

Conclusion

The work presented in this dissertation explores the aerodynamic capabilities of an active twist wing, specifically through the modeling and control regime, below a there will be a summary of the work presented and some possible avenues for future work.

6.1 Summary

This dissertation starts by creating an aeroelastic model for the envisioned operating regime. This entailed treating the wing like an elastic beam and using the Galerkin finite element method to model it. The aerodynamics used was an unsteady vortex lattice method with horseshoes instead of vortex rings as are typically used. This decision was made to reduce the number of computations and is reasonable because of the particular operating regime. These methods were combined using the structure of an open source MATLAB code package to create the aeroelastic simulations.

The aeroelastic simulations were then compared to wind tunnel testing of a cellular lattice based wing structure. The wind tunnel testing included static and dynamic testing that the aeroelastic modeling was validated from. The modeling of the wind tunnel tested wing proved to be especially challenging because of its low aspect ration and disproportionately large blocky body but the simulations matched with the static wind tunnel performance well. The dynamic wind tunnel tests and simulations were able to show an ability to identify critical control derivatives relating to the desired coefficient.

This dissertation approached the problem of control of the active twist aircraft in three different ways, dictated by the underlying design of the targeted wing. The first two control methodologies are means of addressing the cellular lattice based wing design. The basic structure of these designs does not lend itself to typical simulations approaches because as the structure continues to scale or the lattice pitch continues to decrease the problem quickly becomes intractable. To address the issue of the curse of dimensionality with the underlying structure, decentralized controllers were proposed.

Using a very basic spring mass damper model that was identified through vibration testing and frequency analysis of a carbon fiber cubic octahedron voxel, a decentralized controller was developed using the LMI framework. The large model that represents a HALE, which would operate in a similar regime to the UAV's that were designed and tested in this dissertation, was broken into operational subsections and the concept of an "active" voxel was presented. The active voxel is a voxel with the ability to sense and actuate itself. The LMI framework allowed for sufficient conditions to put in place output covariance controls which help to augment the stability of the structure. The proposed aircraft and decentralized controllers were simulated with a gust input and the effectiveness of various amounts of “active voxels” compared.

While it is necessary to have a decentralized control for the problem at hand, there are significant amounts of additional information that exist due to the fundamental nature of the structure that is often ignored during the creation of traditional decentralized control models. To address this the use of the transfer matrix method was rebranded as a means to create a decentralized control, specific models. The transfer matrix method traditionally had been used as a solving method that solved a state at a time in a time domain simulation or was used to find modal values both with reduced matrix size. By taking that framework the boundary conditions and the static information between the boundary conditions and a selected state vector could be taken into account within the decentralized model. After the model was created and LQR controller was applied, and the Pareto optimal curves were compared for various actuation locations and combinations.

Finally, for the more traditional active twist aircraft built by Aurora Flight Sciences, the decentralized control framework was not necessary. Using the modeling techniques presented earlier the aerodynamic coefficients were determined, and an aeroelastic state matrix was created. From this, a gain scheduling controller was created as well as an extended Kalman filter. For the extended Kalman filter and an aeroelastic database was designed to contain the necessary partial derivatives with n-dimensional interpolation to estimate the current partial derivatives and reducing the amount of time required for the processing the control loop.

The previous questions pertained to the lower level control and stabilization of either the structure or commanded tip twist; they do not address how to determine what the required tip twist should be. To address this issue, a constrained optimization problem was formulated with the limitations of MADCAT in mind as the constraints. The aeroelastic model developed earlier was then used as part of the constrained optimization and is a large factor to why the reduction in computations was necessary. A neural network was also trained using the wind above tunnel results. The two simulations techniques and their resulting tip twist pattern optimization were compared, showing some fundamental characteristics that were shared by both and aerodynamic efficiency gains of $3 - 5\%$.

6.2 Future Works

This work can be extended into many different applications and workplaces. The most immediate are the is the design and control of a scalable active twist technology. The torque tube approach presented in this dissertation is a good approach for mesoscale aircraft or winglets but will not scale to commercial grade aircraft wings. In the future expanding the control algorithms with localized distributed actuation on a lattice-based wing such as the one in Figure 6.1 would allow for the continued scaling and for the advantages of active twist technology to continue to be used.

Beyond the continued use of the control and modeling architecture developed

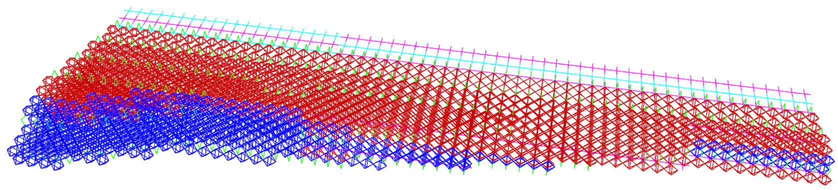

Figure 6.1: Proposed design of a swept wing design for MADCAT v1.0

in this dissertation for active twist technologies they could also be applied to, but not limited to the following topics:

- Structural of space structures
- Control of domestic infrastructures such as bridges, buildings, or dams
- Watercraft and underwater vehicles
- Helicopters
- Wind turbines
- Crawling robots
- Earthquake protection

Bibliography

[1] Iata 2011 annual review. *IATA*, 2011.

[2] Mujahid Abdulrahim, Helen Garcia, Gregory F Ivey, and Rick Lind. Flight testing a micro air vehicle using morphing for aeroservoelastic control. In *AIAA Structures, Structural Dynamics, and Materials Conference*, pages 2004–1674, 2004.

[3] Peter Adey, Lucy Budd, and Phil Hubbard. Flying lessons: exploring the social and cultural geographies of global air travel. *Progress in Human Geography*, 31(6):773–791, 2007.

[4] Lubomir Bakule. Decentralized control: An overview. *Annual reviews in control*, 32(1):87–98, 2008.

[5] Silvestro Barbarino, Onur Bilgen, Rafic M Ajaj, Michael I Friswell, and Daniel J Inman. A review of morphing aircraft. *Journal of Intelligent Material Systems and Structures*, 22(9):823–877, 2011.

[6] John J Bertin and Michael L Smith. Aerodynamics for engineers. 1998.

[7] Samuel Calisch. Physical finite elements. Master's thesis, M.I.T., 2014.

[8] CE de Souza, RGA da Silva, and CES Cesnik. An object-oriented unsteady vortex lattice method for aeroelastic analyses of highly flexible wings. In *10th World Congress on Computational Mechanics*, 2012.

[9] Edward E Degen, Mark S Shephard, and Robert G Loewv. Combined finite element-transfer matrix method based on a mixed formulation. *Computers & Structures*, 20(1):173–180, 1985.

[10] Michael H Dickinson, Fritz-Olaf Lehmann, and Sanjay P Sane. Wing rotation and the aerodynamic basis of insect flight. *Science*, 284(5422):1954–1960, 1999.

[11] Public Domain. Nasa armstrong fact sheet: Solar-power research. *Alternative Energy and Shale Gas Encyclopedia*, page 241, 2016.

[12] David B Doman, Michael W Oppenheimer, and David O Sigthorsson. Wingbeat shape modulation for flapping-wing micro-air-vehicle control during hover. *Journal of guidance, control, and dynamics*, 33(3):724–739, 2010.

[13] Mark Drela. Xfoil: An analysis and design system for low reynolds number airfoils. In *Low Reynolds number aerodynamics*, pages 1–12. Springer, 1989.

[14] James C Ferris. *Wind-tunnel investigation of a variable camber and twist wing.* National Aeronautics and Space Administration, 1977.

[15] Demeter-G Fertis. *Nonlinear mechanics.* CRC Press, 1999.

[16] MI Friswell. The prospects for morphing aircraft. In *Smart Structures and Materials (SMART09), IV ECCOMAS Thematic Conference*, pages 175–188, 2009.

[17] Philip E Gill, Walter Murray, and Michael A Saunders. Snopt: An sqp algorithm for large-scale constrained optimization. *SIAM review*, 47(1):99–131, 2005.

[18] Zdobysław Goraj, Andrzej Frydrychiewicz, and Jacek Winiecki. Design concept of a high-altitude long-endurance unmanned aerial vehicle. *Aircraft design*, 2(1):19–44, 1999.

[19] Justin Hale. Boeing 787 from the ground up. *Aero*, 4:17–24, 2006.

[20] Robert L Halfman. Experimental aerodynamic derivatives of a sinusoidally oscillating airfoil in two-dimensional flow. 1952.

[21] Hossam Hendy, Xiaoting Rui, Qinbo Zhou, and Mostafa Khalil. Controller parameters tuning based on transfer matrix method for multibody systems. *Advances in Mechanical Engineering*, 2014, 2014.

[22] Dewey H Hodges and G Alvin Pierce. *Introduction to structural dynamics and aeroelasticity*. Number 15. Cambridge University Press, 2011.

[23] David G Hull. Fundamentals of airplane flight mechanics, 2007.

[24] Benjamin Jenett, Sam Calisch, Daniel Cellucci, Nick Cramer, Neil Gershenfeld, Sean Swei, and Kenneth C Cheung. Digital morphing wing: Active wing shaping concept using composite lattice-based cellular structures. *Soft Robotics*, 2016.

[25] Benjamin Jenett, Daniel Cellucci, Christine Gregg, and Kenneth Cheung. Meso-scale digital materials: modular, reconfigurable, lattice-based structures. In *ASME*

2016 11th International Manufacturing Science and Engineering Conference, pages V002T01A018–V002T01A018. American Society of Mechanical Engineers, 2016.

[26] James J Joo, Christopher R Marks, Lauren Zientarski, and Adam Culler. Variable camber compliant wing–design. In *23rd AIAA/AHS Adaptive Structures Conference*, pages 2015–1050, 2015.

[27] Vladislav Klein and Eugene A Morelli. *Aircraft system identification: theory and practice*. American Institute of Aeronautics and Astronautics Reston, Va, USA, 2006.

[28] Manoochehr M Koochesfahani. Vortical patterns in the wake of an oscillating airfoil. *AIAA journal*, 27(9):1200–1205, 1989.

[29] Sridhar Kota and Joel A Hetrick. Adaptive compliant wing and rotor system, June 10 2008. US Patent 7,384,016.

[30] Sridhar Kota, Russell Osborn, Gregory Ervin, Dragan Maric, Peter Flick, and Donald Paul. Mission adaptive compliant wing–design, fabrication and flight test. In *RTO Applied Vehicle Technology Panel (AVT) Symposium*, 2009.

[31] Ryan Krauss and Mohamed Okasha. Discrete-time transfer matrix modeling of flexible robots under feedback control. In *American Control Conference (ACC), 2013*, pages 4104–4109. IEEE, 2013.

[32] Ryan W Krauss. Computationally efficient modeling of flexible robots using the

transfer matrix method. *Journal of Vibration and Control*, page 1077546311408466, 2011.

[33] Jayanth Kudva, Peter Jardine, Chris Martin, and Kari Appa. Overview ofthe arpajwl" smart structures and materials development-smart wing" contract.

[34] Jayanth N Kudva, Brian P Sanders, Jennifer L Pinkerton-Florance, and Ephrahim Garcia. Overview of the darpa/afrl/nasa smart wing phase ii program. In *SPIE's 8th Annual International Symposium on Smart Structures and Materials*, pages 383–389. International Society for Optics and Photonics, 2001.

[35] A Selva Kumar and TS Sankar. A new transfer matrix method for response analysis of large dynamic systems. *Computers & structures*, 23(4):545–552, 1986.

[36] PK Kundu, IM Cohen, and DR Dowling. Fluid mechanics, 920 pp, 2012.

[37] Svetlana Kuzmina, Gennadi Amiryants, Johannes Schweiger, Jonathan Cooper, Michael Amprikidis, and Otto Sensberg. Review and outlook on active and passive aeroelastic design concepts for future aircraft. In *ICAS 2002 Congress*, pages 8–13, 2002.

[38] Geethalakshmi S Lakshmikanth, Radhakant Padhi, John M Watkins, and James E Steck. Adaptive flight-control design using neural-network-aided optimal nonlinear dynamic inversion. *Journal of Aerospace Information Systems*, 11(11):785–806, 2014.

[39] Dennis J Linse and Robert F Stengel. Identification of aerodynamic coefficients using computational neural networks. *Journal of Guidance, Control, and Dynamics*, 16(6):1018–1025, 1993.

[40] Johan Löfberg. Yalmip: A toolbox for modeling and optimization in matlab. In *Computer Aided Control Systems Design, 2004 IEEE International Symposium on*, pages 284–289. IEEE, 2004.

[41] Lyle N Long and Tracy E Fritz. Object-oriented unsteady vortex lattice method for flapping flight. *Journal of Aircraft*, 41(6):1275–1290, 2004.

[42] Manoranjan Majji, Othon K Rediniotis, and John L Junkins. Design of a morphing wing: modeling and experiments. In *Proceedings of the AIAA Atmospheric Flight Mechanics Conference and Exhibit, Hilton Head, South Carolina, USA*, pages 20–23, 2007.

[43] Marcial Marazzo, Rafael Scherre, and Elton Fernandes. Air transport demand and economic growth in brazil: A time series analysis. *Transportation Research Part E: Logistics and Transportation Review*, 46(2):261–269, 2010.

[44] Tomas Melin. A vortex lattice matlab implementation for linear aerodynamic wing applications. Master's thesis, Royal Institute of Technology (KTH), Stockholm, Sweden, 2000.

[45] Gerald D Miller. Active flexible wing (afw) technology. Technical report, DTIC Document, 1988.

[46] Samuel C Miller, Markus P Rumpfkeil, and James J Joo. Fluid-structure interaction of a variable camber compliant wing. In *53rd AIAA Aerospace Sciences Meeting*, page 1235, 2015.

[47] Thomas J Mueller. *Fixed and flapping wing aerodynamics for micro air vehicle applications*, volume 195. AIAA, 2001.

[48] Anand Natarajan, Rakesh K Kapania, and Dan J Inman. Aeroelastic optimization of adaptive bumps for yaw control. *Journal of aircraft*, 41(1):175–185, 2004.

[49] Anand Natarajan, Rakesh K Kapania, and Daniel J Inman. Dynamic aeroelastic response of adaptable airfoils using neural networks. *AIAA paper*, (2002-5599):4–6, 2002.

[50] David A Neal, Matthew G Good, Christopher O Johnston, Harry H Robertshaw, William H Mason, and Daniel J Inman. Design and wind-tunnel analysis of a fully adaptive aircraft configuration. *Proceedings of AIAA/ASME/ASCE/AHS/ASC SDM, Palm Springs, California*, 2004.

[51] Nhan Nguyen, Eric Ting, Daniel Nguyen, Tung Dao, and Khanh Trinh. Coupled vortex-lattice flight dynamic model with aeroelastic finite-element model of flexible wing transport aircraft with variable camber continuous trailing edge flap for drag reduction.

[52] Nhan Nguyen, Khanh Trinh, Susan Frost, and Kevin Reynolds. Coupled aeroelastic vortex lattice modeling of flexible aircraft.

[53] Nhan Nguyen, Ilhan Tuzcu, Tansel Yucelen, and Anthony Calise. Longitudinal dynamics and adaptive control application for an aeroelastic generic transport model. In *AIAA Guidance, Navigation, and Control Conference*, 2011.

[54] Nhan Nguyen and James Urnes. Aeroelastic modeling of elastically shaped aircraft concept via wing shaping control for drag reduction. In *AIAA Atmospheric Flight Mechanics Conference*, pages 13–16, 2012.

[55] Xander Olsthoorn. Carbon dioxide emissions from international aviation: 1950–2050. *Journal of Air Transport Management*, 7(2):87–93, 2001.

[56] Michael W Oppenheimer, David B Doman, and David O Sigthorsson. Dynamics and control of a biomimetic vehicle using biased wingbeat forcing functions. *Journal of guidance, control, and dynamics*, 34(1):204–217, 2011.

[57] Jennifer L Pinkerton, Anna-Maria R McGowan, Robert W Moses, Robert C Scott, and Jennifer Heeg. Controlled aeroelastic response and airfoil shaping using adaptive materials and integrated systems. In *1996 Symposium on Smart Structures and Materials*, pages 166–177. International Society for Optics and Photonics, 1996.

[58] Man Mohan Rai. Towards a hybrid aerodynamic design procedure based on neural networks and evolutionary methods. In *20th AIAA Applied Aerodynamics Conference, Saint Louis, MO*, volume 24, page 26, 2002.

[59] Man Mohan Rai and Nateri K Madavan. Aerodynamic design using neural networks. *AIAA journal*, 38(1):173–182, 2000.

[60] Man Mohan Rai, Nateri K Madavan, and Frank W Huber. Improving the unsteady aerodynamic performance of transonic turbines using neural networks. In *Proceedings of the 38th AIAA aerospace sciences meeting and exhibit, Reno, NV*, pages 2000–0169, 2000.

[61] Gregory Reich and Brian Sanders. Introduction to morphing aircraft research. *Journal of Aircraft*, 44(4):1059–1059, 2007.

[62] Bao Rong, Xiaoting Rui, Guoping Wang, and Fufeng Yang. Discrete time transfer matrix method for dynamics of multibody system with real-time control. *Journal of Sound and Vibration*, 329(6):627–643, 2010.

[63] Xiao-Ting Rui, Edwin Kreuzer, Bao Rong, and Bin He. Discrete time transfer matrix method for dynamics of multibody system with flexible beams moving in space. *Acta Mechanica Sinica*, 28(2):490–504, 2012.

[64] Sanjay P Sane and Michael H Dickinson. The control of flight force by a flapping wing: lift and drag production. *Journal of experimental biology*, 204(15):2607–2626, 2001.

[65] Sanjay P Sane and Michael H Dickinson. The aerodynamic effects of wing rotation and a revised quasi-steady model of flapping flight. *Journal of experimental biology*, 205(8):1087–1096, 2002.

[66] Wei Shyy, Hikaru Aono, Satish Kumar Chimakurthi, P Trizila, C-K Kang, Car-

los ES Cesnik, and Hao Liu. Recent progress in flapping wing aerodynamics and aeroelasticity. *Progress in Aerospace Sciences*, 46(7):284–327, 2010.

[67] Dragoslav D Siljak. *Large-scale dynamic systems: stability and structure*, volume 310. North-Holland New York, 1978.

[68] Dragoslav D Siljak. *Decentralized control of complex systems*. Courier Corporation, 2011.

[69] David A Smith and Michael F Timberlake. World city networks and hierarchies, 1977-1997 an empirical analysis of global air travel links. *American Behavioral Scientist*, 44(10):1656–1678, 2001.

[70] AYN Sofla, SA Meguid, KT Tan, and WK Yeo. Shape morphing of aircraft wing: status and challenges. *Materials & Design*, 31(3):1284–1292, 2010.

[71] Bret K Stanford and Philip S Beran. Analytical sensitivity analysis of an unsteady vortex-lattice method for flapping-wing optimization. *Journal of Aircraft*, 47(2):647–662, 2010.

[72] Weihua Su. Modified strain-based geometrically nonlinear beam formulation for modeling slender wings with deformable cross-sections. 2014.

[73] Sean Shan-Min Swei and Nhan Nguyen. Aeroelastic wing shaping control subject to actuation constraints. In *55th AIAA/ASMe/ASCE/AHS/SC Structures, Structural Dynamics, and Materials Conference*, page 1041, 2014.

[74] Sean Shan-Min Swei, Guoming G Zhu, and Nhan Nguyen. Lmi-based multiobjective optimization and control of flexible aircraft using vcctef. In *56th AIAA/ASCE/AHS/ASC Structures, Structural Dynamics, and Materials Conference*, page 1844, 2015.

[75] TM Tan, A Yousuff, LY Bahar, and M Konstantinidis. A modified finite element-transfer matrix for control design of space structures. *Computers & Structures*, 36(1):47–55, 1990.

[76] Andrew S Thomas, William S Saric, Albert L Braslow, DM Bushnell, RC Lock, JE Hackett, et al. Aircraft drag prediction and reduction. Technical report, DTIC Document, 1985.

[77] ASW Thomas. Aircraft drag reduction technology. Technical report, DTIC Document, 1984.

[78] Paul Upham, Callum Thomas, David Gillingwater, and David Raper. Environmental capacity and airport operations: current issues and future prospects. *Journal of Air Transport Management*, 9(3):145–151, 2003.

[79] James Urnes, Nhan Nguyen, Corey Ippolito, Joseph Totah, Khanh Trinh, and Eric Ting. A mission adaptive variable camber flap control system to optimize high lift and cruise lift to drag ratios of future n+ 3 transport aircraft. In *51st AIAA Aerospace Sciences Meeting, Grapevine, TX*, 2013.

[80] Roelof Vos, Zafer Gurdal, and Mostafa Abdalla. Mechanism for warp-controlled twist of a morphing wing. *Journal of Aircraft*, 47(2):450–457, 2010.

[81] Yinan Wang, Andrew Wynn, and Rafael Palacios. Nonlinear model reduction for aeroelastic control of flexible aircraft described by large finite-element models. 2014.

[82] Zhicun Wang. Time-domain simulations of aerodynamic forces on three-dimensional configurations, unstable aeroelastic responses, and control by neural network systems. 2004.

[83] Isaac E Weintraub, David O Sigthorsson, Michael W Oppenheimer, and David B Doman. Implementation of split-cycle control for micro aerial vehicles. In *Robot Intelligence Technology and Applications 2*, pages 859–876. Springer, 2014.

[84] Terry A. Weisshaar. *Aerospace Structures - an Introduction to Fundamental Problems*. 2011.

[85] Peter Colin Young and JC Willems. An approach to the linear multivariable servomechanism problem. *International journal of control*, 15(5):961–979, 1972.

[86] AI Zečević and DD Šiljak. A new approach to control design with overlapping information structure constraints. *Automatica*, 41(2):265–272, 2005.

[87] G Zhu, MA Rotea, and R Skelton. A convergent algorithm for the output covariance constraint control problem. *SIAM Journal on Control and Optimization*, 35(1):341–361, 1997.

[88] Lauren Ann Zientarski. *Wind Tunnel Testing of a Variable Camber Compliant Wing with a Unique Dual Load Cell Test Fixture*. PhD thesis, University of Dayton, 2015.

Appendix A

Constants from Decentralized Control Construction

$$C_{x_n} = \frac{G_{21}H_{11}^nQ_{12}-G_{11}H_{11}^nQ_{22}}{G_{12}Q_{22}-G_{22}Q_{12}+G_{11}H_{12}^nQ_{22}-G_{21}H_{12}^nQ_{12}}$$

$$+m_2A_2$$

$$+\frac{F_{11}^{n+1}R_{11}T_{21}-F_{11}^{n+1}R_{21}T_{11}}{R_{12}T_{21}-R_{22}T_{11}+F_{12}^{n+1}R_{11}T_{21}-F_{12}^{n+1}R_{21}T_{11}}\,.$$

$$C_{E_{n-1}} = \frac{-G_{11}H_c^nQ_{22}+G_{21}H_c^nQ_{12}}{G_{12}Q_{22}-G_{22}Q_{12}+G_{11}H_{12}^nQ_{22}-G_{21}H_{12}^nQ_{12}}\,.$$

$$C_{E_n} = \frac{F_c^{n+1}R_{21}T_{11}-F_c^{n+1}R_{11}T_{21}}{R_{12}T_{21}-R_{22}T_{11}+F_{12}^{n+1}R_{11}T_{21}-F_{12}^{n+1}R_{21}T_{11}}$$

$$-\frac{G_{11}H_c^nQ_{22}-G_{21}H_c^nQ_{12}}{G_{12}Q_{22}-G_{22}Q_{12}+G_{11}H_{12}^nQ_{22}-G_{21}H_{12}^nQ_{12}}\,.$$

$$C_{E_{n+1}} = \frac{F_c^{n+1}R_{11}T_{21}-F_c^{n+1}R_{21}T_{11}}{R_{12}T_{21}-R_{22}T_{11}+F_{12}^{n+1}R_{11}T_{21}-F_{12}^{n+1}R_{21}T_{11}}\,.$$

$$C_R = \frac{R_{23}T_{11}-R_{13}T_{21}-T_{11}T_{23}+T_{13}T_{21}}{R_{12}T_{21}-R_{22}T_{11}+F_{12}^{n+1}R_{11}T_{21}-F_{12}^{n+1}R_{21}T_{11}}\,.$$

$$C_L = \frac{Q_{12}Q_{23}-Q_{13}Q_{22}+G_{13}Q_{22}-G_{23}Q_{12}}{G_{12}Q_{22}-G_{22}Q_{12}+G_{11}H_{12}^nQ_{22}-G_{21}H_{12}^nQ_{12}}\,.$$

When $j < n$,

$$C_{E_j^n} = \frac{-1}{Q_{11} - \frac{Q_{12}Q_{21}}{Q_{22}}} \left[\frac{\begin{array}{c} \left(\frac{Q_{12}G_{21}}{Q_{22}}\right) H_c^j + \\ \left(G_{11}H_{12}^j + G_{12} - \frac{Q_{12}Q_{21} - H_{12}^j + Q_{12}G_{22}}{Q_{22}}\right)\left(\frac{T_{11}R_{21}}{T_{21}} - R_{11}\right) F_c^{j+1} \end{array}}{R_{11}F_{12}^{j+1} + R_{22} - \frac{T_{11}(R_{21}F_{12}^{j+1} + R_{22})}{T_{21}}} \right],$$

and when $j > n$,

$$C_{E_j^n} = \frac{-1}{T_{21} - \frac{T_{22}}{T_{12}}} \left[\frac{\begin{array}{c} \frac{(T_{22}R_{11} - R_{21})F_c^{j+1}}{T_{12}} + \\ \left(G_{21} - \frac{Q_{22}}{Q_{12}}\right) H_c^j \left(R_{21}F_{12}^{j+1} + R_{22} - \frac{T_{22}}{T_{12}}\left(R_{11}F_{12}^{j+1} + R_{12}\right)\right) \end{array}}{\frac{Q_{22}}{Q_{12}}\left(G_{11}H_{12}^j + G_{12}\right) - G_{21}H_{12}^j + G_{22}} \right].$$